

**ORGANIZATION OF INORGANIC COMPLEXES
IN SUPRAMOLECULAR STRUCTURES
BASED ON PEPTIDES AND PEPTIDE NUCLEIC ACIDS**

By

Dilhara R. Jayarathna

A dissertation submitted in partial fulfillment of the requirements for the degree of
Doctor of Philosophy in Chemistry

Carnegie Mellon University
Pittsburgh, Pennsylvania
December 2017

ACKNOWLEDGEMENT

I would like to express my sincere gratitude to my PhD advisor Professor Catalina Achim for her wonderful support during my PhD. I am so grateful that I got the opportunity to do my PhD with you. I cannot thank you enough for being there for me always, not only as a wonderful mentor but also as a friend. My many thanks go to my committee members, Professor Danith Ly and Professor Stefan Bernhard for their feedback during my PhD exams. Your guidance and advices grew me as a scientist. I also thank all my teachers from pre-school to grad-school, for feeding me with knowledge. I wouldn't have come this far if it was not for your guidance.

I also thank all my collaborators for their wonderful work and support, Dr. Stephen House from Professor Judith C. Yang's group for STEM imaging and analysis, Dr. Francesco Tassinari, Dr. Nirit Kantor-Uriel from Professor Ron Naaman's group for chiral peptide project and Lior Bezen from Professor Yossi Paltiel's group for γ -PNA project. Thank You Professor Suba R. Das for letting me use your lab facilities to do gel-electrophoresis experiments and Professor Rongchao Jin for useful discussion on gold nanocluster-PNA project. My gratitude also goes to Dr. Munira Fouz for helping me to learn gel-electrophoresis and Dr. Anindita Das for the help with gold nanocluster synthesis.

My special thanks go to all my group members with whom I worked with during last five years. Thank You Dr. Arnie De Leon and Dr. Jing Kong for helping me to get started at Achim lab and Dr. Dinesh Bhunia for γ -PNA monomers. To Dr. Heather Stout for being a great friend and your work on HypSpec simulations. Arthur, thank you so much for all your help from research discussions to friendly conversations. Dr. Selma Ulku and Yookie, you two are the friends that I never thought I would find at CMU. I

cannot thank you two enough for being there by my side all the time to listen to all the complaints and to raise me up to keep moving forward.

My biggest thanks go to my family. Each and every one of you made me who I am today. If it was not for loving husband Gayan, I would never have achieved this huge accomplishment. Thank you so much for everything you did during last ten years. My dear parents, you two are the true winners of this PhD. I have no words to express my gratitude for making me who I am. I will forever be in debt to both of you for everything you did with immense love from all your hearts.

ABSTRACT

“Organization of Inorganic Complexes in Supramolecular Structures based on Peptides and Peptide Nucleic Acids”

By: Dilhara R. Jayarathna

Advisor: Professor Catalina Achim

The research described in this thesis shows how the properties of PNA can be successfully leveraged to improve the functional and structural versatility of hybrid inorganic nanomaterials. Specifically, the thesis describes the synthesis and investigation of the properties of PNA triplex-metal complex, single stranded-PNA or PNA duplex-gold nanocluster (AuNC), PNA duplex-colloidal quantum dot (CQD) and peptide-metal complex assemblies.

PNA triplexes were characterized as a nano-scaffold to organize four- or six-coordinate metal complexes at predefined positions in the triplex. Binding of 3d metal ions (Fe^{2+} , Ni^{2+} , Cu^{2+} or Zn^{2+}) to PNA triplexes modified with 2,2'-Bipyridine (**Bpy**) or 8-Hydroxyquinoline (**Q**) ligands were studied. UV-melting studies proved that the metal complexes function as alternative base triplets or pairs in that they increase the thermal stability of the triplexes. The metal complexes coordinate two or three ligands although three bidentate ligands are in close proximity of each other within a triplex. The specific stoichiometry can be understood based on the stability constants of the metal complexes determined by simulation of UV-Vis titration data using HypSpec refinement program. Metal coordination to ligand-modified PNA triplexes was further studied by Electron Paramagnetic Resonance (EPR) spectroscopy and Circular Dichroism (CD) spectroscopy. The metal-containing PNA triplexes contain a chiral L-Lysine and adopt a left-handed chiral structure in solution. The handedness of the PNA

triplex determines that of the metal complexes formed with the **Bpy**-containing PNA triplexes.

A method was developed to synthesize, purify and isolate PNA-AuNC conjugates bearing a known number of single stranded PNAs per AuNC. Purification of the PNA-AuNC conjugates was achieved by gel-electrophoresis. UV-Vis spectroscopic analysis quantitatively proves that the discrete gel bands correspond to PNA-AuNC conjugates bearing a distinct number of ss-PNA per cluster. The PNA-AuNC conjugates were characterized by UV-melting, CD Spectroscopy and Fluorescence Spectroscopy. UV-melting analysis of PNA-AuNC conjugates shows that the AuNCs negatively affect the π -stacking of terminal nucleobases of the duplexes and reduce the thermal stability of the PNA duplexes. The chiral properties of AuNCs are highly sensitive to the PNA modifications as revealed by CD spectroscopy. Fluorescence emission intensity and the maximum emission wavelength of AuNCs increases and blue-shifts, respectively, upon PNA modification. Scanning transmission electron microscopy (STEM) proved that complementary PNA strands can “glue” two AuNCs into AuNC dimers.

The effect of the use of chiral γ -PNA duplex as linkers that connect CQDs to random-shaped gold nanoislands on the extinction properties of a monolayer of CQDs was studied. A two-fold larger extinction enhancement in the visible spectrum was achieved when a monolayer of helical chiral γ -PNA duplex molecules connects the CQDs to the gold nanoislands instead of when a monolayer of achiral molecules is used to connect the CQDs to the nanoislands. The increase in extinction was exploited to measure the differential absorption of right- and left-polarized light by the monolayer of chiral molecules.

The effect of handedness on electron transfer through self-assembled monolayers of chiral helical peptides was studied by electrochemistry. A difference between the charge transfer rate constants for oxidation and reduction processes was observed. This observed asymmetry was reversed for left- and right-handed helical peptides. The result can be explained by invoking the spontaneous magnetization that occurs when chiral helical peptides are self-assembled on a gold substrate and the chiral induced spin selectivity of the electron transfer.

CONTENTS

TABLE OF CONTENTS.....	vii
LIST OF FIGURES	x
LIST OF TABLES	xviii
ABBREVIATIONS AND SYMBOLS.....	xx

TABLE OF CONTENTS

CHAPTER I: Introduction	1
I.1 References	11
CHAPTER II: Metal Coordination to Ligand-Modified Peptide Nucleic Acid Triplexes	14
II.1 Introduction	14
II.2 Research Design	17
II.3 Results and Discussion.....	19
II.3.2 Thermal Stability of Triplexes	19
II.3.3 Spectrophotometric Titrations.....	21
II.3.4 Effect of Metal Coordination on Handedness of L ₃ PNA	31
II.4 Conclusions	36
II.5 Material and Methods.....	37
II.5.1 Solid-Phase PNA Synthesis	37
II.5.2 Melting Curves.....	38
II.5.3 Spectrophotometric Titrations.....	40
II.5.4 HypSpec Data Simulations.....	45
II.5.5 EPR Spectroscopy	48
II.5.6 CD Spectroscopy	48
II.6 References	48
CHAPTER III: Peptide Nucleic Assisted Dimerization of Gold Nanoclusters.....	52
III.1 Introduction.....	52
III.2 Research Design.....	56
III.3 Results and Discussion	58
III.3.1 Purification, Isolation and Quantification of PNA-AuNC conjugates bearing a finite number of PNA strands per cluster.....	58
III.3.2 Melting behavior of PNA-AuNC conjugates.....	62
III.3.3 Chiral Properties of PNA-AuNC conjugates	64

III.3.4 STEM analysis of AuNC dimerization	67
III.4 Conclusions	73
III.5 Material and Methods	74
III.5.1 Synthesis of 3-(tritylthio)-2,2-bis(tritylthio)methyl propanoic acid.....	74
III.5.2 Solid Phase PNA Synthesis	76
III.5.3 Synthesis and Polyacrylamide gel electrophoretic purification of the [$\text{Au}_{25}(\text{Capt})_{18}$] clusters	77
III.5.4 Synthesis, PAGE purification and Isolation of PNA-AuNC conjugates ..	79
III.5.5 Quantification of Au_{25} :PNA ratio in Conjugates	82
III.5.6 Melting analysis	84
III.5.7 CD Spectroscopy	84
III.5.8 Fluorescence Spectroscopy	85
III.5.9 STEM Imaging and Analysis.....	88
III.6 References.....	90
CHAPTER IV: Chirality Based Probing of Plasmon-Dot Coupling	94
IV.1 Introduction.....	94
IV.2 Research Design	96
IV.3 Results and Discussion	97
IV.3.1 Thermal Stability and Helicity Characterization of PNA Duplexes.....	97
IV.3.2 Light Extinction Measurements.....	99
IV.4 Conclusions.....	104
IV.5 Material and Methods	104
IV.5.1 Solid-Phase PNA Synthesis.....	105
IV.5.2 Sample Preparations for Extinction Measurements.....	105
IV.5.3 Light Extinction Curve Measurements	108
IV.5.4 UV-Melting and CD Spectroscopy.....	109
IV.6 References.....	110
CHAPTER V: Spin Dependent Mechanism of Charge Transfer through Helical Peptides	112
V.1 Introduction.....	112
V.2 Research Design.....	116
V.3 Results and Discussion.....	118
V.3.1 Characterization of the Helicity of the Peptides	118
V.3.2 Characterization of Peptide Monolayers formed on Gold Surface	120

V.3.3 Charge Transfer Rates Through Opposite-Handed Helical Peptides.....	121
V.3.4 The Proposed Model	123
V.4 Conclusions.....	127
V.5 Material and Methods	128
V.5.1 Peptide Synthesis	128
V.5.2 CD Spectroscopy.....	131
V.5.3 Monolayer Formation	132
V.5.4 Polarization Modulation Infrared Reflection Absorption Spectroscopy (PMIRRAS)	132
V.5.5 Electrochemistry	133
V.5.6 Contact Potential Difference (CPD)	134
V.5.7 Superconducting Quantum Interference Device (SQUID) Measurements	134
V.6 References.....	135

LIST OF FIGURES

CHAPTER I: Introduction	1
Figure I.1: Chemical structure of (a) DNA and (b) PNA.	2
Figure I.2: Cartoon representations of (a) self-assembly of single stranded, ligand-modified nucleic acids to form metal-mediated base pairs at pre-defined positions in nucleic acid duplexes. “Reprinted from the reference ²⁷ with permission from Elsevier.” (b) PNA duplex that contains a metal-mediated [ML ₂] alternative base pair created by the substitution of a pair of nucleobases with a pair of ligands L with high affinity for the metal ion M.....	5
Figure I.3: Cartoon representation of 2D and 3D nanostructures in which AuNCs function as vertices. The complementary PNA hybridization “glues” AuNCs together. Based on the number of PNA strands attached to one AuNC and stoichiometric ratio between the initial mixing components, one can get an architecture of interest.....	7
CHAPTER II: Metal Coordination to Ligand-Modified Peptide Nucleic Acid Triplexes	14
Figure II.1: Cartoon representations of a PNA duplex (left) and a triplex (right) that contain a metal-mediated [ML ₂] or [ML ₃] complexes. The metal complexes of different coordination numbers are created by the substitution of a pair or triplet of nucleobases in a duplex or triplex with a ligands L with high affinity for the metal ion M.....	15
Figure II.2: Chemical structures of AT ₂ (a) or CG-C ⁺ (b) nucleobase triplet. The bases shown in black form Watson-Crick hydrogen bonds; the pyrimidine base in red forms Hoogsteen hydrogen bonds with the purine base.	16
Figure II.3: Cartoon representations for the (a) formation of a nucleic acid triplex, strand orientations in a (b) parallel or (c) anti-parallel triplex. The duplex always has anti-parallel orientation, while the triplex can be either parallel or anti-parallel, based on the orientation of the TFO with respect to the purine strand.	17
Figure II.4: Possible strand orientations in PNA triplexes. Regardless of the relative strand orientation, the ligands are situated in complementary positions in these triplexes.....	18
Figure II.5: A schematic representation of the research design.	18
Figure II.6: Melting curves monitored at 260 nm/ λ_{ML} for 5 μ M Bpy ₃ (a/b) or Q ₃ (c/d) PNA solutions in the absence (solid line) and presence of one equivalent of Fe ²⁺ (dashed line), Ni ²⁺ (dotted line), Cu ²⁺ (dotted-dashed line) or Zn ²⁺ (double dotted-double dashed line). λ_{ML} for each sample is given in Table II.2 foot note.....	20
Figure II.7: Spectrophotometric titrations of Bpy (□) and Bpy ₃ PNA (■) with Fe ²⁺ (a and b), Ni ²⁺ (c and d), Cu ²⁺ (e and f) or Zn ²⁺ (g and h). The lines through the data in (b), (d), (f) and (h) represent simulations of the titration curves for Bpy (dashed line) and Bpy ₃ PNA (solid line) using HypSpec program with the stability constants given in Table II.3. The titration curves with Fe ²⁺ , Ni ²⁺ , Cu ²⁺ and Zn ²⁺ were	

monitored at 525 nm, 296 nm, 301 nm and 295 nm, respectively for Bpy. For Bpy₃ PNA, the titration curves were monitored at 304 nm, 313 nm, 315 nm and at 310 nm with Fe²⁺, Ni²⁺, Cu²⁺ and Zn²⁺ respectively.23

Figure II.8: Spectrophotometric titrations of Q (□) and Q₃ PNA (■) with Ni²⁺ (a and b), Cu²⁺ (c and d), Zn²⁺ (e and f) or Fe²⁺ (g). The titration curves with Ni²⁺, Cu²⁺ and Zn²⁺ were monitored at 375 nm, 376 nm and 362 nm, respectively for Q. For Q₃ PNA, the titration curves were monitored at 460 nm, 408 nm and at 388 nm with Ni²⁺, Cu²⁺, and Zn²⁺, respectively. Insets in (c) and (e) show absorbance change for peaks in visible region. No change in absorbance was observed upon addition of Fe²⁺ to Q₃ PNA. Solid lines (Q₃ PNA) and dashed line (Q ligand) through titration points in b, d and f are simulations obtained using HypSpec and the stability constants are from Table II.3.25

Figure II.9: Speciation diagrams for free Bpy/Q ligand (black lines) and Bpy₃/Q₃ PNA (blue lines) with (a) Fe²⁺, (b/e) Ni²⁺, (c/f) Cu²⁺ and (d/g) Zn²⁺ obtained using the stability constants from Table II.3. Solid line: [M(L)₃]²⁺; dotted line: [M(L)₂]²⁺; segment-dot line: [M(L)]²⁺; dashed line: free L. The vertical solid line goes through the 0.33 [M²⁺]/[L] or 1 eq of M²⁺ per L₃ triplex ratio. The percentage of the dominant [M(L)_x]²⁺ complex at 0.33 [M²⁺]/[L] or 1 eq of M²⁺ per L₃ triplex ratio is written on each figure.31

Figure II.10: (a) EPR spectrum (black line) of a sample of 100 μM Q₃ PNA triplex containing one eq. Cu²⁺ in pH 7.00 10 mM sodium phosphate buffer with 25% glycerol as a glassing agent. The red line represents a simulation with g values 2.048, 2.056, 2.223 and hyperfine A values 64.98 MHz, 94.26 MHz, and 608.3MHz, respectively. (b) Overlap of speciation diagram calculated with logβ₂=13.9 (Table II.3) for Q₃ PNA in the presence of Cu²⁺, with the %[CuQ₂] complex (red circles) measured by quantitation of the EPR spectra31

Figure II.11: CD spectra for 5 μM solutions of (a) Bpy₃ PNA and (b) Q₃ PNA in the absence (solid line) and presence of one equivalent of Fe²⁺ (dashed line), Ni²⁺ (dotted line), Cu²⁺ (dotted-dashed line) or Zn²⁺ (double dotted-double dashed line).33

Figure II.12: CD spectra for 2 μM Bpy₃ PNA solutions with DiSC₂(5) dye in the absence (solid line) and presence of one equivalent of Ni²⁺ (dotted line) and Zn²⁺ (double dotted-double dashed line) (a), for 2 μM Q₃ PNA solutions with DiSC₂(5) dye in the absence (solid line) and presence of one equivalent of Cu²⁺ (dotted-segmented line) and Zn²⁺ (double dotted-double dashed line) (b). Concentration of the dye in the solution was 5 μM. Triplex solutions were prepared in pH 7.00, 10 mM sodium phosphate buffer and 10 % methanol.33

Figure II.13: CD spectra for 5 μM Bpy₃ PNA solutions in the presence of (a) 0, 0.5, 0.7, 0.9 equivalents of Fe²⁺ and (b) 0.2, 0.4, 0.7, 0.9 and 1.0 equivalents of Ni²⁺ ...35

Figure II.14: Concomitant increase in CD (top) and UV absorption (bottom) band intensities in 300-330 nm region with addition of increasing amounts of (a) Fe²⁺ or (b) Ni²⁺ to Bpy₃ PNA.35

Figure II.15: CD (■) and UV (□) titration curves monitored at 308 nm in the presence of (a) Fe^{2+} and at 318 nm in the presence of (b) Ni^{2+} , with 5 μM Bpy ₃ PNA.	36
Figure II.16: Melting curves for Bpy ₃ PNA (a) and Q ₃ PNA monitored at 260 nm in the presence of three equivalents of Ni^{2+} (dotted line), Cu^{2+} (dotted-dashed line) or Zn^{2+} (double dotted-double dashed line)	39
Figure II.17: First derivative plots of melting curves to determine the melting temperatures reported in Table II.2, monitored at 260 nm (a and c) or at λ_{ML} (d and e) for Bpy ₃ PNA (a and b) and Q ₃ PNA in the presence of one equivalent of Fe^{2+} (dashed line), Ni^{2+} (dotted line), Cu^{2+} (dotted-dashed line) or Zn^{2+} (double dotted-double dashed line).	40
Figure II.18: Spectrophotometric titrations of Bpy ligand with Fe^{2+} (a and b), Ni^{2+} (c and d), Cu^{2+} (e and f) or Zn^{2+} (g and h) and of Q ligand with Fe^{2+} (i and j) Ni^{2+} (k and l), Cu^{2+} (m and n) or Zn^{2+} (o and p).	43
Figure II.19: Spectrophotometric titrations of Bpy ligand with Fe^{2+} (a and b) and Bpy ₃ PNA with Ni^{2+} (c and d) at $I=0.33$. Ionic strength of the solution was adjusted with KCl. Concentrations of Bpy, Bpy ₃ PNA and Ni^{2+} were similar to non-ionic strength controlled titrations.	44
Figure II.20: UV-Vis spectra for the titration of Bpy in pH 6.50 10 mM MES buffer with Fe^{2+} . Wavelengths for which the change in absorbance was within 70% of the maximum change in the absorbance within the same band were used first in HypSpec simulations to obtain the stability constants. These wavelengths are identified by blue lines. The red line shows the difference between the initial and final spectra in the titration.	46
CHAPTER III: Peptide Nucleic Assisted Dimerization of Gold Nanoclusters	52
Figure III.1: (a) Size regime to show where AuNC lie compared to the dimensions of molecules and AuNPs. (b) Kohn-Sham orbital energy level diagram to show the electronic transitions in a model $[\text{Au}_{25}(\text{SH})_{18}]^-$ cluster. (b) Simulated optical absorption spectrum for $[\text{Au}_{25}(\text{SH})_{18}]^-$ clusters. “Reprinted (adapted) with permission from the reference ³³ . Copyright (2008) American Chemical Society.”	55
Figure III.2: Schematic representation of the research design	58
Figure III.3: The gel migration pattern for reaction products obtained from the incubation of Au NCs with PNA1-SH3 for 1 hour at 50°C. The PNA1-SH3:AuNC ratios were 0.2, 0.4, 0.5, 0.7, 0.9, 1.3, 1.7, 2.1 and 2.4 (left to right, lanes 1-9) and AuNC only (lane 10).	59
Figure III.4: The gel migration pattern for reaction products obtained from the incubation of Au NCs with PNA1-SH1 for 1 hour at 50°C. Lanes 1-5 and 7-9, PNA1-SH1: Au ₂₅ ratios 0.90, 0.70, 0.50, 0.40, 0.20, 0.05, 0.10, 0.15. Lane 6: AuNC only and Lane 10: PNA 1-SH1 only.	60
Figure III.5: The gel migration pattern for scaled up reactions between PNA1-SH3 or PNA2-SH3 and Au ₂₅ at PNA : Au ₂₅ molar ratio 0.4. Up to six distinct gel bands are seen that correspond to conjugates bearing distinct number of PNAs per Au ₂₅	

cluster. Lane 1: Au ₂₅ only, lane 2: PNA2-SH3: Au ₂₅ reaction mixture and lane 3: PNA1-SH3: Au ₂₅ reaction mixture.	60
Figure III.6: Absorption spectra for 1x (solid line) PNA1-SH3 – Au ₂₅ conjugate, 2x (dashed line) PNA1-SH3 - Au ₂₅ conjugate or 3x (dotted line) PNA1-SH3 – Au ₂₅ conjugates in the wavelength ranges (a) 400 – 850 nm, and (b) 220 – 350 nm. 670 nm and 260 nm are identified by vertical lines. Each extracted conjugate was diluted with water to get reasonable absorbance at 670 nm (Au ₂₅ absorption) and 260 nm (PNA absorption).	62
Figure III.7: Melting curves (a) monitored at 260 nm for ss PNA 1 (10 μM, dotted-dashed line), ss PNA 2 (10 μM, dashed line), PNA 1 – PNA 2 duplex (5 μM, dotted line), PNA 3 duplex (10 μM, double dotted-double dashed line), PNA 1-SH3 – PNA 2-SH3 Au ₂₅ assembly (4 μM in duplex concentration, solid line) or (b) monitored at 670 nm for same PNA 1-SH3 – PNA 2-SH3 Au ₂₅ assembly. All samples were in 10 mM, pH 7.00 sodium phosphate buffer.	63
Figure III.8: CD spectra for PNA1.PNA2 duplex (10 μM, orange), [Au ₂₅ (Capt) ₁₈] [−] clusters (8 μM, black), Captopril ligand (60 μM, pink), PNA1-SH3 - Au ₂₅ conjugate (4 μM PNA1-SH3, blue) , PNA2-SH3 - Au ₂₅ conjugate (4 μM PNA2-SH3, green) or PNA1-SH3-PNA2-SH3 Au ₂₅ assembly (2 μM PNA1-SH3-PNA2-SH3 duplex, red) in 10 mM pH 7.00 sodium phosphate buffer. UV-Vis spectra for these samples are given in Figure III.19.	65
Figure III.9: Example HAADF-STEM micrographs (a,b) and corresponding particle size histograms (c,d) from the annealed PNA1-SH3+PNA2-SH3 (a,c) and annealed PNA3-SH3 (b,d) specimens.	67
Figure III.10: Example HAADF-STEM micrographs (a-e), experimental and simulated-random nn distance distributions (f-j), and center-to-center nn distributions where the simulated-random distribution has been scaled to the non-spike regions of the experimental (k-o) for each of the five samples examined. The simulated-random distributions are in red, while the experimental are overlaid in semi-transparent blue. The dashed lines correspond to the theoretical max-extension distance assuming fully bonded PNA chains for the given sample. In (k-o), the x-axes for each plot have been set to the same range for ease of visual comparison.	69
Figure III.11: Example HAADF-STEM micrograph (a), experimental and simulated-random center-to-center nn distance distribution (b), and nn distributions where the random distribution was scaled to the non-spike regions of the experimental (c) for the annealed PNA3-SH3 specimen at 2 M× magnification. The simulated-random distributions are in red, while the experimental are overlaid in semi-transparent blue.	73
Figure III.12: Gel photograph for purification of [Au ₂₅ (Capt) ₁₈] [−] clusters. Right lane contains Bromophenol blue and Xylene cyanol, which function as a marker to monitor the gel running.	78
Figure III.13: Absorption spectra for (a) band 1 (pure [Au ₂₅ (Capt) ₁₈] [−]), (b) band 2 and (c) band 3. Band 2 and band 3 are impurities, bigger clusters.	78

Figure III.14: STEM (a) image and (b) size distribution of purified $[\text{Au}_{25}(\text{Capt})_{18}]^-$ clusters	79
Figure III.15: Gel photograph that shows specific Au-thiol interactions produce Au_{25} -PNA conjugates with distinct number of PNAs per cluster attached. Lane 1: Au_{25} +PNA1, lane 2: Au_{25} +PNA2, lane 3: Au_{25} +PNA1-SH3, lane 4: Au_{25} +PNA2-SH3, lane 5: Au_{25} NC only, lane 6: PNA only. The top band for lanes 1,2,3 and 4 represents PNA only and/or PNA- Au_{25} aggregates. The top band for lane 6 is PNA only. Other bands are parallel to the structures illustrated by cartoons. The PNA : Au_{25} molar ratio used in the reaction mixtures in the gel shown in is 2.4.	80
Figure III.16: Reaction mixtures after 1 hour incubation at 50 °C those correspond to gel photographs in (a) Figure III.3 and (b) Figure III.4. Aggregation is visible in the reaction mixtures starting from the PNA: AuNC ratio ~ 1.7 and ~ 0.5 for PNA1-SH3 and PNA1-SH1 conjugation, respectively.	81
Figure III.17: Plot of absorbance at 260 nm vs concentration to determine $\epsilon_{260\text{ nm}}$ for $[\text{Au}_{25}(\text{Capt})_{18}]^-$ Concentration of $[\text{Au}_{25}(\text{Capt})_{18}]^-$ was determined based on $\epsilon_{670\text{ nm}} = 8800\text{ M}^{-1}\text{ cm}^{-1}$	83
Figure III.18: UV-Vis spectra for 1xPNA1-SH1- Au_{25} conjugate (a) Au_{25} absorption region and (b) PNA absorption region. The conjugate was dissolved in 3 μl and 14 μl of nano-pure water to measure the Au_{25} and PNA absorption, respectively. The solid vertical lines are drawn through 670 nm and 260 nm.	83
Figure III.19: Absorption spectra for the samples of which CD spectra were measured (a) 200 – 350 nm and (b) 350 -850 nm). (c) and (d) are absorption spectra from 200 – 400 nm and 400 – 850 nm, respectively for concentrated samples of PNA 1-SH3 - Au_{25} conjugate and PNA 2-SH3 - Au_{25} conjugate. These samples were diluted by four-fold to prepare the samples of which CD spectra are given in Figure III.8. Line styles are consistent with Figure III.8 caption.	85
Figure III.20: Fluorescence properties of PNA- Au_{25} conjugates. (a) Fluorescence emission intensity enhancement and (b) blue shift in emission maxima for $[\text{Au}_{25}(\text{Capt})_{18}]^-$ clusters (double dotted – double dashed line), 1 PNA1 – Au_{25} conjugate (solid line), 2 PNA1 – Au_{25} conjugate (dashed line), 3 PNA1 – Au_{25} conjugate (dotted line), crude PNA1- Au_{25} conjugates (dotted-dashed line). Excitation wavelength is 460 nm.	86
Figure III.21: Lognormal quantile (qq) plots of the size distributions for the (a) annealed PNA1-SH3+PNA2-SH3 and (b) annealed PNA3-SH3 specimens. The red line is a visual guide for an ideal lognormal distribution.....	89
CHAPTER IV: Chirality Based Probing of Plasmon-Dot Coupling	94
Figure IV.1: Melting curves measured at 260 nm for 5 μM solutions of duplexes PNA 1S.PNA 2 (black dotted line) and PNA 1R.PNA 2 (black solid line) in 10 mM pH 7.00 NaPi buffer.	98
Figure IV.2: CD spectra of 5 μM solutions of duplexes PNA 1S.PNA 2 (black dotted line) and PNA 1R.PNA 2 (black solid line) and of 2 μM solutions of single stranded	

PNA 1S (blue dotted line), and single stranded PNA 1R (blue solid line). All the samples were prepared in 10 mM pH 7.00 NaPi buffer.99

Figure IV.3: Light extinction spectra for samples that have a monolayer of achiral (MPS, pink) or chiral molecules α -HPA (a, blue lines) and γ -PNA (b, purple lines for left-handed PNA and pink lines for right-handed PNA) on top of Au nanoislands created from a 5 nm-thick layer of evaporated Au. The solid lines correspond to samples without CQDs; the dashed lines correspond to samples that have adsorbed CQDs. The horizontal arrows mark the red shift in the position of the maximum light extinction caused by the adsorption of CQDs. The vertical arrows identify the increase in light extinction due to adsorption of CQDs, at the wavelength of the maximum light extinction for samples that have the CQDs. 100

Figure IV.4: The light extinction of the samples that have monolayers of chiral PNA on Au nanoislands obtained from evaporated Au with 2, 5 or 7nm thickness. The solid lines correspond to the light extinction by the random-shaped Au nanoislands that have a PNA (left/right) monolayer. The dashed lines correspond to samples which a CQD monolayer was added over the PNA (left/right) monolayer. 101

Figure IV.5: The changes in light extinction due to the adsorption of another chiral molecules layer on top of the CQDs monolayer. 102

Figure IV.6: CD spectra of a monolayer of chiral organic molecules on top of the Au nanoislands structure (a) α -HPA or (b) γ -PNA) measured using a circular polarized light source and calculated as the difference between the light extinction of a sample measured using left circular polarized light and the light extinction of the same sample measured using right circular polarized light. 103

Figure IV.7: (a) Schematic sketch of the plasmonic layer of Au nanoislands evaporated on top of a glass substrate; (b) A homogeneous, closely-packed monolayer of organic molecules is covalently-adsorbed onto plasmonic layer of Au nanoislands. The organic molecules may be chiral or achiral. (c) CdSe CQDs with energy band gap of 590nm is covalently adsorbed onto the monolayer or organic molecules. (d) Lastly, an additional monolayer of organic molecules similar to those used in step (b) is formed on top of the monolayer of CQDs. 106

Figure IV.8: Au nanoislands evaporated on top of a glass substrate. The size of the islands depends on the Au thickness of the layer of Au NPs evaporated onto the glass surface, which was (a) 7 nm, (b) 5 nm, or (c) 2 nm. 107

Figure IV.9: The device contains CdSe CQDs (blue) attached to Au nanoislands through chiral (yellow) or achiral molecules. 108

Figure IV.10: Experimental set up for measuring the extinction spectra. 109

Figure IV.11: Absorption spectra at 90 °C (dashed line) and 15 °C (solid line) for 5 μ M CD samples of (a) PNA 1S.PNA 2 and (b) PNA 1R.PNA 2. 109

CHAPTER V: Spin Dependent Mechanism of Charge Transfer through Helical Peptides 112

Figure V.1: A schematic diagram of electron tunneling and hopping mechanisms of electron transfer from ferrocene (donor) to Au surface (acceptor), connected by a

helical peptide bridge. “Reprinted (adapted) with permission from the reference ⁴. Copyright (2011) American Chemical Society.” 113

Figure V.2: (a) A schematic representation of the movement of a charge q with spin state σ along a helical electric field (path of the charge is shown by blue circles). “ a ”, “ b ” and “ Δz ” are the radius of the helix, the pitch of the helix and the position vector of the charges distributed along the helix, respectively. The helical electric field, E_{helix} induces a magnetic field B in the rest frame of the charge and thus influences its spin state.²⁵ The degenerate magnetic dipole associated with a moving electron (charge q of spin state σ) along the helix becomes split due to the generated magnetic field B .²⁶ (b) An energy diagram to explain the CISS effect. A freely moving electron has four states associated with its motion. Those states are given by $|+, +\rangle$, $|-, -\rangle$, $|+, -\rangle$ and $|-, +\rangle$. The first and second variables denote the direction of motion and spin, respectively. Spin up (+) is stabilized relative to the spin down (−) state for an electron that moves towards the positive (+) direction along a left-handed helix. Thus, the $|+, +\rangle$ state is stabilized by spin-orbit coupling to the same extent that the $|+, -\rangle$ state is destabilized. $|+, +\rangle$ state is also degenerate with the state $|-, -\rangle$ which is the stabilized state for the electron moving in the opposite direction of the same helix. The $|+, -\rangle$ state has a $|-, +\rangle$ degenerate state. An electron of $|+, +\rangle$ state moving towards positive (+) direction to elastically backscatter within the left-handed helix, has to change to $|-, -\rangle$ state, changing its both spin state and momentum (direction). This flipping requires a high energy, and thus unlikely. For the right-handed helix, $|+, -\rangle$, $|-, +\rangle$ and $|+, +\rangle$, $|-, -\rangle$ are the ground states and high energy states, respectively. “Reprinted (adapted) with permission from the reference ²⁶. Copyright (2012) American Chemical Society.” 115

Figure V.3: A cartoon representation to illustrate the asymmetry in charge transfer through Fc-modified peptide attached to a gold substrate. Asymmetric charge transfer means, the rate constant for charge transfer from substrate to Fc group is different than the rate constant for charge transfer from Fc to substrate. 116

Figure V.4: Chemical structures of (a) D/L-12 mer or (b) D/L-12 mer Fc peptides. 118

Figure V.5: CD spectra for 0.1 mg/ml solutions of D/L-9 mers (dotted-dashed line), D/L-12 mers (dashed line), D/L-12 mers Fc (solid line) or D/L-15 mers (dotted line) in 1:1(v/v) 10 mM pH 7.00 NaPi:TFE. Black lines are for D-peptides while red lines are for L-peptides. 119

Figure V.6: The amide region of PMIRRAS spectra recorded for the self-assembled monolayers of L-12 mer-Fc and D-12 mer-Fc. The D-12 mer-Fc spectrum is shifted up for clarity. 121

Figure V.7: Plot of peak position relative to the formal potential ($E_p - E_0$) as a function of the normalized scan rate (v/k_0) for either L-12mer-Fc (red squares) or D-12mer-Fc (black dots). The blue solid lines are calculated using the Marcus theory applying a standard electrochemical rate constant (k_0) of 0.48 s^{-1} and assuming the reorganization energy for the ferrocene to be 0.8 eV. The dotted lines are a guide for the eye. 122

Figure V.8: Magnetic moment versus magnetic field measured by SQUID at 300K for the L-12mer-Fc monolayer adsorbed on gold film. The substrate contribution to the signal has been subtracted from the data. The magnetic field was applied either (a) parallel or (b) perpendicular to the sample surface. The inset is a zoom of the low field region where the hysteresis is largest.	126
Figure V.9: A scheme of the proposed mechanism for the asymmetric electron transfer. The gold surface is magnetized and as a result, one spin is injected preferentially from it to the molecule or vice versa. In the case of L-12 mer-Fc peptide (right handed helix) the electron injected from the gold has a spin aligned parallel to the electron's velocity, which is the preferred spin for the electron transfer. As a result, the electron transfer in this direction (reduction process) is faster than backwards. In the case of D-12 mer-Fc peptide (left handed helix), the preferred spin orientation is when the spin is aligned antiparallel to the electron's velocity and therefore the preferred rate is for the oxidation process.	127
Figure V.10: CD spectra for 12 µg/ml solutions of Cya-D/L-(Leu-Ser-Ala) ₃ -H in 10 mM pH 7.00 NaPi buffer. Black line: D-peptide, Red line: L-peptide. The CD spectra were measured in a 1 cm path length cuvette.	131
Figure V.11: Cyclic voltammograms for (a) D-12 mer Fc and (b) L-12 mer Fc..	133
Figure V.12: SQUID measurements for the bare gold surface that has been used as a substrate for the L-12mer-Fc monolayer formation. Applied magnetic field (a) parallel to the field and (b) perpendicular to the field.	135
Figure V.13: SQUID measurements for the L-12mer-Fc monolayer prior to subtraction of the magnetic moment due to the bare gold substrate. Applied magnetic field (a) parallel to the field and (b) perpendicular to the field.....	135

LIST OF TABLES

CHAPTER II: Metal Coordination to Ligand-Modified Peptide Nucleic Acid Triplexes	14
Table II.1: PNA sequences and MALDI data.....	18
Table II.2: Melting temperature T_m ($^{\circ}\text{C}$) ^a for L_3 PNA triplexes in the absence and presence of one/three ^b equivalents of metal ion per triplex.	19
Table II.3: The stability constants for metal complexes formed with the free ligands or L_3 PNA obtained from UV-Vis data using HypSpec refinement program.	26
Table II.4: Conditions for literature stability constants.....	28
Table II.5: Stability constants obtained with two error functions and different wavelength ranges used in the HypSpec simulations.	47
CHAPTER III: Peptide Nucleic Assisted Dimerization of Gold Nanoclusters	52
Table III.1: PNA sequences and MALDI data.....	57
Table III.2: Average PNA1-SH3 : Au ₂₅ ratio in the conjugates from gel electrophoresis bands 1-3.....	62
Table III.3: Melting temperatures (T_m) ^a for single stranded (ss) PNAs or PNA duplexes with no thiol modifications and for Au ₂₅ -PNA assemblies.	64
Table III.4: Summary of AuNC pairing behavior from nn distributions. Spike Span is the distance range spanned by the non-random spike. Highest Bin is the bin with the largest population. The scaling factor yielding the best fit to the non-spike regions of each nn distribution and the resulting calculated of % of AuNCs exhibiting non-random pairing are listed in the last two columns.	71
Table III.5: Fluorescence properties of PNA-Au ₂₅ conjugates.	87
Figure III.21: Lognormal quantile (qq) plots of the size distributions for the (a) annealed PNA1-SH3+PNA2-SH3 and (b) annealed PNA3-SH3 specimens. The red line is a visual guide for an ideal lognormal distribution.....	89
Table III.6: Number of micrographs and total number of nanoparticles comprising each of the experimental datasets used for nearest neighbor analysis.	90
CHAPTER IV: Chirality Based Probing of Plasmon-Dot Coupling	94
Table IV.1: PNA Sequences and MALDI data.....	97
CHAPTER V: Spin Dependent Mechanism of Charge Transfer through Helical Peptides	112
Table V.1: Peptide sequences and mass spectrometry results	118
Table V.2: θ_{222} nm/ θ_{208} nm and percentage helix content of the peptides.....	120
Table V.3: The electron transfer rate constants and surface coverage for the self-assembled monolayers of L/D-12 mer-Fc.....	122
Table V.4: CPD of gold substrate coated with self-assembled monolayers of peptides.	123

Table V.5: Peptide sequences and mass spectrometry results	129
---	-----

ABBREVIATIONS AND SYMBOLS

A	Adenine
A/Ala	Alanine
AEG	N-(2-aminoethyl)-glycine
AuNC	Gold nanocluster
AuNP	Gold nanoparticle
B/Aib	2-Aminoisobutyric acid
Boc	tert-Butyloxycarbonyl
Bpy	Bipyridine
Bpy ₃ PNA	Bipyridine modified triplex
C	Cytosine
CISS	Chiral Induced Spin Selectivity
Cya	Cysteamine
Cys	Cysteine
CD	Circular Dichroism
CPD	Contact Potential Difference
CV	Cyclic Voltammetry
CQD	Colloidal quantum dot
DCM	Dichloromethane
DIEA	Diisopropyl ethyl amine
DiSC ₂ (5)	3,3'-Diethylthiadicarbocyanide
DMF	Dimethylformamide
DMSO	Dimethylsulfoxide
DNA	Deoxyribonucleic acid
ds-	Double stranded
EDTA	Ethylenediaminetetraacetic acid
EPR	Electron Paramagnetic Resonance
Fc	Ferrocene
Fmoc	Fluorenylmethyloxycarbonyl
FTIR	Fourier-transform Infrared Spectroscopy
G	Guanine
Glu	Glutamic acid
HAADF-STEM	High-angle angular dark-field scanning transmission electron microscope
HATU	1-[Bis(dimethylamino)methylene]-1H-1,2,3-triazolo[4,5-b]pyridinium 3-oxid hexafluorophosphate
HBTU	2-(1 <i>H</i> -benzotriazol-1-yl)-1,1,3,3-tetramethyluronium hexafluorophosphate
HPLC	High Pressure Liquid Chromatography
I	Ionic strength
L	Ligand
Lys	Lysine
M	Metal ion
NMR	Nuclear Magnetic Resonance
L ₃ PNA	Ligand modified PNA triplex
Leu	Leucine
MLCT	Metal to Ligand Charge Transfer
MALDI-ToF-MS	Matrix-Assisted Laser Desorption Ionization Time of Flight Mass Spectrometry
MES	2-(N-morpholino)ethanesulfonic acid

NaPi	Sodium Phosphate
OBzl	Benzyl
PM-IRRAS	Polarization Modulation Infrared Reflection Absorption Spectroscopy
PNA	Peptide Nucleic Acid
PyClock	6-Chloro-benzotriazole-1-yloxy-tris-pyrrolidinophosphonium hexafluorophosphate
Q	Hydroxyquinoline
Q ₃ PNA	Hydroxyquinoline modified PNA triplex
Ser	Serine
SQUID	Superconducting Quantum Interference Device
ss-	Single stranded
T	Thymine
tBu	<i>tert</i> -butyl
TBTA	Tris(benzyltriazolylmethyl)amine
TCEP	Tris(2-carboxyethyl)phosphine
TFA	Trifluoroacetic acid
TFO	Triplex forming oligonucleotide
TFE	2,2,2-trifluoroethanol
TFMSA	Trifluoromethanesulfonic acid
THF	Tetrahydrofuran
TIS	Triisopropylsilane
T _m	Melting temperature
UV	Ultraviolet
Vis	Visible
Z	Carboxybenzyl

CHAPTER I: Introduction

Nanotechnology is an evolving field in science that has applications in biology, chemistry, physics, medicine and engineering.¹⁻⁵ Integration of functionally different nanomaterials into hybrid materials that have properties different from those of the individual components is one of the pursuits in current research in nanotechnology.⁶ The success of these hybrid nanomaterials in real life applications, for example, to build a molecular electronic device, depends on a combination of factors that include ease of synthesis, precise position control of nano components in the hybrid material, stability and the interplay between a variety of optical, electronic, magnetic, chiral and fluorescence properties of each component nanomaterial.

The work presented in this thesis is focused on hybrid inorganic-supramolecular nano-materials. More specifically, my research focused on the synthesis, characterization and investigation of properties of Peptide Nucleic Acid (PNA)-metal complex, gold nanocluster (AuNC) or colloidal quantum dot (CQDs) conjugates and ferrocene (Fc)-modified chiral peptides. The organization of inorganic molecules, including metal complexes, AuNCs and CQDs, in organic nano-scaffolds built from single-stranded (ss) PNAs, PNA duplexes, triplexes or peptides is relevant and potentially useful for the applications of the hybrid inorganic-nucleic acid materials in nanotechnology and molecular electronics. My research findings expand the structural and functional diversity of hybrid nanomaterials.

Extensive current research focuses on the use of DNA as building block of nanomaterials due to its remarkable ability to self-assemble by Watson-Crick base pairing and/or other type of relatively weak interactions into a variety of nano-scale 1D, 2D and 3D shapes.⁷ However, DNA-based nanomaterials have properties that may limit its real-life applications, such as an electronic structure that favors electron pairing and

slow charge transport over relatively short distances, limited stability under typical environmental conditions, and susceptibility to nuclease degradation in biological environment.

PNA is an interesting molecule that could be used to overcome or reduce the aforementioned limitations. PNA is a synthetic analogue of DNA that typically has a neutral, achiral, and acyclic pseudopeptide backbone based on N-(2-aminoethyl)glycine (AEG). This is in contrast to DNA that has a negatively charged, chiral, and cyclic sugar diphosphate backbone (Figure I.1). PNA has C- and N- ends while DNA has 3' and 5' ends.⁸⁻¹²

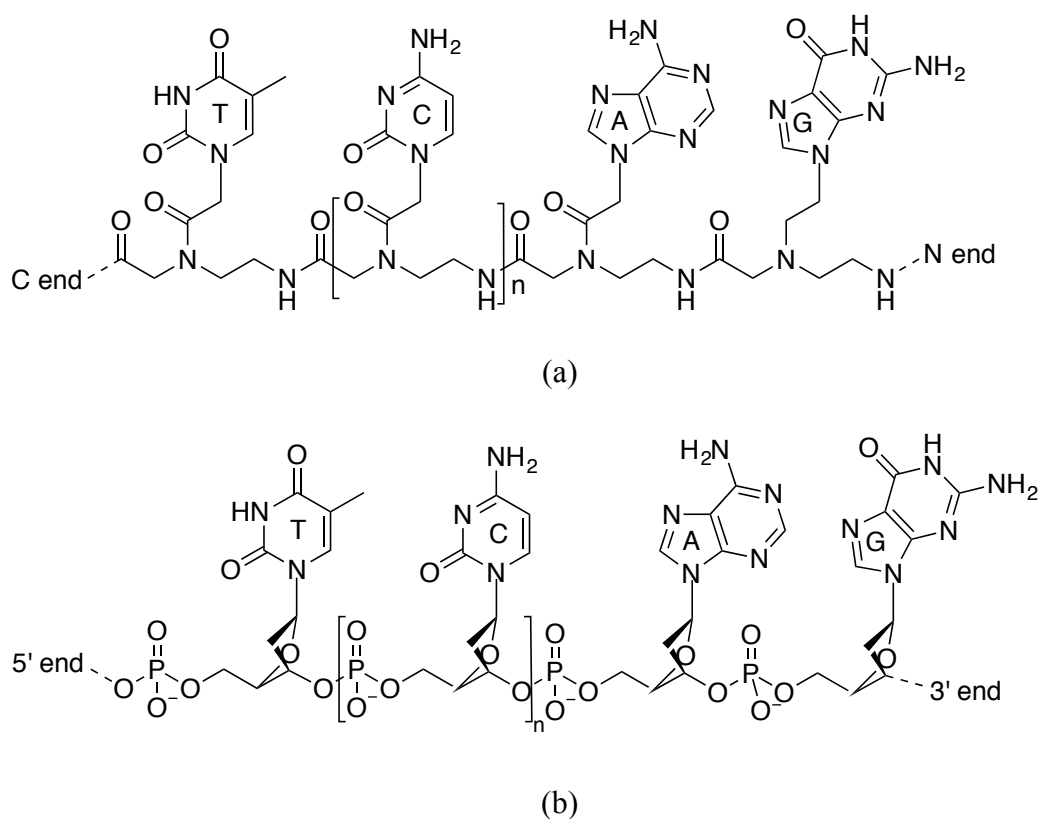


Figure I.1: Chemical structure of (a) DNA and (b) PNA.

PNA has the same nucleobases as DNA; they are attached to the pseudopeptide backbone by methylene carbonyl linkages. PNA can form duplexes with DNA, RNA

and PNA by Watson Crick base pairing. The PNA homo-duplexes or PNA-containing hetero-duplexes can be parallel or anti-parallel; the anti-parallel conformation is more stable.¹³⁻¹⁶ In the case of hetero-duplexes, if the 3' end of the DNA or RNA oligonucleotide faces the N-terminal of the PNA, the duplexes are termed anti-parallel.¹⁵

The PNA-containing homo- and hetero-duplexes are more stable than DNA and RNA homo- and hetero-duplexes due to the lack of electrostatic repulsion of the single strand PNA with the other strands that form the duplex since the backbone of the PNA is neutral. The flexible nature of backbone of the PNA also contributes to the thermodynamic stability of the duplexes. If one considers the entropic factor, one can argue that a flexible backbone is not in favor for the formation of a stable nucleic acid duplex. However, flexible backbone of AEG PNA that has a less conformation rigidity has a favorable enthalpy factor to unfold and fit into the duplex structure. These properties underline the fact that PNA:PNA homo-duplexes or/and PNA:DNA/RNA hetero-duplexes have a higher specificity compared to natural nucleic acid duplexes.^{9, 11-13} The exact solubility of PNA depends on its sequence. But since PNA is neutral, the upper limit for the solubility of PNA in aqueous environment is lower than milimolar concentrations; this is in contrast to DNA whose solubility in aqueous environment can reach as high as 10 milimolar concentrations.

PNA homo-duplexes that have an achiral AEG backbone exist as a racemic mixture of left- and right-handed helices. A preferred handedness can be induced in PNA homo-duplexes by a chiral group situated at the end of a PNA strand, e.g. an amino acid such as L-lysine at the C-terminal of PNA oligomers, or in a PNA monomer, e.g. a γ -modification in the PNA monomer backbone.¹⁴⁻¹⁵ X-ray diffraction or NMR

spectroscopy studies showed that PNA duplexes of AEG-PNA and γ -PNA form P-type helices.¹⁶⁻¹⁷

Metals can be incorporated in nucleic acid-based nanostructures in several ways. A major part of my thesis (Chapter II and III) is dedicated to the study of the incorporation of metals into PNA by two strategies. One strategy is to synthesize PNA monomers in which the nucleobase is replaced with an aromatic ligand (Figure I.2) that has higher affinity towards the metal ions than the nucleobases. The ligand-modified monomer is incorporated into the PNA oligomers during solid phase synthesis and coordinates metal ions to the single strand or to the duplex or triplex upon hybridization. The PNA duplexes have been modified with ligands such as 2,2'-Bipyridine (**Bpy**), 8-Hydroxyquinoline (**Q**), Terpyridine, 1,2-Hydroxypyridone at both terminal and central positions and were shown to coordinate metal ions such as Ni^{2+} , Zn^{2+} , Cu^{2+} or Eu^{3+} to form metal complexes that function as metal-mediated base pairs.¹⁸⁻²¹

The stability of the PNA duplexes that contain metal-mediated base pairs depends on the stability of the metal complex, the way in which the ligand is attached to the PNA, the steric and electronic interactions between the PNA and the metal complex. While the PNA duplex functions as the scaffold for the metal complexes, the metal complexes affect the stability of the structure and impart to it special properties such as electronic²²⁻²³ and luminescence.¹⁸

My research presented in Chapter II was focused on the incorporation of metal complexes with three ligands that replace a base triplet in PNA triplexes. The formation of a triple helical nucleic acid structure was first described in 1957 by Felsenfeld and co-workers.²⁴ It was determined by them that synthetic polynucleotides, polyuridylic acid [poly(U)] and polyadenylic acid [poly(A)] form a stable triple helical structure with a 2:1 ratio of poly(U) to poly(A). They also concluded that, DNA should be able

to form triple helical structures since the two-stranded (A+U) structure is similar to Watson-Crick structure for DNA, where T is present instead of U. For DNA, the melting of the triplex occurs in two steps, one corresponding to the breaking of Hoogsteen hydrogen bonds and a higher temperature step corresponding to the Watson Crick hydrogen bonds.²⁵ In contrast, the melting of the three strands of PNA triplexes is a one step, cooperative process.²⁶

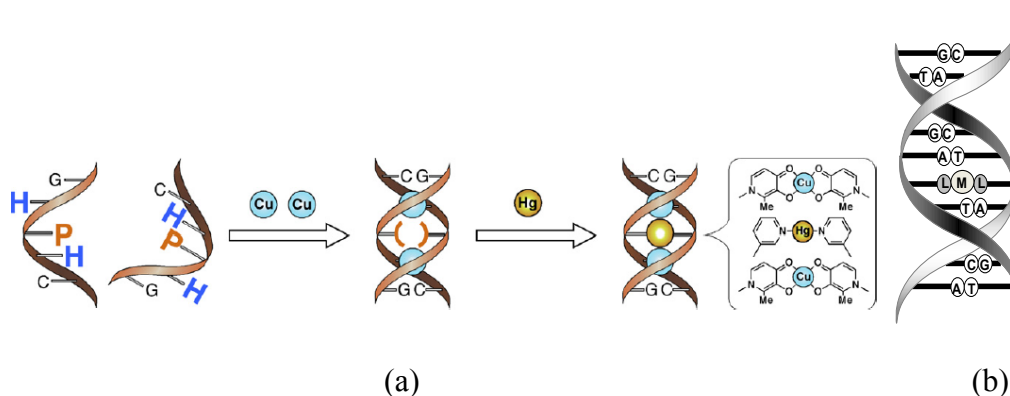


Figure I.2: Cartoon representations of (a) self-assembly of single stranded, ligand-modified nucleic acids to form metal-mediated base pairs at pre-defined positions in nucleic acid duplexes. “Reprinted from the reference²⁷ with permission from Elsevier.” (b) PNA duplex that contains a metal-mediated [ML₂] alternative base pair created by the substitution of a pair of nucleobases with a pair of ligands L with high affinity for the metal ion M.

Actually, PNA was first designed by Buchardt, Nielsen and their collaborators to target a DNA duplex and form a triplex. They assumed that the single stranded PNA (ssPNA) would bind along the major groove of the duplex DNA to form a PNA.DNA₂ triple helix structure.²⁸⁻²⁹ Surprisingly, they observed that polypyrimidine (polyT) ssPNA displaces the homo-pyrimidine strand of the DNA duplex homo-purine (polyA)-homo-pyrimidine target to form a PNA₂.DNA type triplex on the polypurine strand of the DNA duplex. This mode of binding was attributed to the higher affinity that PNA has towards DNA than DNA to itself. In 1997, Buchardt, Nielsen and co-workers reported that it is possible for three ss-PNAs to self-assemble to form a triple helical

structure.²⁶ Since then, several studies have been done on DNA.PNA hetero triplexes, but not much has been reported on homo PNA triplexes.²⁹⁻³⁰

In the case of duplexes, the substitution of two complementary bases with aromatic ligands makes possible the formation of (pseudo) square planar complexes that are structurally similar to nucleobase pairs. However, the substitution of two complementary bases in duplexes with ligands limits the coordination numbers and geometries that a metal complex can have inside a duplex. When a base triplet is substituted with ligands in a triplex, a larger number of possibilities to form metal complexes exists since the coordination number of the metal complex is determined by both the number of binding sites per each ligand and the number of ligands

In Chapter II, I show that metal ions can successfully be incorporated in to ligand-modified PNA triplexes and that the metal complexes introduce interesting properties to the PNA triplexes. PNA triplexes were synthesized in which the central base triplet was replaced with three **Bpy** ligands or **Q** ligands. The possibility for those ligand modifications to coordinate with metal ions, Fe^{2+} , Ni^{2+} , Cu^{2+} and Zn^{2+} was studied. UV-melting studies were performed to determine whether the metal-complexes formed with the ligand modified PNA triplexes function as metal-mediated base pairs or triplets to improve the overall stability of the triplexes. $[\text{Fe}(\text{Bpy})_3]^{2+}$, $[\text{Ni}(\text{Bpy})_3]^{2+}$, $[\text{NiQ}_2]$, $[\text{CuQ}_2]$ and $[\text{ZnQ}_2]$ complexes function as metal-based alternative base pairs or triplets. Spectrophotometric titrations and the analysis of the titration curves by HypSpec refinement program were used to determine the stoichiometry and the relative stability of the metal complexes. $[\text{Fe}(\text{Bpy})_3]^{2+}$, $[\text{Ni}(\text{Bpy})_3]^{2+}$, $[\text{Zn}(\text{Bpy})_2]^{2+}$ and $\text{Cu}(\text{Bpy})^{2+}$ complexes form with PNA triplexes that contain three **Bpy** ligands situated in complementary positions. $[\text{NiQ}_2]$, $[\text{CuQ}_2]$, and $[\text{ZnQ}_2]$ complexes form with **Q**₃ PNA triplexes although three **Q** ligands are situated in complementary positions.

Circular Dichroism (CD) spectroscopy determined the effect of metal coordination to the ligand modifications on the chirality of the triplexes. The handedness of the PNA triplexes was not affected by the metal ions but in some cases, the chirality of the metal complexes such as $[\text{Fe}(\text{Bpy})_3]^{2+}$ and $[\text{Ni}(\text{Bpy})_3]^{2+}$ was determined by the chirality of the PNA triplex.

In Chapter III, I describe a second strategy to introduce metals to PNA by synthesizing PNA oligomers with terminal thiols and covalently attaching the thiol modified ss-PNAs to AuNCs by Au-S bonds. In this chapter, for the first time, I show that AuNCs can be modified with a known number of ss-PNAs attached per AuNC and that these well-defined AuNC-PNA conjugates can be isolated. The long-term goal of the project is to use AuNCs-modified with different number of PNA strands as building blocks to create two- and three-dimensional hybrid-nanostructures in which AuNCs function as the vertices glued by PNA edges (Figure I.3).

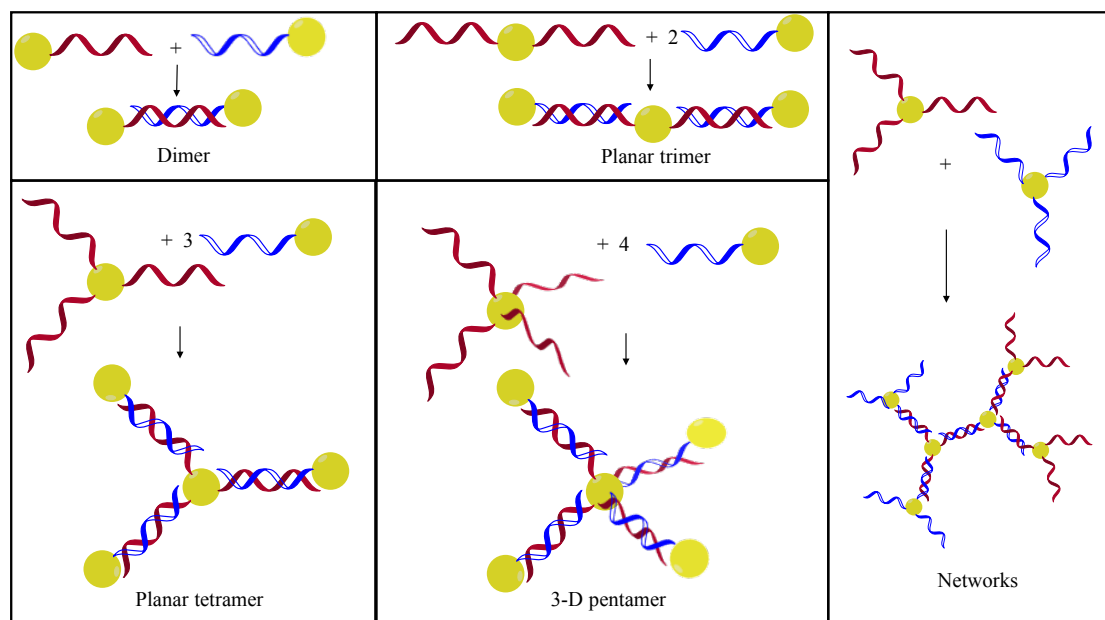


Figure I.3: Cartoon representation of 2D and 3D nanostructures in which AuNCs function as vertices. The complementary PNA hybridization “glues” AuNCs together. Based on the number of PNA strands attached to one AuNC and stoichiometric ratio between the initial mixing components, one can get an architecture of interest.

As the first step to achieve this long-term goal, we show that AuNC dimers can be formed using complementary PNA hybridization. 10 or 8-mer PNA oligomers with three glutamic acid modifications at the C-end and 3-mercapto-2,2-bis(mercaptomethyl)propanoic acid or L-Cysteine at the N-end were synthesized. Water soluble $[\text{Au}_{25}(\text{Capt})_{18}]^-$ clusters were synthesized by a previously reported method and used in this study.³¹ PNA-AuNC conjugates were purified and separated by gel-electrophoresis based on the number of strands attached per AuNC. UV-Vis spectroscopy was used to quantitatively prove that the distinct gel bands that appear during the purification of crude-PNA-AuNC conjugates by gel electrophoresis are due to AuNCs bearing distinct number of PNA oligomers. The properties of AuNC-PNA conjugates were assessed by UV-melting, CD and fluorescence spectroscopies. The UV-melting experiments indicate that the attachment of $[\text{Au}_{25}(\text{Capt})_{18}]^-$ clusters at the ends of PNA duplexes decreases the stability of the duplexes from 68 °C to 58 °C. The chiral properties of $[\text{Au}_{25}(\text{Capt})_{18}]^-$ clusters show a great sensitivity to the PNA attachment. The fluorescence emission intensity of $[\text{Au}_{25}(\text{Capt})_{18}]^-$ clusters increases and blue-shifts with PNA modification. PNA assisted dimerization of $[\text{Au}_{25}(\text{Capt})_{18}]^-$ clusters was confirmed by Scanning Transmission Electron Microscopy (STEM).

In chapter IV, we show that a larger extinction enhancement in the visible spectrum can be obtained by using random Au nanoislands and a CQD monolayer when chiral rather than achiral molecular linkers connect the Au nanoislands and the CQDs. Left- or right-handed γ -PNA duplexes were used in this study. (R) or (S)- γ -Serine modifications were introduced in the PNA oligomers to induce the left or right handedness. We achieved a light extinction of up to 35% which is a 28-fold enhancement from a monolayer of CQDs coupled to Au nanoislands through chiral

molecules compared to a monolayer of CQDs in the absence of Au nanoislands. The same system enabled us to measure the circular dichroism that originates from a chiral monolayer. The results from this chapter may allow one to identify ways to design more sensitive and efficient photon detectors based on CQDs and may also offer a simple way to measure the circular dichroism of chiral monolayers.

In Chapter V, the results of the study of charge transfer through Fc-modified opposite-handed helical peptides are presented. Helical peptides have been researched for a while as potential charge transport material in nano-devices.³² The peptides used in chapter V were modified with a Cysteamine (Cya) linker at the C-end to attach to the gold surface to form self-assembled monolayers. The charge transfer through left- and right-handed helical peptides was studied by electrochemistry and for the first time, a handedness-dependent asymmetry in rate constants for oxidation and reduction was observed. A novel model based on chiral induced spin selectivity (CISS)³³ and the magnetization of the gold substrate is proposed to explain the observed asymmetry. The peptides were synthesized by solid phase peptide synthesis strategy and optimum peptide sequence for the study was identified based on helicity characterization by CD spectroscopy. Similar dipole moments obtained by contact potential difference measurements proved that the handedness-dependent asymmetry of charge transfer through the peptides cannot be explained by an existing dipole-moment based argument.³⁴ Magnetic property measurement of the self-assembled monolayers on the gold surface by superconducting quantum interference device proved that a “spontaneous magnetization” occurs when chiral peptides modified with Fc are self-assembled on a gold surface. This magnetization results the handedness-dependent asymmetry in charge transfer.

In summary, my thesis describes several ways to advance the structural and functional diversity of hybrid nanomaterials. PNA triplexes constituted from three mono-**Bpy** modified ss-PNAs were shown to act as nano-scaffolds to organize tris-metal complexes; previous work on duplexes required two or three adjacent **Bpy** modifications in each ss-PNA strand to form a $[\text{Ni}(\text{Bpy})_3]^{2+}$ complex in a PNA duplex.²⁰ Chiral induction is exerted by PNA triplexes on $[\text{Ni}(\text{Bpy})_3]^{2+}$ and $[\text{Fe}(\text{Bpy})_3]^{2+}$ complexes incorporated in the PNA. The methods for the synthesis and separation of PNA-AuNC conjugates bearing a known number of ss-PNAs open the path to interesting new building blocks for nanostructures. While metal complex incorporation at terminal positions usually increases PNA duplex thermal stability, the attachment of AuNCs at terminal positions decreased the stability of the duplex by 10 °C (from 68 °C to 58 °C) and caused a hyperchromicity reduction from 16% to 6%. This may be due to steric interactions caused by the AuNC, which have ~1 nm core diameter, that negatively impact the π -stacking of terminal base pairs. Previous inorganic complexes with luminescence properties included Eu^{3+} and 1,2-Hydroxypyridone¹⁸ and $[\text{Ru}(\text{Bpy})_3]^{2+23}$. I showed that the emission properties of AuNCs attached to PNA (both emission intensity and emission wavelength) are affected by the nucleic acid. While the ultra-small diameter of the Au_{25} NC (~1 nm) makes it very challenging for one to use electron microscopy to visualize the NCs, in collaborative studies we prove by STEM images that AuNC dimers can be made using complementary PNA strands attached to the AuNCs as a “smart” glue. The CQD-modified monolayers of PNA duplexes attached to gold nanoislands displayed enhanced extinction when compared to CQDs deposited directly onto gold nanoislands or linked to the nanoislands through achiral molecules. This enhancement may be useful in creating a means to characterize the dichroism of self-assembled monolayers of chiral molecules. Asymmetric charge

transfer through chiral peptides of opposite handedness was observed using Fc-modified peptides and may be caused by the chiral induced spin selectivity effect recently discovered by our collaborators at the Weizmann Institute. The advances in the synthesis of hybrid inorganic nano-scaffolds that include ss-PNAs, duplexes, triplexes and chiral peptides and a variety of inorganic components such as metal complexes, AuNCs, and CQDs expand the structural and functional diversity of hybrid nanomaterials.

I.1 References

1. Rosi, N. L.; Mirkin, C. A., Nanostructures in biodiagnostics. *Chem. Rev.*, **2005**, *105* (4), 1547-1562.
2. Peng, Z.; Liu, H., Bottom-up nanofabrication using DNA nanostructures. *Chem. Mater.*, **2016**, *28* (4), 1012-1021.
3. Chen, G.; Roy, I.; Yang, C.; Prasad, P. N., Nanochemistry and nanomedicine for nanoparticle-based diagnostics and therapy. *Chem. Rev.*, **2016**, *116* (5), 2826-2885.
4. Boles, M. A.; Engel, M.; Talapin, D. V., Self-assembly of colloidal nanocrystals: From intricate structures to functional materials. *Chem. Rev.*, **2016**, *116* (18), 11220-11289.
5. Pinheiro, A. V.; Han, D.; Shih, W. M.; Yan, H., Challenges and opportunities for structural DNA nanotechnology. *Nat. Nanotechnol.*, **2011**, *6* (12), 763-772.
6. Samanta, A.; Medintz, I. L., Nanoparticles and DNA—a powerful and growing functional combination in bionanotechnology. *Nanoscale*, **2016**, *8* (17), 9037-9095.
7. Seeman, N. C., DNA in a material world. *Nature*, **2003**, *421* (6921), 427-431.
8. Nielsen, P. E.; Berg, R. H., Sequence-selective recognition of DNA by strand displacement with a thymine-substituted polyamide. *Science*, **1991**, *254* (5037), 1497-1500.
9. Egholm, M.; Buchardt, O.; Christensen, L.; Behrens, C.; Freier, S. M.; Driver, D. A.; Berg, R. H.; Kim, S. K.; Norden, B.; Nielsen, P. E., PNA hybridizes to complementary oligonucleotides obeying the Watson-Crick hydrogen-bonding rules. *Nature*, **1993**, *365* (6446), 566-568.
10. Wittung, P.; Nielsen, P. E.; Buchardt, O.; Egholm, M.; Norde, B., DNA-like double helix formed by peptide nucleic acid. *Nature*, **1994**, 561-563.
11. Egholm, M.; Buchardt, O.; Nielsen, P. E.; Berg, R. H., Peptide nucleic acids (PNA). Oligonucleotide analogs with an achiral peptide backbone. *J. Am. Chem. Soc.*, **1992**, *114* (5), 1895-1897.
12. Egholm, M.; Nielsen, P. E.; Buchardt, O.; Berg, R. H., Recognition of guanine and adenine in DNA by cytosine and thymine containing peptide nucleic acids (PNA). *J. Am. Chem. Soc.*, **1992**, *114* (24), 9677-9678.
13. Wittung, P.; E. Nielsen, P.; Buchardt, O.; Egholm, M.; Norden, B., DNA-like double helix formed by peptide nucleic acid. *Nature*, **1994**, *368* (6471), 561.

14. Dragulescu-Andrasi, A.; Rapireddy, S.; Frezza, B. M.; Gayathri, C.; Gil, R. R.; Ly, D. H., A simple γ -backbone modification preorganizes peptide nucleic acid into a helical structure. *J. Am. Chem. Soc.*, **2006**, *128* (31), 10258-10267.
15. Wittung, P.; Eriksson, M.; Lyng, R.; Nielsen, P. E.; Norden, B., Induced chirality in PNA-PNA duplexes. *J. Am. Chem. Soc.*, **1995**, *117* (41), 10167-10173.
16. He, W.; Crawford, M. J.; Rapireddy, S.; Madrid, M.; Gil, R. R.; Ly, D. H.; Achim, C., The structure of a γ -modified peptide nucleic acid duplex. *Mol. BioSyst.*, **2010**, *6* (9), 1619-1629.
17. He, W.; Hatcher, E.; Balaeff, A.; Beratan, D. N.; Gil, R. R.; Madrid, M.; Achim, C., Solution Structure of a Peptide Nucleic Acid Duplex from NMR Data: Features and Limitations. *J. Am. Chem. Soc.*, **2008**, *130* (40), 13264-13273.
18. de Leon, A. R.; Olatunde, A. O.; Morrow, J. R.; Achim, C., Binding of EuIII to 1, 2-Hydroxypyridinone-Modified Peptide Nucleic Acids. *Inorg. Chem.*, **2012**, *51* (23), 12597-12599.
19. Popescu, D.-L.; Parolin, T. J.; Achim, C., Metal incorporation in modified PNA duplexes. *J. Am. Chem. Soc.*, **2003**, *125* (21), 6354-6355.
20. Franzini, R. M.; Watson, R. M.; Patra, G. K.; Breece, R. M.; Tierney, D. L.; Hendrich, M. P.; Achim, C., Metal binding to bipyridine-modified PNA. *Inorg. Chem.*, **2006**, *45* (24), 9798-9811.
21. Ma, Z.; Olechnowicz, F.; Skorik, Y. A.; Achim, C., Metal binding to ligand-containing peptide nucleic acids. *Inorg. Chem.*, **2011**, *50* (13), 6083-6092.
22. Wierzbinski, E.; de Leon, A.; Davis, K. L.; Bezer, S.; Wolak, M. A.; Kofke, M. J.; Schlaf, R.; Achim, C.; Waldeck, D. H., Charge Transfer through Modified Peptide Nucleic Acids. *Langmuir*, **2012**, *28* (4), 1971-1981.
23. Yin, X.; Kong, J.; De Leon, A.; Li, Y.; Ma, Z.; Wierzbinski, E.; Achim, C.; Waldeck, D. H., Luminescence quenching by photoinduced charge transfer between metal complexes in peptide nucleic acids. *J. Phys. Chem. B*, **2014**, *118* (30), 9037-9045.
24. Felsenfeld, G.; Davies, D. R.; Rich, A., Formation of a three-stranded polynucleotide molecule. *J. Am. Chem. Soc.*, **1957**, *79* (8), 2023-2024.
25. Plum, G. E.; Park, Y.-W.; Singleton, S. F.; Dervan, P. B.; Breslauer, K. J., Thermodynamic characterization of the stability and the melting behavior of a DNA triplex: a spectroscopic and calorimetric study. *Proc. Natl. Acad. Sci. U.S.A.*, **1990**, *87* (23), 9436-9440.
26. Wittung, P.; Nielsen, P.; Norden, B., Observation of a PNA– PNA– PNA Triplex. *J. Am. Chem. Soc.*, **1997**, *119* (13), 3189-3190.
27. Tanaka, K.; Shionoya, M., Programmable metal assembly on bio-inspired templates. *Coord. Chem. Rev.*, **2007**, *251* (21), 2732-2742.
28. Nielsen, P.; Egholm, M.; Berg, R.; Buchardt, O., Sequence-selective recognition of DNA by strand displacement with a thymine-substituted polyamide. *Science*, **1991**, *254* (5037), 1497-1500.
29. Nielson, P. E.; Egholm, M.; Buchardt, O., Evidence for (PNA)₂ DNA Triplex Structure upon binding of PNA to dsDNA by strand displacement. *J. Mol. Recognit.*, **1994**, *7* (3), 165-170.
30. Kim, S. K.; Nielsen, P. E.; Egholm, M.; Buchardt, O.; Berg, R. H.; Norden, B., Right-handed triplex formed between peptide nucleic acid PNA-T8 and poly(dA) shown by linear and circular dichroism spectroscopy. *J. Am. Chem. Soc.*, **1993**, *115* (15), 6477-6481.
31. Kumar, S. Synthesis, Characterization and Application of Water-soluble Gold and Silver Nanoclusters. Carnegie Mellon University, 2013.

32. Shah, A.; Adhikari, B.; Martić, S.; Munir, A.; Shahzad, S.; Ahmad, K.; Kraatz, H.-B., Electron transfer in peptides. *Chem. Soc. Rev.*, **2015**, *44* (4), 1015-1027.
33. Naaman, R.; Waldeck, D. H., Chiral-induced spin selectivity effect. *J. Phys. Chem. Lett.*, **2012**, *3* (16), 2178-2187.
34. Sek, S.; Tolak, A.; Misicka, A.; Palys, B.; Bilewicz, R., Asymmetry of electron transmission through monolayers of helical polyalanine adsorbed on gold surfaces. *J. Phys. Chem. B*, **2005**, *109* (39), 18433-18438.

CHAPTER II: Metal Coordination to Ligand-Modified Peptide Nucleic Acid Triplexes

II.1 Introduction

The selective self-assembly of ligand-modified nucleic acids allows the programmable arrangement of functional elements in nanoscale systems.¹⁻² In the last fifteen years, several research groups have developed numerous nucleic acid duplexes that contain a variety of transition metal-based, alternative base pairs.³⁻⁴ Given the planar geometry of natural nucleobase pairs as well as the contribution of π -stacking interactions to the stabilization of nucleic acid duplexes, square planar metal complexes with aromatic ligands have been the first- and are the preponderant- type of inorganic alternative base pairs that have been incorporated in nucleic acid duplexes. The π -stacking interactions can manifest between the metal complexes and the adjacent bases. The synthesis of PNA monomers that contain ligands instead of nucleobases makes possible the creation of metal-mediated, alternative base pairs at specific locations in PNA duplexes.⁵⁻¹⁰

However, the substitution of two complementary bases with ligands limits the coordination number and geometry that a metal complex can adopt inside a duplex. From this point of view, nucleobase substitution with ligands in triplex nucleic acid-based structures can lead to complexes with larger coordination number and more diverse coordination geometries, which needs to be balanced with the degree of steric compatibility between the metal complex and nucleic acid structure (Figure II.1).

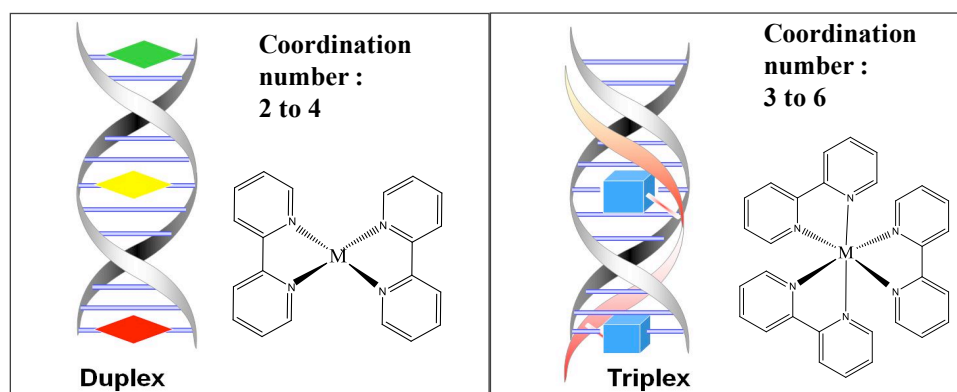


Figure II.1: Cartoon representations of a PNA duplex (left) and a triplex (right) that contain a metal-mediated [ML₂] or [ML₃] complexes. The metal complexes of different coordination numbers are created by the substitution of a pair or triplet of nucleobases in a duplex or triplex with a ligands L with high affinity for the metal ion M.

To date, there have been two reports of metal binding to a DNA triplex modified with ligands. In 2002, Shionoya and collaborators reported the study of a DNA triplex based on 21-base adenine and 21-base thymine strands, each containing a central pyridine ligand.¹¹ The triplex was formed from these strands both in the absence and presence of Ag⁺, as demonstrated by Job plots in which the absorbance at 260 nm was monitored. Both melting temperatures of the triplex, the lower one corresponding to breaking the Hoogsteen hydrogen bonds and the higher one to Watson Crick bonds, were higher in the presence of 4-fold excess Ag⁺ than in the absence of Ag⁺. Based on this evidence, the authors concluded that Ag⁺ coordinates the three pyridine ligands in the triplex. This report was followed in 2009 by a paper from the same group on the di-, tri- and tetra-oligomers, based on monomers with the same backbone as DNA but with 3-hydroxy-4-pyridone (H) instead of a nucleobase.¹² Mass spectrometry and UV-Vis spectroscopy studies showed that in the presence of Fe³⁺, the oligomers formed triplexes with the chemical formula [Fe_n(5'-H_n-3')₃] (n = 2-4) in which each Fe³⁺ coordinates three H ligands. The triplexes adopted a chiral structure due to the presence

of chiral centers in the backbone. Ag^+ binding to CGC^+ nucleobase triplets in DNA triplexes has been reported in several studies.¹³⁻¹⁷

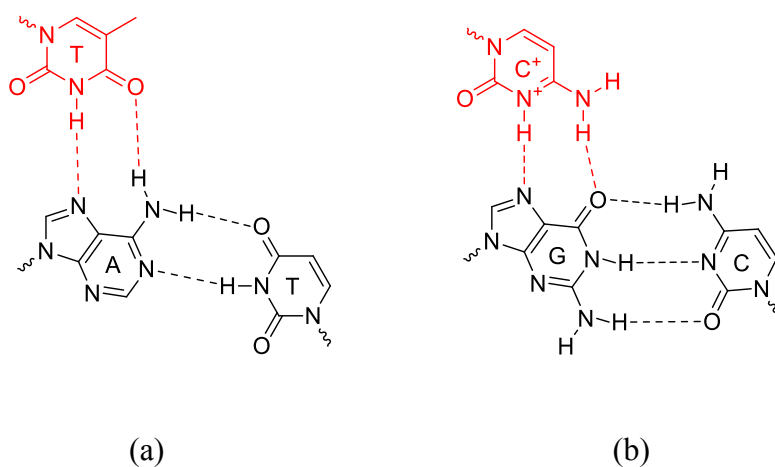


Figure II.2: Chemical structures of AT_2 (a) or CG-C^+ (b) nucleobase triplet. The bases shown in black form Watson-Crick hydrogen bonds; the pyrimidine base in red forms Hoogsteen hydrogen bonds with the purine base.

Same as DNA^{18} , polypurine and polypyrimidine PNA strands can form triplexes.¹⁹ The metallo-regulation of the formation of a ligand-modified PNA/DNA bimolecular triplex has been studied in 2013.²⁰ The incorporation of metal complexes in PNA duplexes and triplexes can broaden its potential applications to nanotechnology and molecular electronics.

In this chapter, we report the study of 3d metal ion binding to PNA triplexes that contain triplets of 8-hydroxyquinoline (**Q**) or 2,2'-bipyridine (**Bpy**) ligands. PNA oligomers synthesized with **Q** or **Bpy** ligand modifications were used in this study. Thermal stability of ligand modified PNA triplexes, in the absence and presence of metal ions was characterized by UV-melting. Stoichiometry of the metal complexes formed with PNA triplexes was determined by UV-Vis titrations and simulation of the titration data by Hypspec program. Circular Dichroism(CD) spectroscopy was used to study the effect of metal ion incorporation on chirality of the triplexes.

II.2 Research Design

A triplex formally consists of a pyrimidine triplex forming oligonucleotide (TFO) bound to the purine strand of a duplex through Hoogsteen or reverse-Hoogsteen hydrogen bonds to a purine strand to form base triplets TA-T or CG-C⁺ (Figure II.2).¹⁸ An (AT₂)_n triplex forms at neutral pH, while a (CG-C⁺)_n triplex forms at acidic pH. The nucleic acid triplexes can have parallel or anti-parallel orientations (Figure II.3); DNA triplexes with a parallel structure are typically more stable than triplexes with an antiparallel structure.

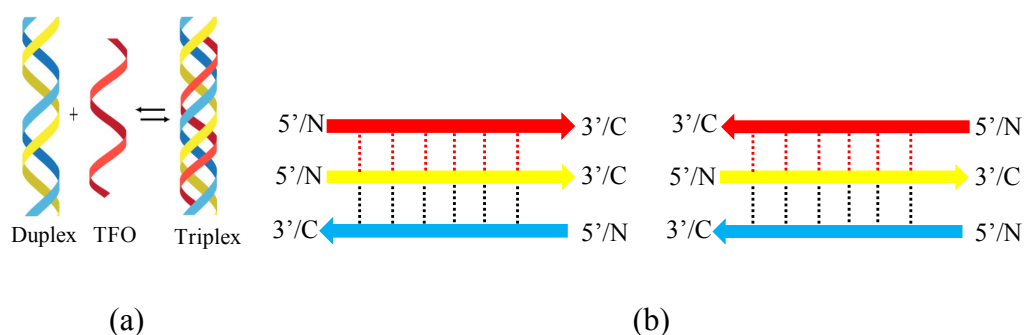


Figure II.3: Cartoon representations for the (a) formation of a nucleic acid triplex, strand orientations in a (b) parallel or (c) anti-parallel triplex. The duplex always has anti-parallel orientation, while the triplex can be either parallel or anti-parallel, based on the orientation of the TFO with respect to the purine strand.

To avoid consideration of the relative strand orientation in PNA triplexes, we incorporated a ligand in the middle of the polypurine and polypyrimidine strands (Figure II.4). We synthesized 11-mer adenine and thymine strands in which the central unit was either a **Bpy** or **Q** ligand (Table II.1), which are termed **Bpy₃ PNA** or **Q₃ PNA**, respectively.

Lys-T ₅ - Bpy -T ₅	Lys-T ₅ - Bpy -T ₅	Lys-T ₅ - Q -T ₅	Lys-T ₅ - Q -T ₅	} Duplex
A ₅ - Bpy -A ₅ -Lys	A ₅ - Bpy -A ₅ -Lys	A ₅ - Q -A ₅ -Lys	A ₅ - Q -A ₅ -Lys	
T ₅ - Bpy -T ₅ -Lys	Lys-T ₅ - Bpy -T ₅	T ₅ - Q -T ₅ -Lys	Lys-T ₅ - Q -T ₅	
Parallel triplex	Anti-parallel triplex	Parallel triplex	Anti-parallel triplex	

Figure II.4: Possible strand orientations in PNA triplexes. Regardless of the relative strand orientation, the ligands are situated in complementary positions in these triplexes.

Table II.1: PNA sequences and MALDI data

Abbreviation	PNA sequence (N to C)	MWcalc/exp
Lys-A ₅ - Bpy -A ₅	H-AAAAA Bpy AAAAA- ^L Lys-NH ₂	3193.23/3193.48
Lys-T ₅ - Bpy -T ₅	H-TTTTT Bpy TTTTT- ^L Lys-NH ₂	3103.90/3103.95
Lys-A ₅ - Q -A ₅	H-AAAAA Q AAAAA- ^L Lys-NH ₂	3182.20/3183.22
Lys-T ₅ - Q -T ₅	H-TTTTT Q TTTTT- ^L Lys-NH ₂	3093.11/3094.27

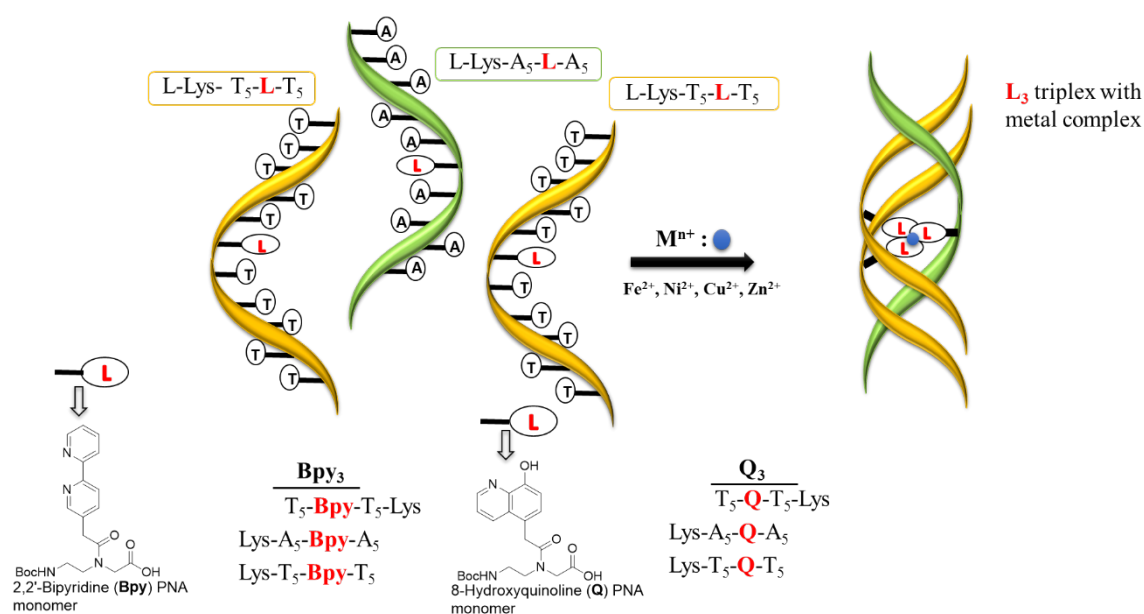


Figure II.5: A schematic representation of the research design.

We decided to study the interactions of **L₃ PNA** (Figure II.5) with Fe²⁺, Ni²⁺, Cu²⁺ and Zn²⁺ based on the high stability constants reported for metal complexes with free **Bpy** or **Q** ligands (Table II.4).²¹⁻²⁵

II.3 Results and Discussion

II.3.1 Thermal Stability of Triplexes

UV-melting curves were measured for the **Bpy**₃ PNA and **Q**₃ PNA triplexes in the absence and presence of Fe²⁺, Ni²⁺, Cu²⁺ or Zn²⁺ (Figure II.6). The changes in absorbance of the triplex were monitored at 260 nm, the wavelength corresponding to the absorbance of the triplex, at 300-320 nm, and at 388-460 nm, the wavelengths corresponding to the coordinated ligands. Table II.2 shows the melting temperatures of the **L**₃ PNA triplexes in the absence and presence of the metal ions.

Table II.2: Melting temperature T_m (°C)^a for **L**₃ PNA triplexes in the absence and presence of one/three^b equivalents of metal ion per triplex.

	Bpy ₃ PNA		Q ₃ PNA	
	260 nm	λ_{ML} ^c	260 nm	λ_{ML} ^c
No M ²⁺	51	NC ^d	53	NC ^d
+ Fe ²⁺	64	65	54	NC ^d
+ Ni ²⁺	66/66	71	65	65
+ Cu ²⁺	52	55	74/74	71
+ Zn ²⁺	52/53	55	58/60	61

^a T_m are known within 1 °C; ^b Melting curves measured in the presence of three equivalents of metal ion per triplex are given in Figure II.16; ^c λ_{ML} for the complexes of **Bpy** with Fe²⁺, Ni²⁺, Cu²⁺ and Zn²⁺ were 304 nm, 315 nm, 316 nm and 315 nm respectively, and for the complexes of **Q** with Ni²⁺, Cu²⁺ and Zn²⁺ were 460 nm, 408 nm and 388 nm, respectively; ^d NC stands for no change observed in absorbance at this wavelength.

The unmodified triplex that contains 11 AT₂ nucleobase triplets has a melting temperature $T_m = 73$ °C. The substitution of a central triplet with three **L** ligands to form the **L**₃ PNA triplexes causes a large destabilization of the triplex ($T_m = 51$ -53 °C). The melting temperature of the **Bpy**₃ PNA triplex increases significantly in the presence of Fe²⁺ ($\Delta T_m = 13$ °C) or Ni²⁺ ($\Delta T_m = 15$ °C) but is not affected by Cu²⁺ or Zn²⁺ (Table II.2). The thermally-induced hyperchromicity at 260 nm is lower in the presence of Fe²⁺ or Ni²⁺, which suggests that steric interactions after the metal coordination to the **Bpy** ligands negatively impact the π -stacking of the nucleobase triplets.

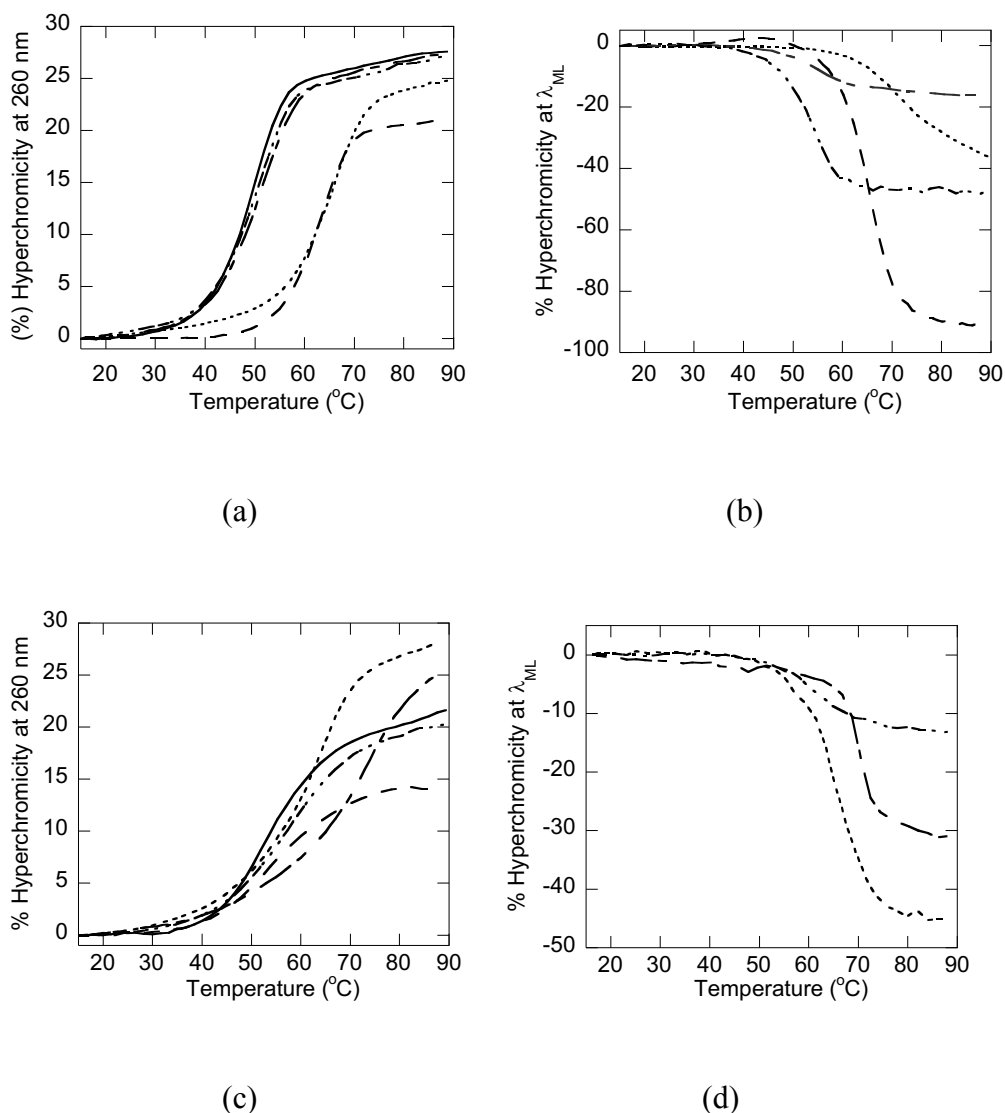


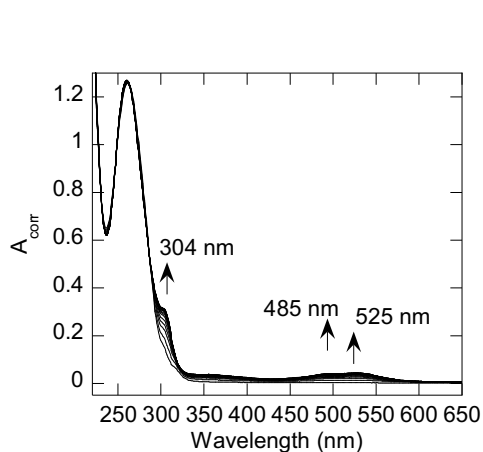
Figure II.6: Melting curves monitored at 260 nm/ λ_{ML} for 5 μ M Bpy₃(a/b) or Q₃(c/d) PNA solutions in the absence (solid line) and presence of one equivalent of Fe²⁺ (dashed line), Ni²⁺ (dotted line), Cu²⁺ (dotted-dashed line) or Zn²⁺ (double dotted-double dashed line). λ_{ML} for each sample is given in Table II.2 foot note.

The melting temperature of the **Q₃ PNA** triplex increases significantly in the presence of Cu²⁺ ($\Delta T_m = 21$ °C) and Ni²⁺ ($\Delta T_m = 12$ °C) suggesting that Cu²⁺ and Ni²⁺ form complexes with the **Q** ligands that act as alternative base triplets (Figure II.6c). Only small changes in T_m are observed in the presence of Fe²⁺ and Zn²⁺. The hyperchromicity for the **Q₃ PNA** triplex increases in the presence of Cu²⁺ and Ni²⁺, which suggests that the coordination of these metals to the ligands “improves” the

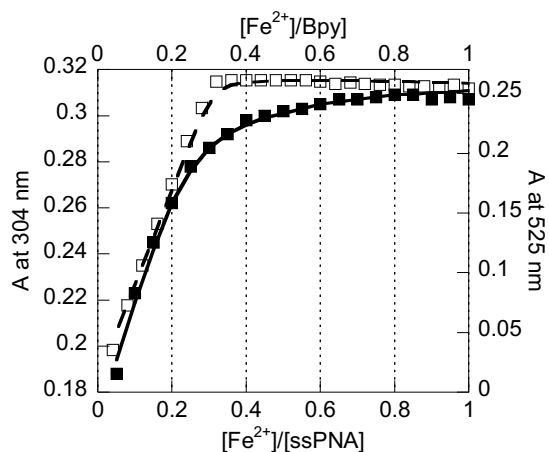
nucleobase stacking in the triplex. Figure II.6b shows the temperature dependence of the absorbance at the wavelength corresponding to the π - π^* transitions of the coordinated **Bpy** ligand (300-320 nm).²⁶ A similar decrease in absorbance was seen for metal-to-ligand charge transfer bands that appear from ~360-500 nm for metal-**Q** complexes formed in **Q₃ PNA** (Figure II.6d). Overall, the relative increase in melting temperatures monitored at 260 nm indicates that Ni^{2+} and Fe^{2+} coordinate to **Bpy** in **Bpy₃ PNA** while Ni^{2+} and Cu^{2+} coordinate to **Q** in **Q₃ PNA** to form metal complexes that act as metal-mediated alternative bases. Cu^{2+} or Zn^{2+} and Fe^{2+} or Zn^{2+} bind weakly or not at all to **Bpy₃ PNA** and **Q₃ PNA**, respectively.

II.3.2 Spectrophotometric Titrations

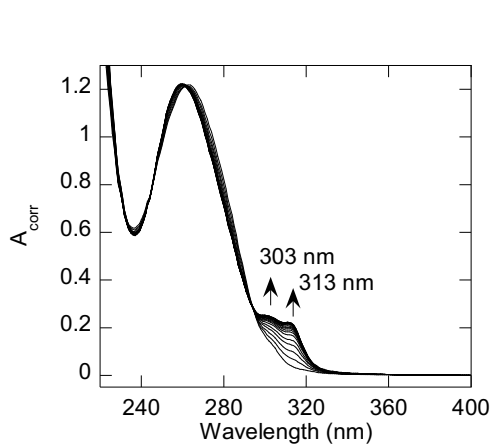
Spectrophotometric titrations with Fe^{2+} , Ni^{2+} , Cu^{2+} , or Zn^{2+} were carried out for the free **Bpy** ligand, the **Bpy₃ PNA**, **Q** ligand and the **Q₃ PNA** triplexes. The UV-Vis spectra of the **Bpy** ligand and the **Bpy₃ PNA** triplex in the presence of increasing amounts of Fe^{2+} , Ni^{2+} , Cu^{2+} , and Zn^{2+} and the corresponding titration curves are shown in Figure II.7. The absorbance band at 260 nm is caused by π - π^* transitions of the nucleobases; its intensity changes upon addition of the metal ions. Metal coordination to **Bpy** ligand shifts the π - π^* transition peaks of the ligand at 235 nm and 285 nm to 245 nm and 295 – 330 nm (Figure II.18 a-g).²⁶⁻²⁷ Thus, the new absorption bands at 300 – 330 nm when **Bpy₃ PNA** is titrated with metal ions arise from π - π^* transitions of the coordinated **Bpy**. In the case of Fe^{2+} , new MLCT bands at 485 nm and 525 nm are observed also.



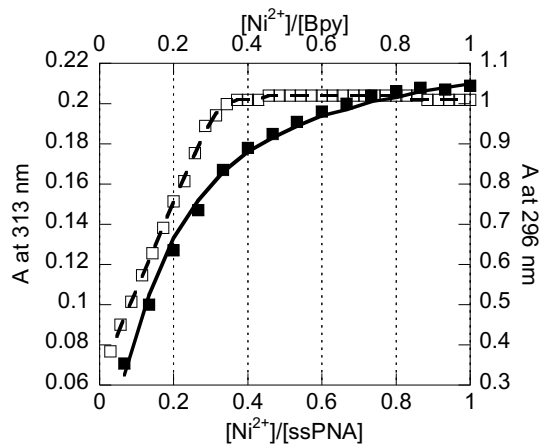
(a)



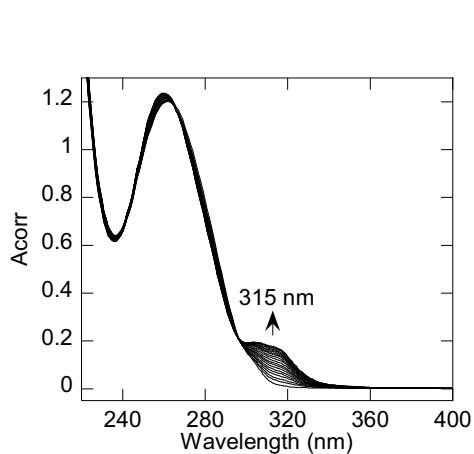
(b)



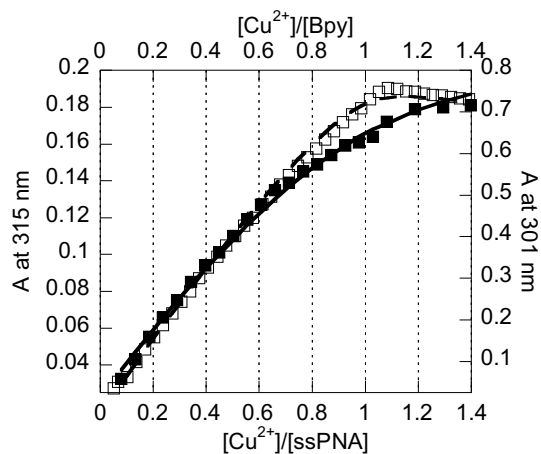
(c)



(d)



(e)



(f)

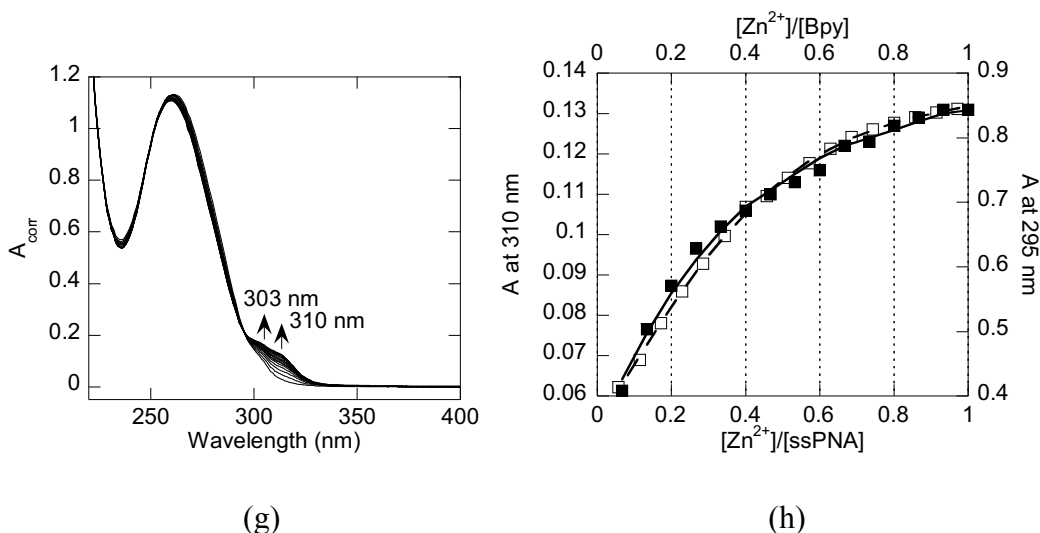
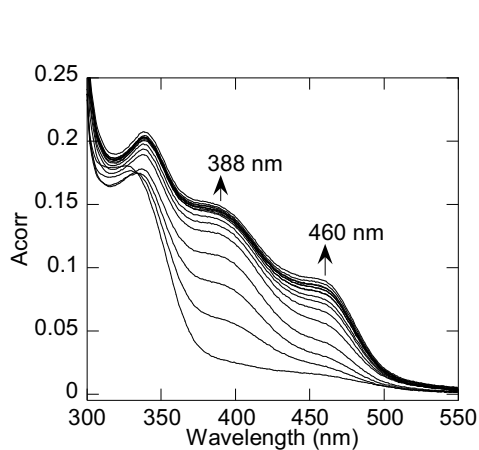


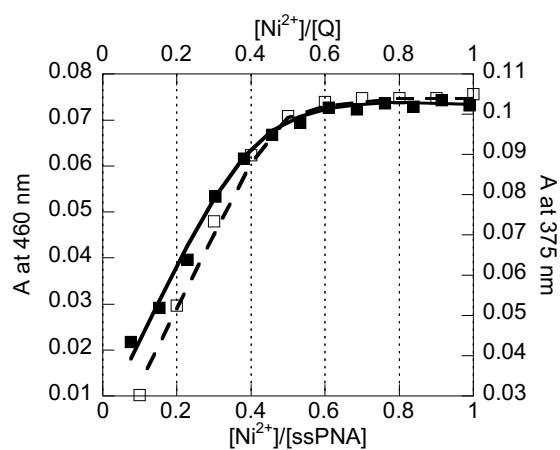
Figure II.7: Spectrophotometric titrations of **Bpy** (\square) and **Bpy₃ PNA** (\blacksquare) with Fe^{2+} (a and b), Ni^{2+} (c and d), Cu^{2+} (e and f) or Zn^{2+} (g and h). The lines through the data in (b), (d), (f) and (h) represent simulations of the titration curves for **Bpy** (dashed line) and **Bpy₃ PNA** (solid line) using HypSpec program with the stability constants given in Table II.3. The titration curves with Fe^{2+} , Ni^{2+} , Cu^{2+} and Zn^{2+} were monitored at 525 nm, 296 nm, 301 nm and 295 nm, respectively for **Bpy**. For **Bpy₃ PNA**, the titration curves were monitored at 304 nm, 313 nm, 315 nm and at 310 nm with Fe^{2+} , Ni^{2+} , Cu^{2+} and Zn^{2+} respectively.

The UV-Vis spectrum of the **Q** ligand is dominated by peaks at 240 nm and 300 nm (Figure II.18 i, k, m, o) attributed to π - π^* transitions of the ligand.²⁸ Unlike in the case of **Bpy₃ PNA**, the peaks due to the **Q** ligand are not masked by the nucleobase absorption peak at 260 nm. Therefore, the **Q₃ PNA** UV-Vis spectrum shows bands at 248 nm, 325 nm due to the ligand electronic transitions. Figure II.18 (i, k, m, o) show that the Ni^{2+} , Cu^{2+} , Zn^{2+} and Fe^{2+} coordination to the **Q** ligand leads to bathochromic shift in the 240 nm and 300 nm peaks. Similarly, the addition of Cu^{2+} and Zn^{2+} causes a decrease in the intensity of the absorption bands of **Q₃ PNA** at 248 nm and 325 nm decreases upon addition of Cu^{2+} and Zn^{2+} . The addition of Ni^{2+} , Cu^{2+} , or Zn^{2+} causes the appearance of a broad metal-to-ligand charge transfer band at 350 -500 nm²⁹⁻³⁰ (Figure II.8 a, c and e). These spectral changes establish that Cu^{2+} , Ni^{2+} and Zn^{2+} coordinate to the **Q** ligands in the **Q₃ PNA** triplex. On the other hand, the UV Vis

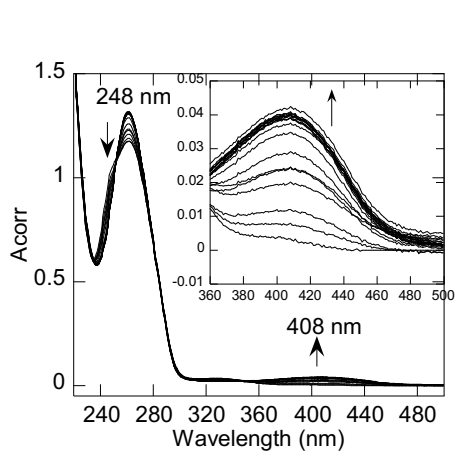
spectra show no evidence for the binding of Fe^{2+} to **Q₃ PNA** (Figure II.8g), a conclusion corroborated by the finding that the melting temperature of the **Q₃ PNA** was not affected by the presence of Fe^{2+} .



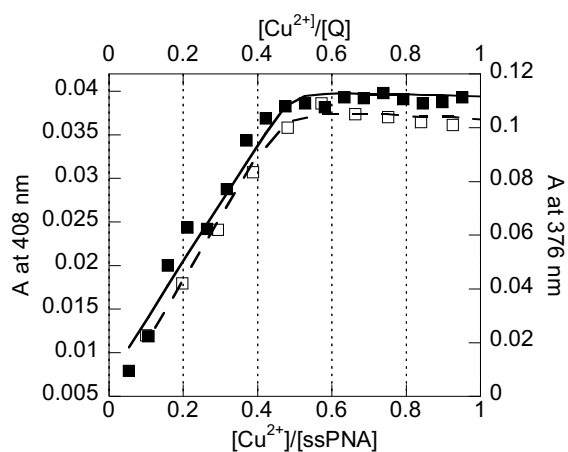
(a)



(b)



(c)



(d)

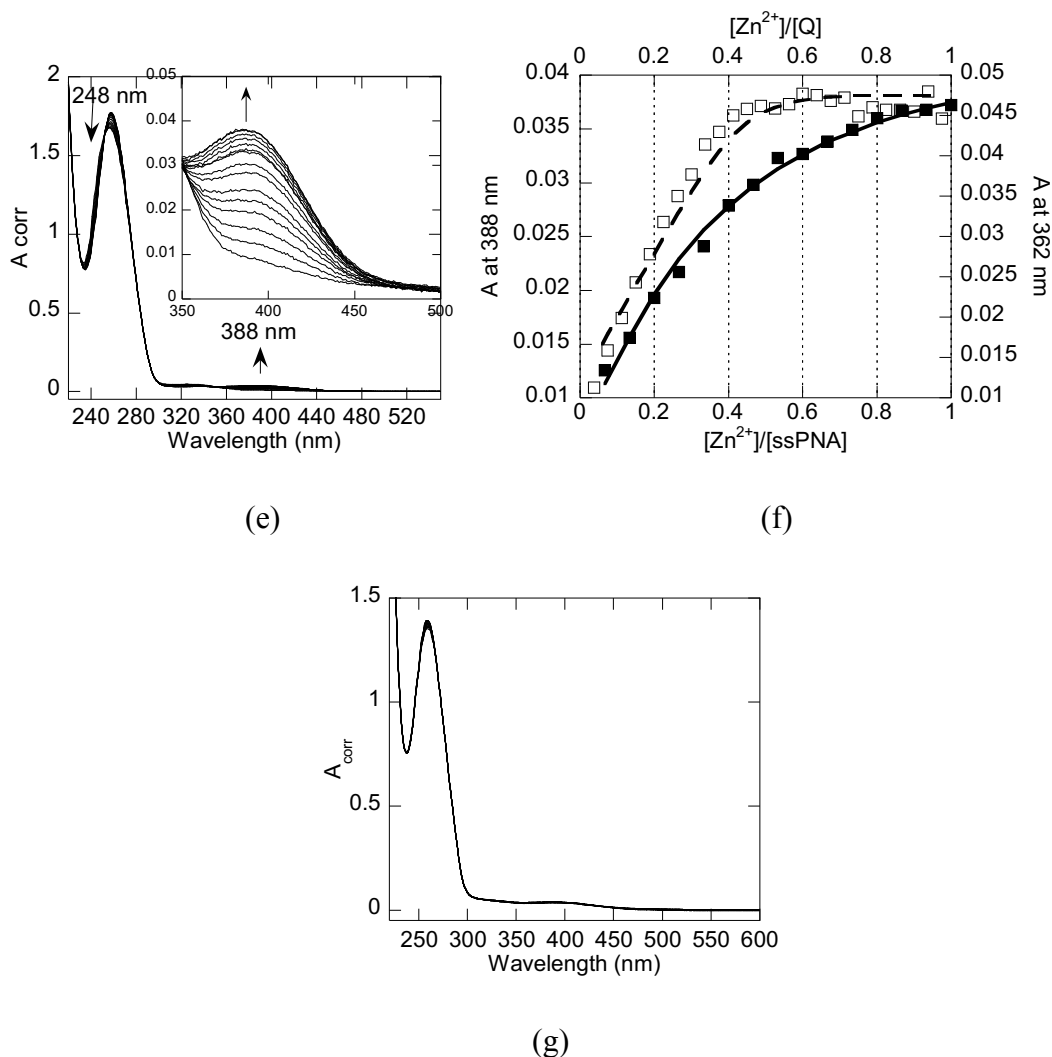


Figure II.8: Spectrophotometric titrations of **Q** (\square) and **Q₃ PNA** (\blacksquare) with Ni^{2+} (a and b), Cu^{2+} (c and d), Zn^{2+} (e and f) or Fe^{2+} (g). The titration curves with Ni^{2+} , Cu^{2+} and Zn^{2+} were monitored at 375 nm, 376 nm and 362 nm, respectively for **Q**. For **Q₃ PNA**, the titration curves were monitored at 460 nm, 408 nm and at 388 nm with Ni^{2+} , Cu^{2+} , and Zn^{2+} , respectively. Insets in (c) and (e) show absorbance change for peaks in visible region. No change in absorbance was observed upon addition of Fe^{2+} to **Q₃ PNA**. Solid lines (**Q₃ PNA**) and dashed line (**Q** ligand) through titration points in b, d and f are simulations obtained using HypSpec and the stability constants are from Table II.3.

The titration curves for the **Bpy** ligand with Fe^{2+} or Ni^{2+} and Cu^{2+} (Figure II.7 b, d and f) show an inflection point at $[\text{M}^{2+}]/[\text{ssPNA}]$ ratio of ~ 0.3 and 1, respectively, which suggests the formation of octahedral $[\text{Ni/Fe}(\text{Bpy})_3]^{2+}$ complex or $\text{Cu}(\text{Bpy})^{2+}$. In contrast, the titration curves for the **Bpy** ligand with Zn^{2+} and **Bpy₃ PNA** triplex with

Fe^{2+} , Ni^{2+} , Cu^{2+} or Zn^{2+} show more gradual changes in the absorbance making it difficult to ascertain the stoichiometry of the $[\text{M}(\text{Bpy})_n]^{2+}$ complexes from titration curves.

In the titration curves of **Q₃ PNA** with Cu^{2+} (Figure II.8), a sharp inflection point is seen at $[\text{M}^{2+}]/[\text{ssPNA}]$ ratio of ~ 0.5 , indicating the formation of a $[\text{CuQ}_2]$ complex. The change in absorbance upon addition of Ni^{2+} or Zn^{2+} to **Q₃ PNA** is gradual, which makes it unable for one to assign a stoichiometry to the complex formed, based on an UV-Vis titration curve.

In order to further study the stability and the stoichiometry of the complexes formed, we have analyzed the UV-Vis titration curves of the free **Bpy** and **Q** ligands and of the **Bpy₃** and **Q₃ PNA** triplexes using HypSpec refinement program³¹⁻³². The stability constants are listed in Table II.3 and the corresponding calculated speciation diagrams are shown in Figure II.9.

Table II.3: The stability constants for metal complexes formed with the free ligands or **L₃ PNA** obtained from UV-Vis data using HypSpec refinement program.

			Refinement condition	$\log \beta_1$	$\log \beta_2$	$\log \beta_3$
Fe^{2+}	Bpy	MES	refine β_3 ,	-	-	16.4 ± 0.1
		I=0.33	ignore β_1, β_2	-	-	16.7 ± 0.1
	Bpy ₃	MES		-	-	16.8 ± 0.4
Ni^{2+}	Bpy	NaPi	refine β_1, β_3 ,	5.7 ± 0.2	-	17.4 ± 0.02
			ignore β_2			
	Bpy ₃		refine β_3 ,	-	-	15.7 ± 0.03
Cu^{2+}	Bpy	NaPi	ignore β_1, β_2	-	-	15.6 ± 0.01
			refine β_1 ,	6.4 ± 0.01	-	-
	Bpy ₃		ignore β_2, β_3			
Zn^{2+}	Bpy	I=0.33	refine β_1 ,	5.7 ± 0.02	-	-
			ignore β_2, β_3			
	Bpy ₃		refine β_1, β_2 ,	5.2 ± 0.02	9.7 ± 0.02	-
Ni^{2+}	Q	NaPi	ignore β_3	-	-	-
			refine β_2 ,	-	11.9 ± 0.07	-
	Q ₃		ignore β_1, β_3	-	9.9 ± 0.7	-

Cu ²⁺	Q	-	12.4±0.05	-
	Q ₃	-	13.9±0.1	-
Zn ²⁺	Q	-	11.2±0.03	-
	Q ₃	-	10.2±0.04	

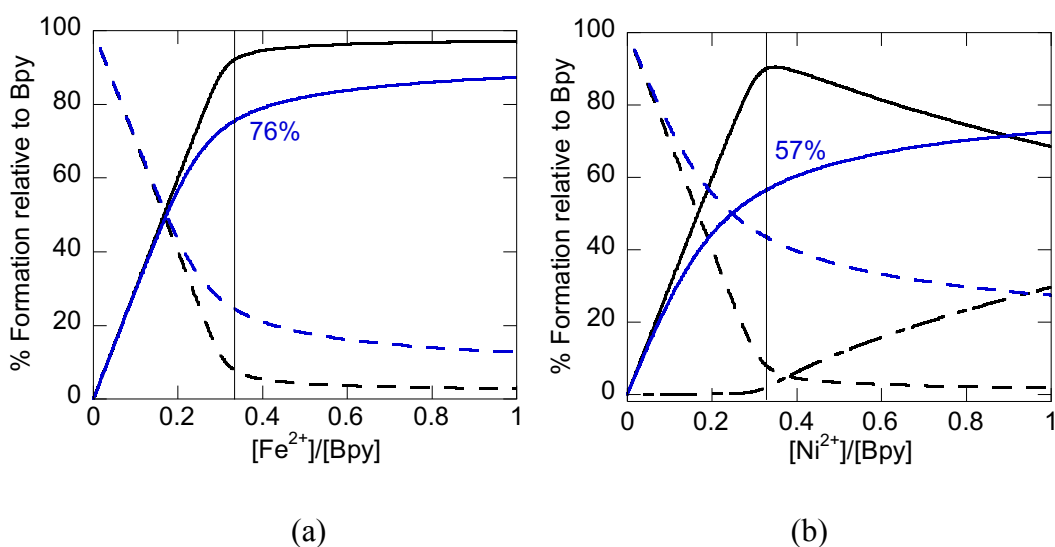
The free ligand-metal complex stability constants that we obtained by simulations are smaller than the reported values (Table II.3 and Table II.4). We attribute the discrepancy to the fact that our simulated stability constants are apparent and were determined from UV-Vis spectrometric titrations performed under different experimental conditions than the ones reported in literature (Table II.4).

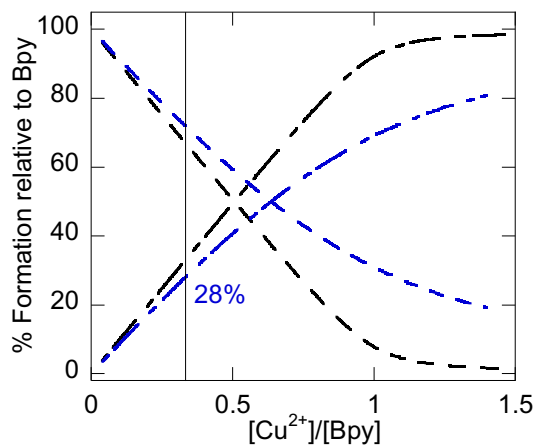
The HypSpec simulation analysis of the spectroscopic titrations shows that Fe²⁺ and Ni²⁺ form [M(**Bpy**)₃]²⁺ complexes with **Bpy**₃ PNA triplexes, but that these complexes are at most as stable as the corresponding complexes formed by these metal ions with free **Bpy**. In the triplexes, the three ligands are situated in close proximity to each other. Hence one could anticipate a stabilization of the [M(**Bpy**)₃]²⁺ complexes due to the supramolecular chelate effect. We attribute the fact that this stabilization does not occur due to the steric interactions between the metal complex and PNA triplex. These interactions could also explain why neither Ni²⁺ or Fe²⁺ cause an increase in the melting temperature of the **Bpy**₃ PNA triplex when compared to the unmodified triplex. Cu²⁺ and Zn²⁺ form mono- and bis-complexes respectively, with **Bpy**₃ PNA, corroborating our conclusion that the complexes of Cu²⁺ or Zn²⁺ with **Bpy** do not function as alternative metal-mediated base triplets in the **Bpy**₃ triplexes. Although three **Q** ligands are in close proximity of each other, Ni²⁺, Cu²⁺ and Zn²⁺ form bis [MQ₂] complexes with **Q**₃ PNA. We attribute this property to the high stability of square-planar MQ₂ complexes that can efficiently π -stack with adjacent nucleobases of the triplex.

Table II.4: Conditions for literature stability constants

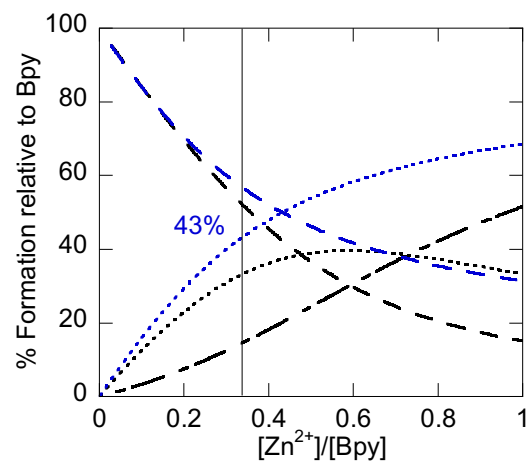
Complex	Stability constants	Method	Experimental conditions	Reference
Ni^{2+} -Bpy	$\log \beta_1=6.9$ $\log \beta_2=13.7$ $\log \beta_3=19.6$	Indirect spectrophotometric method where Cu^{2+} is used as a competing metal ion.	In aqueous-alcoholic solution (EtOH, 41.5% by wt) in the presence of KNO_3 (0.1M) as the electrolyte.	21
Fe^{2+} -Bpy	$\log \beta_1=4.21$ $\log \beta_3=17.07$	Spectrophotometric method	In aqueous solutions of $I=0.025$ in the presence of acetate and phthalate buffers at pH 4.00.	22
Zn^{2+} -Bpy	$\log \beta_1=5.16$ $\log \beta_2=9.62$ $\log \beta_3=13.36$	pH metric method	In aqueous solutions which contained KNO_3 (0.1M) as the electrolyte.	21
Cu^{2+} -Bpy	$\log \beta_1=8.15$ $\log \beta_2=13.65$ $\log \beta_3=16.95$	Partition method	Partition coefficients of Bpy ligand between buffers of $I=0.33$ and organic solvents were used to determine the given stability constants, valid in solution of 0.1 M KCl or KNO_3 .	24
Ni^{2+} -Q	$\log \beta_1=9.9$ $\log \beta_2=18.7$	Potentiometric titration	-	25
Zn^{2+} -Q	$\log \beta_1=8.52$ $\log \beta_2=15.83$	Solubility method	In aqueous solutions of 0.2 M sodium perchlorate, 0.2 M perchloric acid and 0.2 M sodium	23
Cu^{2+} -Q	$\log \beta_1=12.1$ $\log \beta_2=23.0$			

Speciation diagrams for free ligand **L** and for **L₃ PNA** in the presence of Fe^{2+} , Ni^{2+} , Cu^{2+} or Zn^{2+} are given in Figure II.9. At parity of concentration of ligand **L** in solution, the metal complex is present in lower concentration in solutions of **L₃ PNA** than in solutions of the free ligand. The relative population of the dominant $[\text{M}(\text{L})_x]^{2+}$ complex correlates with the relative increase in the stability of the **L₃ PNA** in the presence of one equivalent of metal ion per triplex, except in the case of Fe^{2+} and Ni^{2+} with **Bpy₃ PNA**. It is possible that a certain fraction Fe^{2+} is oxidized during the melting and annealing cycles, resulting in lower melting temperature (64 °C for Fe^{2+} vs 66 °C for Ni^{2+} , Table II.2) than predicted by the percentage of $[\text{Fe}(\text{Bpy})_3]^{2+}$ at 1 equivalent of Fe^{2+} per triplex ratio. The relative increase in melting temperatures of **Q₃ PNA** in the presence of one equivalent of Cu^{2+} (ΔT_m : 21 °C, 66% CuQ_2), Ni^{2+} (ΔT_m : 12 °C, 53% NiQ_2) or Zn^{2+} (ΔT_m : 5 °C, 38% ZnQ_2) correlates nicely with the percentage of $[\text{MQ}_2]$.

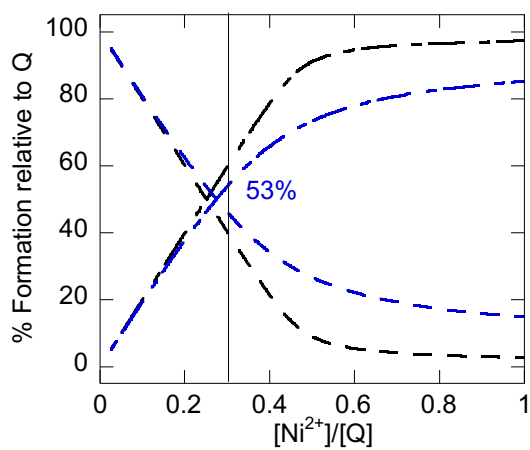




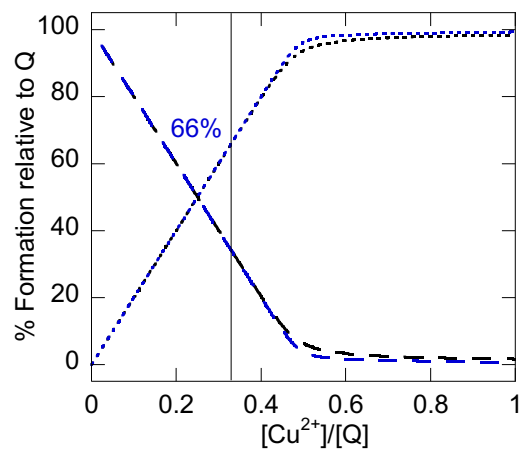
(c)



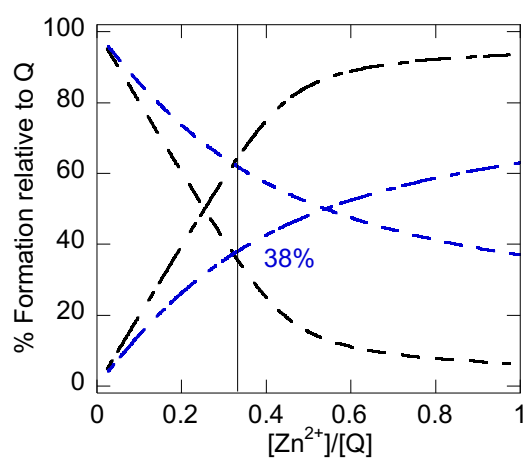
(d)



(e)



(f)



(g)

Figure II.9: Speciation diagrams for free Bpy/Q ligand (black lines) and Bpy₃/Q₃ PNA (blue lines) with (a) Fe²⁺, (b/e) Ni²⁺, (c/f) Cu²⁺ and (d/g) Zn²⁺ obtained using the stability constants from Table II.3. Solid line: [M(L)₃]²⁺; dotted line: [M(L)₂]²⁺; segment-dot line: [M(L)]²⁺; dashed line: free L. The vertical solid line goes through the 0.33 [M²⁺]/[L] or 1 eq of M²⁺ per L₃ triplex ratio. The percentage of the dominant [M(L)_x]²⁺ complex at 0.33 [M²⁺]/[L] or 1 eq of M²⁺ per L₃ triplex ratio is written on each figure.

The formation of CuQ₂ complexes in Q₃ PNA is corroborated by EPR spectra of solutions of the Q₃ PNA triplex in the presence of 0.5, 1.0, and 1.5 equivalents of Cu²⁺, which are similar to each other and indicate the formation of square planar [CuQ₂] complexes between the Cu²⁺ and the triplex irrespective of the amount of Cu²⁺ added to the solution.

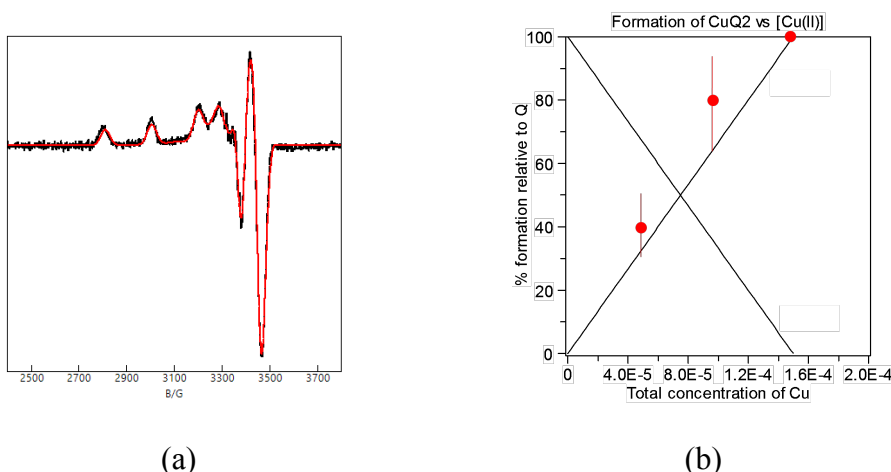


Figure II.10: (a) EPR spectrum (black line) of a sample of 100 μM Q₃ PNA triplex containing one eq. Cu²⁺ in pH 7.00 10 mM sodium phosphate buffer with 25% glycerol as a glassing agent. The red line represents a simulation with g values 2.048, 2.056, 2.223 and hyperfine A values 64.98 MHz, 94.26 MHz, and 608.3MHz, respectively. (b) Overlap of speciation diagram calculated with logβ₂=13.9 (Table II.3) for Q₃ PNA in the presence of Cu²⁺, with the %[CuQ₂] complex (red circles) measured by quantitation of the EPR spectra

II.3.3 Effect of Metal Coordination on Handedness of L₃ PNA

The PNA backbone is achiral. Hence the PNA triplexes adopt a preferred handedness only when a chiral unit is incorporated in the PNA oligomers.^{19, 33} The Q₃

PNA and **Bpy₃ PNA** triplexes contain an L-Lysine, causing them to adopt a left-handed helical structure as revealed by the negative features at 220 nm and 255 nm in the CD spectra (Figure II.11). Additionally, **Bpy₃ PNA** and **Q₃ PNA** triplexes, both in the absence and presence of metal ions, show a bisignate CD band in the presence of DiSC₂(5) dye molecules (Figure II.12). Specifically, **Bpy₃ PNA** shows a positive CD peak at 523 nm and a negative peak at 539 nm and **Q₃ PNA** shows a positive peak at 527 nm and a negative peak at 548 nm, regardless of the absence or presence of metal ions. Smith and co-workers reported that a left-handed PNA duplex exhibits bisignate CD peaks that are similar in peak signs and positions to those we observed for the triplexes.³⁴ Therefore, the left handedness of the triplexes is confirmed by the CD spectra of the triplex solutions to which DiSC₂(5) dye was added. The bisignate CD peaks obtained for triplex solutions are consistent with the binding mode in which dimeric units of DiSC₂(5) dyes form H-aggregates in a face-to-face orientation along the minor groove of the triplexes.³⁵

With one exception, namely **Bpy₃ PNA** in the presence of Cu²⁺, the CD spectra of the **Bpy₃ PNA** and **Q₃ PNA** triplexes in the presence of any of the four metal ions used in this study show negative peaks at 220 nm and 255 nm, indicating that the metal coordination does not affect the triplex left handedness. L-Lysine induces a preferred left handed structure in a PNA duplex³⁶ or a triplex by hydrogen bonding interaction between L-Lysine- side chain and PNA backbone and adjacent nucleobases. The chirality is transferred along the duplex or triplex through π -stacking interaction of nucleobases.

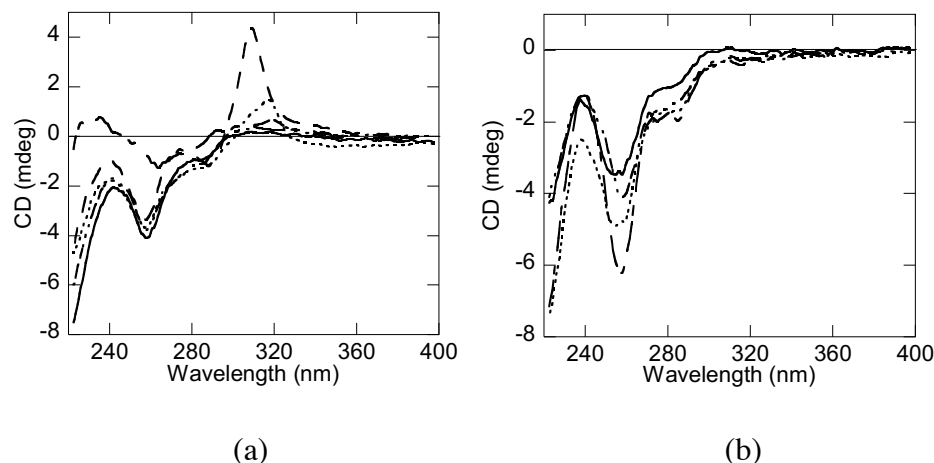


Figure II.11: CD spectra for 5 μM solutions of (a) Bpy_3 PNA and (b) Q_3 PNA in the absence (solid line) and presence of one equivalent of Fe^{2+} (dashed line), Ni^{2+} (dotted line), Cu^{2+} (dotted-dashed line) or Zn^{2+} (double dotted-double dashed line).

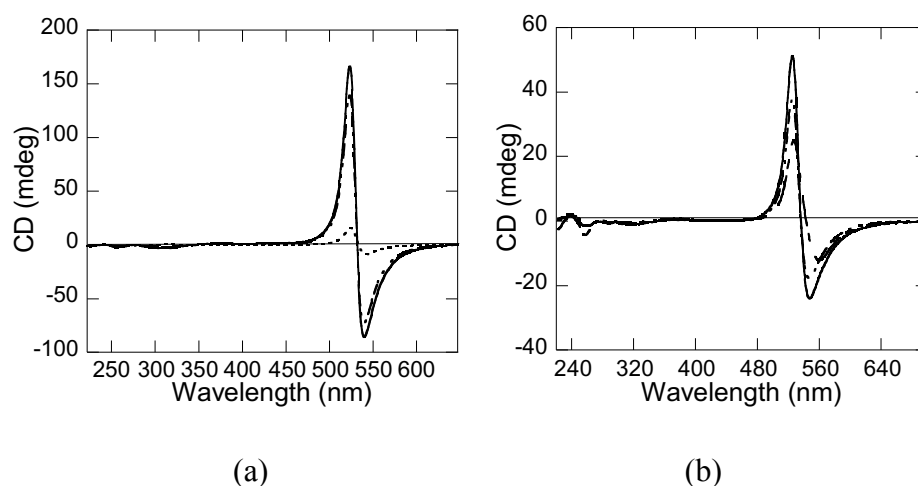


Figure II.12: CD spectra for 2 μM Bpy_3 PNA solutions with $\text{DiSC}_2(5)$ dye in the absence (solid line) and presence of one equivalent of Ni^{2+} (dotted line) and Zn^{2+} (double dotted-double dashed line) (a), for 2 μM Q_3 PNA solutions with $\text{DiSC}_2(5)$ dye in the absence (solid line) and presence of one equivalent of Cu^{2+} (dotted-segmented line) and Zn^{2+} (double dotted-double dashed line) (b). Concentration of the dye in the solution was 5 μM . Triplex solutions were prepared in pH 7.00, 10 mM sodium phosphate buffer and 10 % methanol.

Cu^{2+} forms mono- $\text{Cu}(\text{Bpy})^{2+}$ complexes with **Bpy₃ PNA**, as evident from analysis of UV-Vis titration curves (Figure II.7 e, f and Table II.3). The $\text{Cu}(\text{Bpy})^{2+}$ or uncoordinated **Bpy** may protrude out from the triplexes and break the π -stacking

interactions among nucleobase triplets in the **Bpy₃ PNA**. This could be the reason why **Bpy₃ PNA** shows very weak or no CD activity in the presence of one equivalence of Cu²⁺. The 255 nm and 220 nm CD peak intensities of **Bpy₃ PNA** decrease in the presence of Fe²⁺, Ni²⁺ or Zn²⁺ (Figure II.11 a), which is attributed to the octahedral or tetrahedral geometry of the respective metal complexes negatively impacting the π -stacking of the nucleobase triplets in **Bpy₃ PNA**. In contrast, the intensity of the CD peaks of **Q₃ PNA** at 255 nm and 220 nm increases in the presence of Cu²⁺, Ni²⁺ or Zn²⁺ (Figure II.11 b). The increase correlates with percent [M \mathbf{Q}_2] present in solution estimated from the speciation diagrams (Figure II.9 e-f). [M \mathbf{Q}_2] complexes are square planar and thus can efficiently π -stack with adjacent nucleobases of the **Q₃ PNA**, effectively transferring the left-handedness induced by the terminal L-Lys. The negative and positive effects by the metal complexes on π -stacking of the nucleobases of the triplexes are consistent with our UV-melting results.

The most striking features in the CD spectra of **Bpy₃ PNA** triplex in the presence of one equivalent of Ni²⁺ (~318 nm) or Fe²⁺ (~308 nm) are the peaks from 300 – 330 nm. These CD signals correspond to the π – π^* transitions of the coordinated Bpy ligands in [M(**Bpy**)₃]²⁺ complexes and suggest that one enantiomer for [M(**Bpy**)₃]²⁺ predominates inside the **Bpy₃ PNA** triplex. A similar UV-CD feature was observed recently for [Ni(**Bpy**)₃]²⁺ situated at the core of a 3-way DNA junction and was interpreted as indicative of the Λ conformation of the complex.³⁷ The Cotton effects seen for Ni²⁺ and Fe²⁺ tris-Bpy complexes are consistent with Λ -isomers of each.³⁸⁻⁴¹

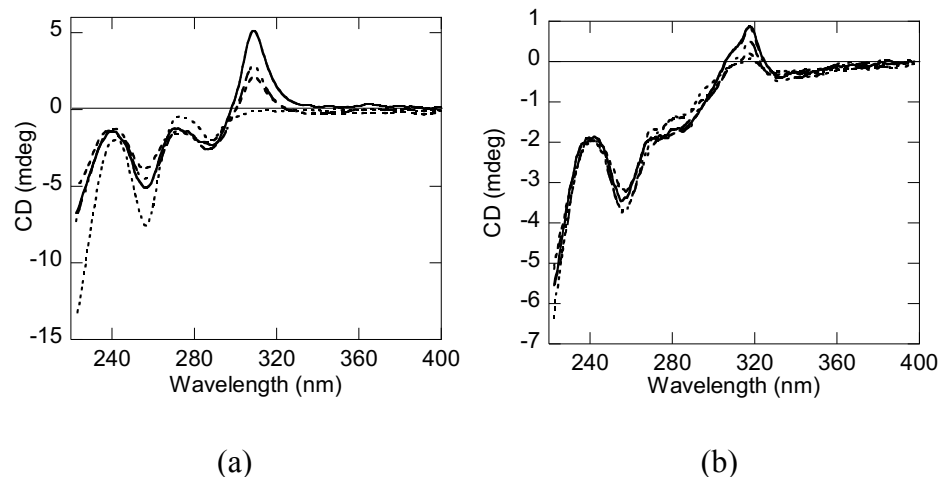


Figure II.13: CD spectra for 5 μM **Bpy₃ PNA** solutions in the presence of (a) 0, 0.5, 0.7, 0.9 equivalents of Fe^{2+} and (b) 0.2, 0.4, 0.7, 0.9 and 1.0 equivalents of Ni^{2+} .

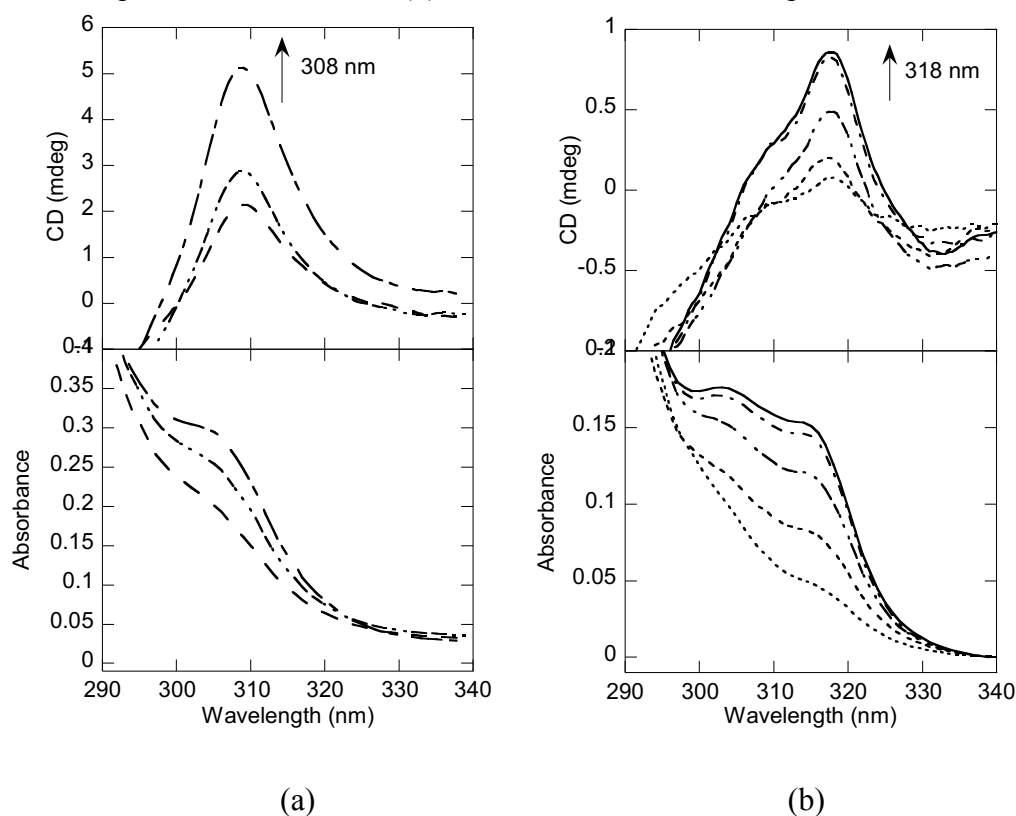


Figure II.14: Concomitant increase in CD (top) and UV absorption (bottom) band intensities in 300-330 nm region with addition of increasing amounts of (a) Fe^{2+} or (b) Ni^{2+} to **Bpy₃ PNA**.

We also measured UV-Vis and CD spectra of **Bpy₃ PNA** annealed in the presence of different equivalents of Fe^{2+} or Ni^{2+} per triplex. The data were used to

construct the titration curves given in Figure II.15. The intensity of the CD and UV-absorption at 300-330 nm increases with the amount of metal ion added to the solution up to one equivalent of metal per triplex (Figure II.13 and Figure II.14). These curves confirm the formation of $[M(\text{Bpy})_3]^{2+}$ complexes in the triplexes.

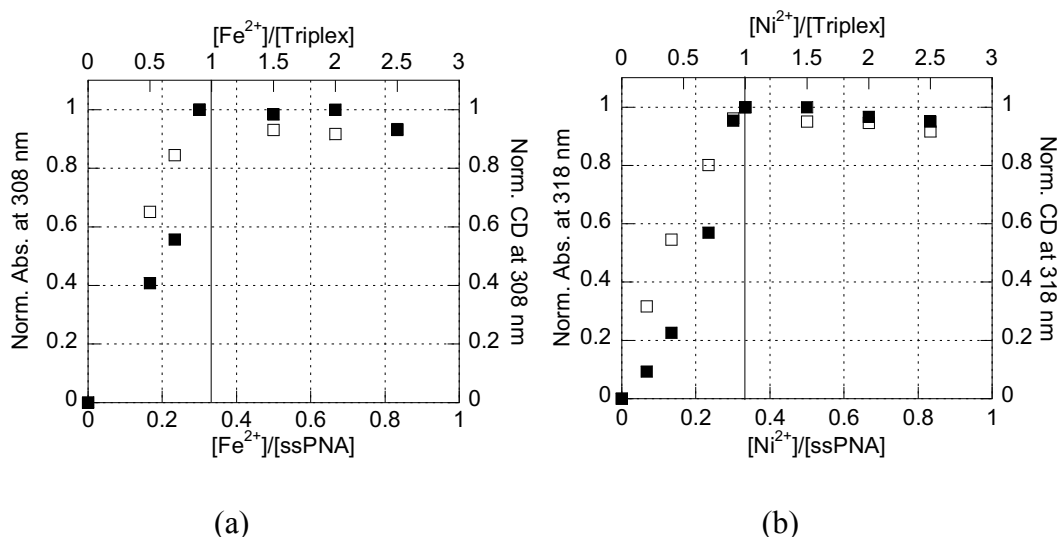


Figure II.15: CD (■) and UV (□) titration curves monitored at 308 nm in the presence of (a) Fe^{2+} and at 318 nm in the presence of (b) Ni^{2+} , with 5 μM Bpy_3 PNA.

II.4 Conclusions

In this study, we showed that $[\text{Fe}(\text{Bpy})_3]^{2+}$, $[\text{Ni}(\text{Bpy})_3]^{2+}$, $[\text{Zn}(\text{Bpy})_2]^{2+}$ and $\text{Cu}(\text{Bpy})^{2+}$ complexes form within PNA triplexes that contain three **Bpy** ligands situated in complementary positions. We also showed that $[\text{NiQ}_2]$, $[\text{CuQ}_2]$ and $[\text{ZnQ}_2]$ complexes form with **Q₃** PNA triplexes although three **Q** ligands are situated in complementary positions in each triplex. $[\text{Fe}(\text{Bpy})_3]^{2+}$, $[\text{Ni}(\text{Bpy})_3]^{2+}$, $[\text{NiQ}_2]$, $[\text{CuQ}_2]$ and $[\text{ZnQ}_2]$ act as metal-based alternative base pairs or triplets and increase the thermal stability of the triplexes. The thermal melting and UV titration results suggest that the stabilization effect arising from the coordination bonds, which are much stronger than hydrogen bonds within the nucleobase triplets, is mitigated by the steric interactions

between the octahedral complexes and the triplexes. The handedness of the PNA triplexes are not affected by the metal ions and in some cases, the chirality of the metal complexes depends on the chirality of the PNA triplex. These findings are of value in the design of hybrid inorganic-nucleic acid architectures.

II.5 Material and Methods

II.5.1 Solid-Phase PNA Synthesis

The Boc/Z-A and T PNA monomers were purchased from Polyorg and used with no further purification. The **Q** and **Bpy** PNA monomers were synthesized according to previously published procedures.^{6-7, 10} PNA oligomers were synthesized by solid phase Boc-protection peptide synthesis strategy.⁴² p-Methyl-Benzhydrylamine resin.HCl (1.03 meq/g, Peptides International) was used as the solid support for PNA synthesis. The resin was downloaded to between 0.10-0.05 meq/g by preloading with an L-lysine using Boc-Lys(2-Cl-Z)-OH (Fluka). Boc-Lys(2-Cl-Z)-OH was coupled on to the resin using 1-[Bis(dimethylamino)methylene]-1*H*-1,2,3-triazolo[4,5-*b*]pyridinium3-oxid hexafluorophosphate (HATU, Chem-Impex) and *N,N*-Diisopropylethylamine (DIEA, Sigma Aldrich) as the coupling reagent and the base, respectively. *N,N,N',N'*-Tetramethyl-*O*-(1*H*-benzotriazol-1-yl)uronium hexafluorophosphate (HBTU, Chem-Impex) and *N,N*-Dicyclohexylmethylamine (MDCHA, TCI America) were used as the coupling reagent and the base for the couplings of Boc-PNA monomers, **Q** or **Bpy** PNA monomers. PNA oligomers were cleaved from the resin using *m*-cresol/thioanisole/TFMSA/TFA (1:1:2:6) and precipitated using cold diethyl ether. Purification of the PNA was done by reversed-phase HPLC equipped with a C18 silica column on a Waters 600 controller and pump. Absorbance was monitored with a Waters 2996 photodiode array detector. PNA

oligomers were characterized by MALDI-ToF-MS on an Applied Biosystems Voyager biospectrometry workstation using α -cyano-4-hydroxycinnamic acid as the matrix (10 mg/ml in water/acetonitrile, 0.1% TFA).

PNA stock solutions were made in nano-pure water. The concentrations of the PNA solutions were determined by UV-vis spectroscopy at 90 °C using 8600, 13700, 9770 and 2574 cm⁻¹ M⁻¹ as the extinction coefficients at 260 nm for A, T, **Bpy** and **Q** PNA monomers, respectively.⁴³ The 5 μ M solutions of the PNA triplexes were prepared in pH 7.00, 10 mM sodium phosphate (NaPi) buffer except for the solutions of the **Bpy**₃ **PNA** triplex used in the study of interactions with Fe²⁺, which were prepared in pH 6.50, 10 mM 2-(N-morpholino)ethanesulfonic acid (MES) buffer. The solutions of PNA triplexes were annealed by cooling from 90 °C to 15 °C at a rate of 1 °C/min in a Varian Cary 300 spectrophotometer equipped with a programmable temperature block.

II.5.2 Melting Curves

Variable temperature UV-vis experiments were performed in a Varian Cary 300 spectrophotometer equipped with a programmable temperature block in 1 cm optical-path, quartz cells. The melting curves were recorded in the presence of one or three equivalents of metal ions per triplex, over a temperature range of 15-90 °C for both cooling (annealing) and heating (melting) cycles at a rate of 1 °C/min. The samples were kept for 10 minutes at 90 °C before cooling and at 15 °C before heating. Samples that contained Fe²⁺ were prepared in the glove box and melting experiments were performed in air-tight cuvettes under nitrogen. The melting temperature was determined by using the first derivative plots of the thermal melting profiles (Figure II.17).

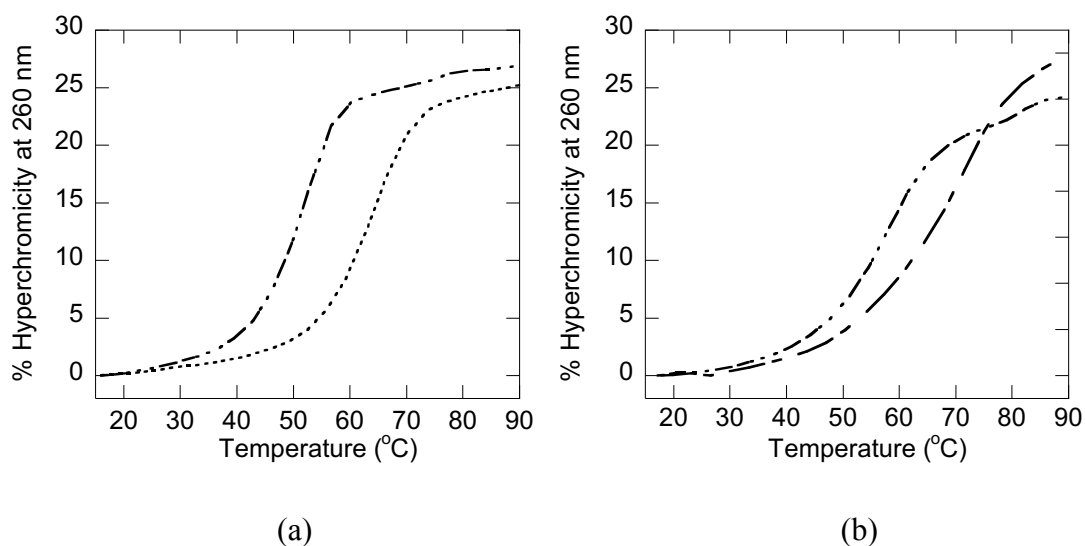
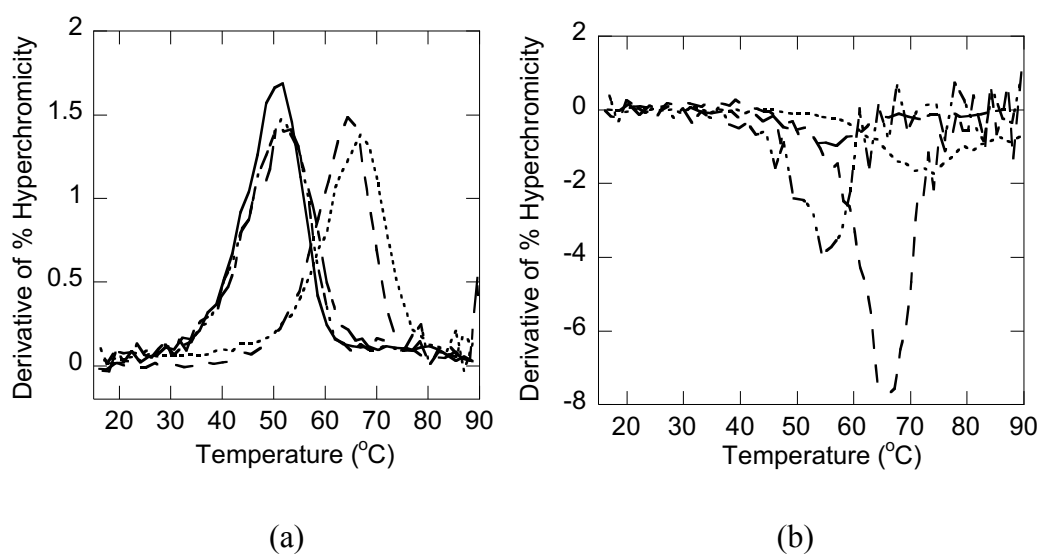


Figure II.16: Melting curves for **Bpy₃ PNA** (a) and **Q₃ PNA** monitored at 260 nm in the presence of three equivalents of Ni²⁺ (dotted line), Cu²⁺ (dotted-dashed line) or Zn²⁺ (double dotted-double dashed line)



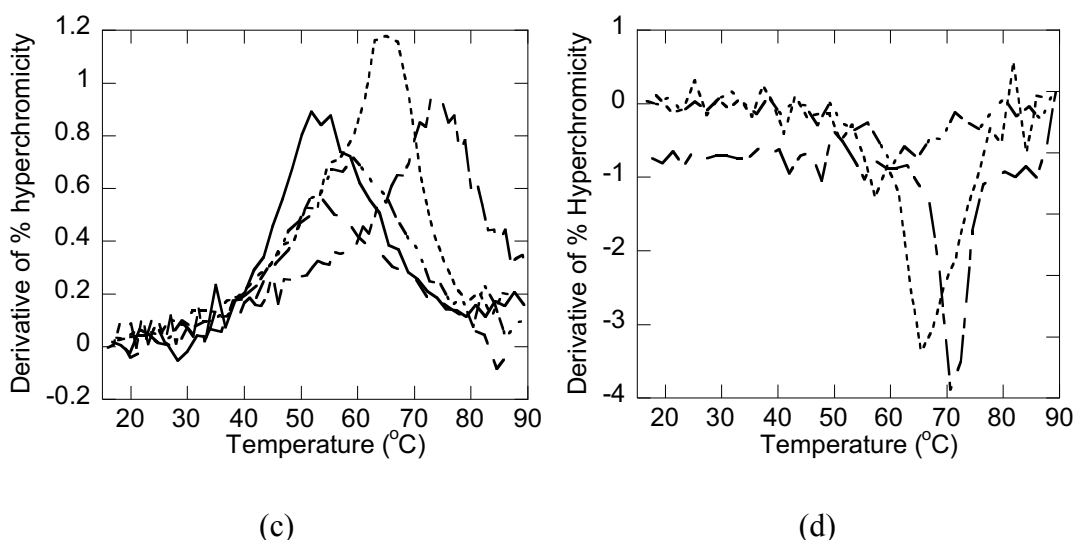
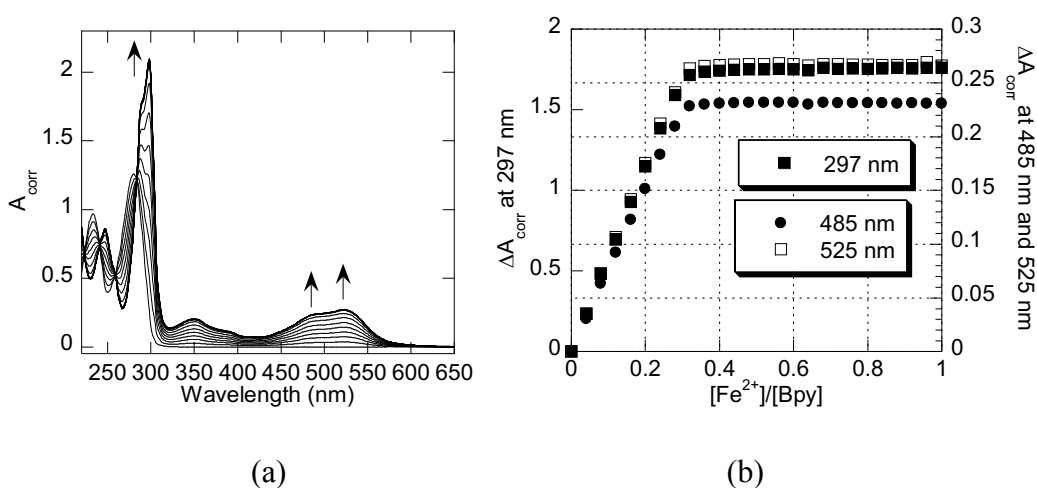
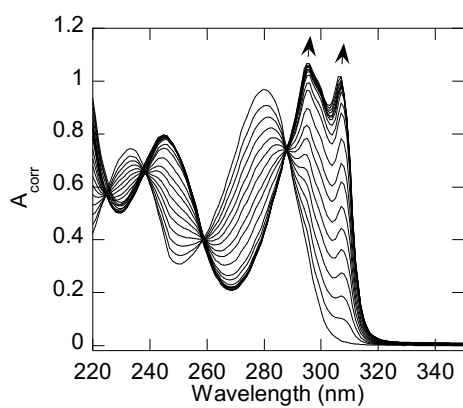


Figure II.17: First derivative plots of melting curves to determine the melting temperatures reported in Table II.2, monitored at 260 nm (a and c) or at λ_{ML} (d and e) for **Bpy**₃ PNA (a and b) and **Q**₃ PNA in the presence of one equivalent of Fe²⁺ (dashed line), Ni²⁺ (dotted line), Cu²⁺ (dotted-dashed line) or Zn²⁺ (double dotted-double dashed line).

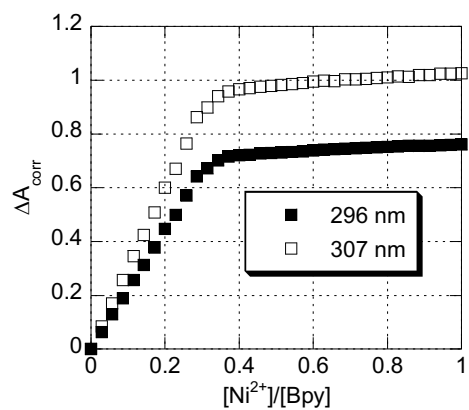
II.5.3 Spectrophotometric Titrations

The binding of metal ions to free ligands and ligand-modified **L**₃ PNA was determined by spectrophotometric titrations performed in Varian Cary 50 spectrophotometer. First, titrations of **Bpy** or **Q** ligand were done with Fe²⁺, Ni²⁺, Cu²⁺ and Zn²⁺ to determine the nature of complexes formed by each ligand with the metal ions under our experimental conditions (Figure II.18).

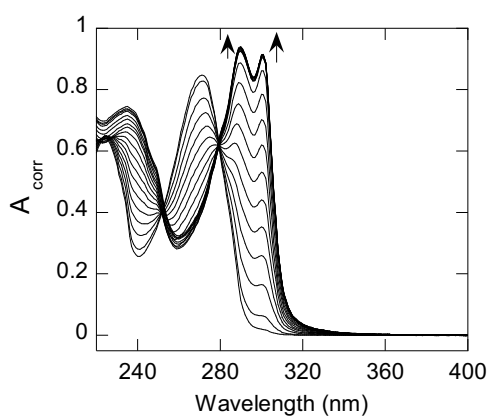




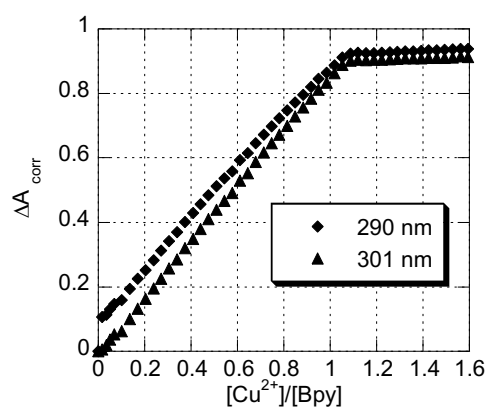
(c)



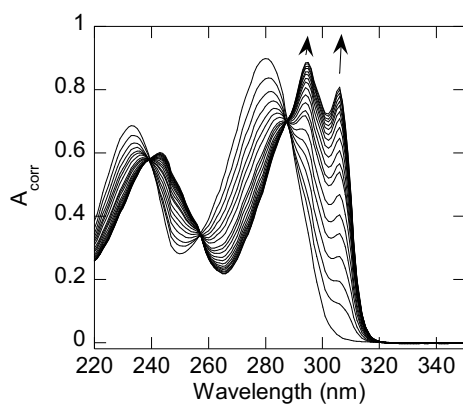
(d)



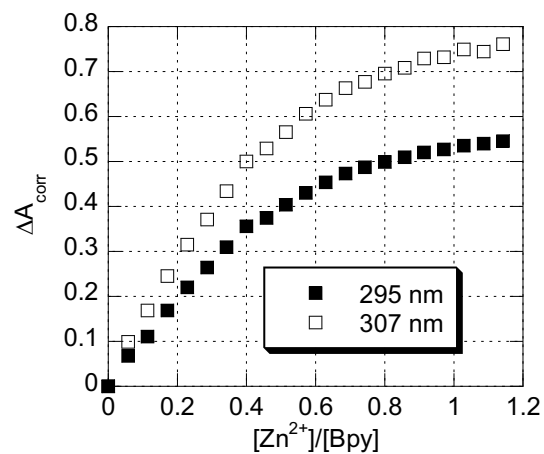
(e)



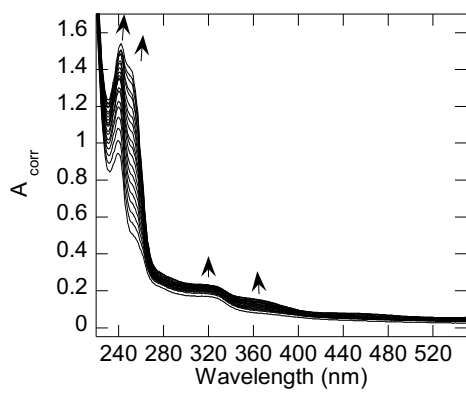
(f)



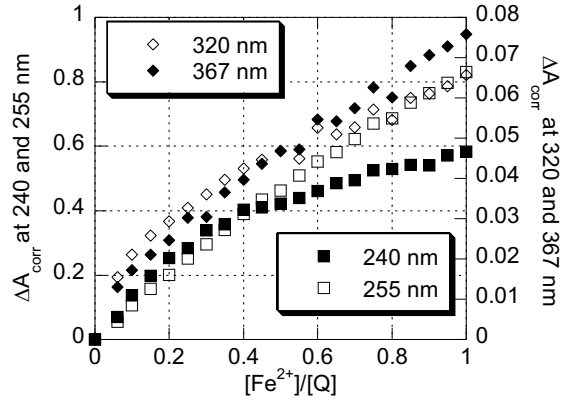
(g)



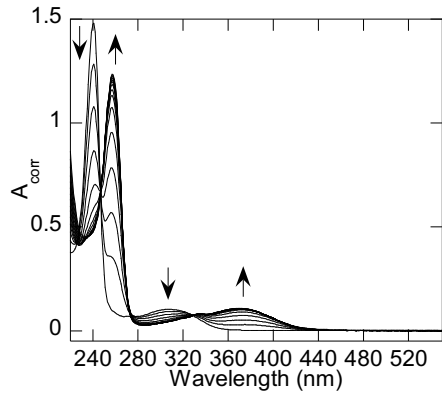
(h)



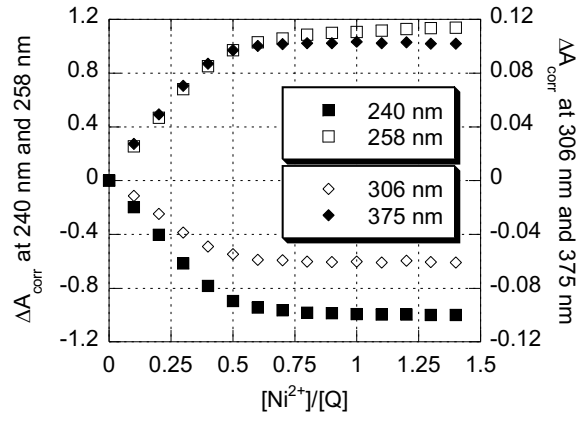
(i)



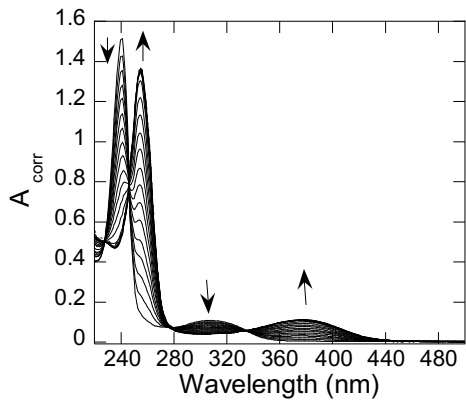
(j)



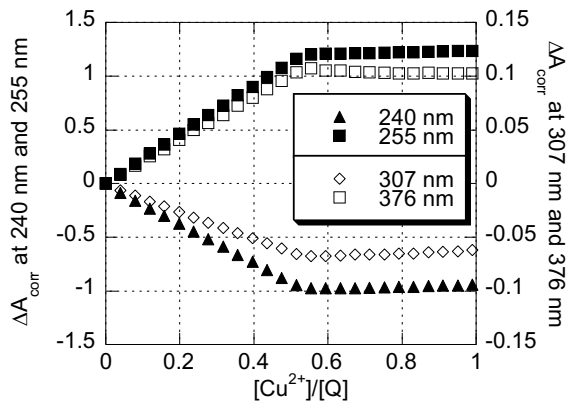
(k)



(l)



(m)



(n)

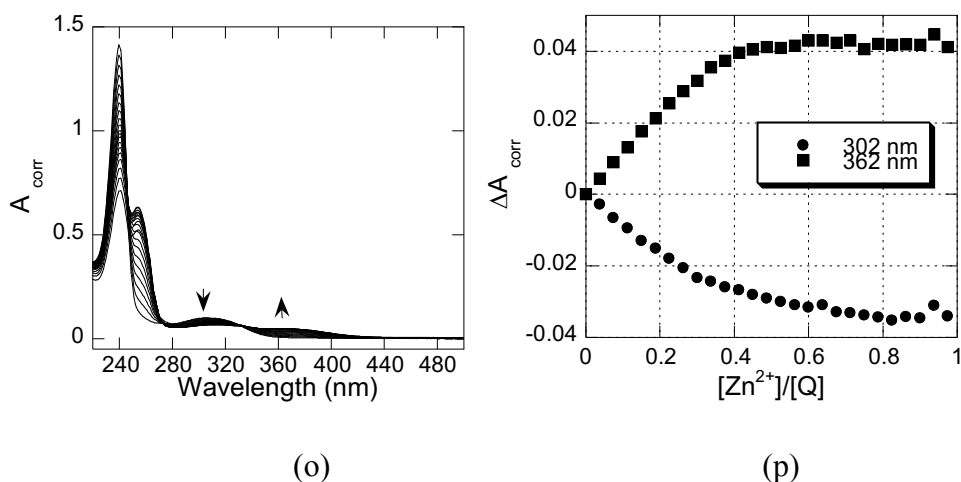


Figure II.18: Spectrophotometric titrations of **Bpy** ligand with Fe^{2+} (a and b), Ni^{2+} (c and d), Cu^{2+} (e and f) or Zn^{2+} (g and h) and of **Q** ligand with Fe^{2+} (i and j) Ni^{2+} (k and l), Cu^{2+} (m and n) or Zn^{2+} (o and p).

Titration were carried out by addition of aliquots of known volumes and concentrations of metal ion solutions in water to ligand or **L₃ PNA** solutions. Titrations of **Bpy₃ PNA** or **Bpy** with Ni^{2+} , Cu^{2+} and Zn^{2+} were done in pH 7.0 10 mM sodium phosphate buffer while those with Fe^{2+} were done in pH 6.50 10 mM MES buffer. The concentrations of **Bpy** solutions were 70 μM and 100 μM for the titration with Ni^{2+} , Cu^{2+} , Zn^{2+} and Fe^{2+} , respectively. **L₃ PNA** triplex concentration was 5 μM . Metal ion concentrations for the titrations with **Bpy** were 1000 μM (Ni^{2+}), 400 μM (Cu^{2+}), 2000 μM (Zn^{2+}) and 2000 μM (Fe^{2+}) and for the titrations with **Bpy₃ PNA** were 500 μM (Ni^{2+}), 400 μM (Cu^{2+}), 500 μM (Zn^{2+}) and 1500 μM (Fe^{2+}). The **Bpy₃** and **Q₃ PNA** solutions for titrations with Fe^{2+} were prepared in the glove box and the titrations were performed using an air-tight titration set-up. **Bpy** ligand and **Bpy₃ PNA** was titrated with Fe^{2+} and Ni^{2+} , respectively, in solutions in which the ionic strength was controlled and in solutions in which it was not controlled (Figure II.19). Comparison of these

titrations showed that ionic strength had no significant effect on the stability constants (Table II.3).

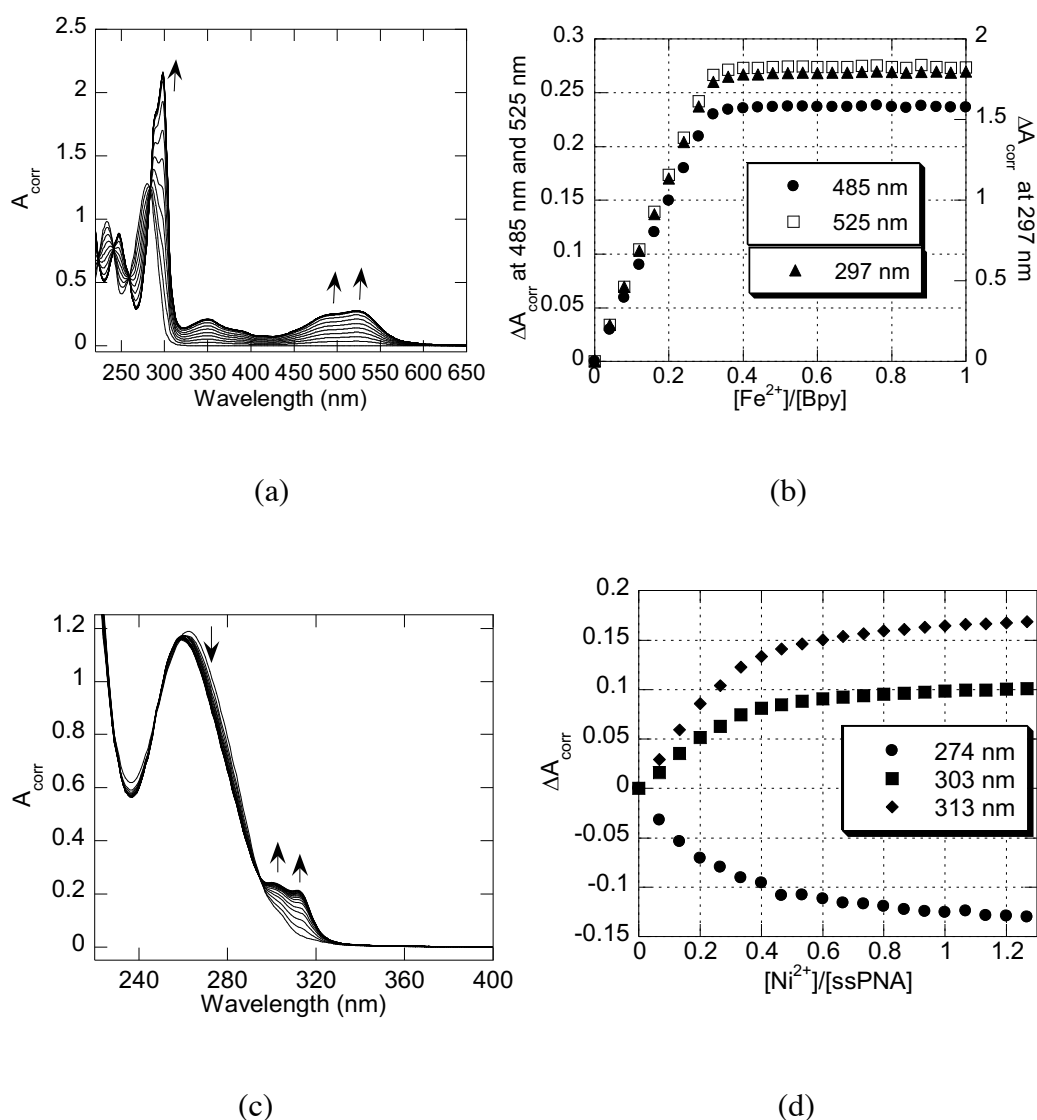


Figure II.19: Spectrophotometric titrations of **Bpy** ligand with Fe^{2+} (a and b) and **Bpy₃ PNA** with Ni^{2+} (c and d) at $I=0.33$. Ionic strength of the solution was adjusted with KCl. Concentrations of **Bpy**, **Bpy₃ PNA** and Ni^{2+} were similar to non-ionic strength controlled titrations.

Concentration of **Q** ligand was 40 μM for titrations with Ni^{2+} (2000 μM), Cu^{2+} (500 μM) and Zn^{2+} (500 μM) and that was 30 μM for the titration with Fe^{2+} (3000 μM). 5 μM solutions of **Q₃ PNA** were titrated with Cu^{2+} (400 μM), Zn^{2+} (500 μM) and Fe^{2+} (1500 μM). Concentration **Q₃ PNA** was 25 μM for the titration with Ni^{2+} (500 μM).

Both **Q** ligand and **Q₃ PNA** titrations with Ni²⁺, Cu²⁺ or Zn²⁺ were performed in 10 mM pH 7.00 sodium phosphate buffer while those with Fe²⁺ were done in 10 mM pH 6.5 MES buffer.

The absorbance was corrected for the dilution using the formula $A_{corr} = A_{measured} \times \frac{(nV_i + V)}{V}$, where n is the number of metal ion additions, V_i is the volume of the metal ion added during each addition and V is the initial volume in the cuvette. The change in the absorbance (ΔA) was normalized using the formulas $\Delta A_{ni} = A_{ni} - A_{initial}$ and $Norm \Delta A = \Delta A_{ni} / \Delta A_{final}$, where A_{ni} is the absorbance after each addition n_i of metal ion.

II.5.4 HypSpec Data Simulations

Spectrophotometric data were simulated using the refinement program HypSpec to obtain stability constants.³¹ First, we determined the number of absorbing species present in the system based on factor analysis. The models were chosen to ignore or refine log β based on how many absorbing species are present. The combinations of log β were altered, to ignore or refine and the initial input values of log β , to get the output log β s to converge. Wavelengths were chosen to include the maximum absorbance for each species in the solution. It is enough to measure absorbance at a single wavelength to calculate stability constants from absorbance data. However, it is better to select a few wavelengths. These wavelengths should ideally be selected near the maximum molar absorbance of each of the species present.³¹ HypSpec software requires use of an experimental error function. Experimental error function for our instrument was determined by making repeat measurement of Holmium oxide filter (UV/Visible region) or 100 mg/l H⁺/K₂Cr₂O₇ (235-310 nm).

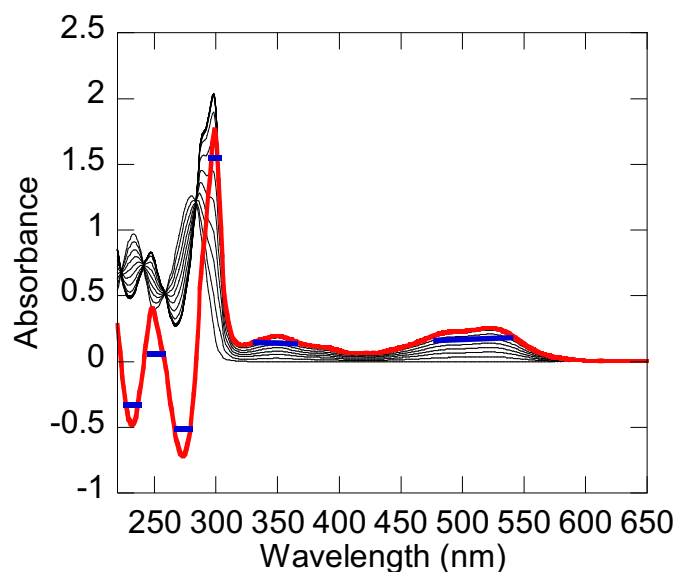


Figure II.20: UV-Vis spectra for the titration of **Bpy** in pH 6.50 10 mM MES buffer with Fe^{2+} . Wavelengths for which the change in absorbance was within 70% of the maximum change in the absorbance within the same band were used first in HypSpec simulations to obtain the stability constants. These wavelengths are identified by blue lines. The red line shows the difference between the initial and final spectra in the titration.

First, we simulated the UV-Vis titrations of 100 μM **Bpy** ligand in pH 6.5 MES buffer in the presence of increasing amount of Fe^{2+} using the Hyppec software over wavelength range for which the change in absorbance was within 70% of the maximum change in the absorbance within the same band (Figure II.20), using the holmium oxide filter or $\text{H}^+/\text{K}_2\text{Cr}_2\text{O}_7$ as the error functions. Then, we altered the span of the wavelength range to get sigma close to one. Regardless of the experimental error function or wavelength ranges we used, similar stability constants were obtained. Sigma was variable (Table II.5). Only when sigma is close to one, one can tell that the data has been fitted within the experimental error.

Table II.5: Stability constants obtained with two error functions and different wavelength ranges used in the HypSpec simulations.

Wavelength range (nm)	H ⁺ /K ₂ Cr ₂ O ₇ error function		holmium oxide filter error function	
	log β_3	σ	log β_3	σ
227-237, 245-252, 266-279, 294-303, 327-370, 472-543	16.4386±0.0183	5.6082	16.4386±0.0183	0.51989
227-237, 245-252, 266-279, 294-303	16.423±0.0179	5.1528	16.423±0.0179	0.47768
486-488, 524-526, 349-352, 247-248, 233-234	16.4746±0.0187	1.0091	16.4746±0.0187	0.093547
486-488, 524-526, 349-352, 298, 247-248, 233-234	16.4564±0.0182	1.8661	16.4564±0.0182	0.17299
349-352, 247-248, 233-234	16.4304±0.0174	0.73572	16.4304±0.0174	0.068202

It was possible to get sigma close to one when the H⁺/K₂Cr₂O₇ error function was used and wavelength range was chosen to include the absorbance range of the error function. H⁺/K₂Cr₂O₇ error function has absorbance data up to 1.4, the typical absorbance limit for our titration as well. When the wavelength 298 nm at which absorbance was ~2, was included in the simulation, sigma increased from 1.0091 to 1.8661 (Table II.5). The holmium oxide filter has absorbance up to 3. Detector of our instrument saturates around 2 absorbance units. Therefore, the H⁺/K₂Cr₂O₇ error function was used for the simulations and the data were simulated in the wavelength ranges within which absorbance is less than 1.4 and fine-tuned the wavelength range to get sigma closest to one. In the case of PNA triplex simulations, 260 nm region was not used as it accounts for nucleobase absorption. Multiple trials of titrations were fitted to get the final log β reported here.

II.5.5 EPR Spectroscopy

X-band EPR spectra were recorded on a Bruker 300 spectrometer equipped with an Oxford ESR-910 liquid helium cryostat. The microwave frequency was calibrated with a frequency counter and the magnetic field with an NMR gaussmeter. A modulation frequency of 100 kHz was used for all EPR spectra. The quantification of all signals is relative to a [Cu(EDTA)] spin standard. The concentration of the standard was derived from an atomic absorption standard (Aldrich). Temperature calibrations were performed using devices from Lake Shore Cryonics. The spectra were recorded at 17 K under non-saturating power conditions. The EPR simulation software (Spin Count) was written by Professor Michael P. Hendrich.⁴⁴ Samples containing 100 μ M **Q₃ PNA** triplex and 0.5, 1.0, and 1.5 eq. Cu²⁺ in pH 7.0 10 mM NaPi buffer with 25% glycerol as a glassing agent were kept at 95 °C for 10 min, then slowly cooled to room temperature, transferred to an EPR tube, and frozen.

II.5.6 CD Spectroscopy

The CD spectra were measured at 20 °C at a rate of 50 nm/min and 10 scan accumulation on a JASCO J-715 spectropolarimeter equipped with a thermoelectrically controlled, single-cell holder. For the spectra obtained in the presence of DiSC2(5) dye, 10 minutes before recording the CD spectra, a dye solution prepared in pH 7.00 10 mM NaPi buffer and 10% methanol was added to the PNA solutions such that the final dye concentration was 5 μ M.

II.6 References

1. Tanaka, K.; Shionoya, M., Programmable metal assembly on bio-inspired templates. *Coord. Chem. Rev.*, **2007**, 251 (21), 2732-2742.
2. Takezawa, Y.; Shionoya, M., Metal-mediated DNA base pairing: alternatives to hydrogen-bonded Watson–Crick base pairs. *Acc. Chem. Res.*, **2012**, 45 (12), 2066-2076.

3. He, W.; Franzini, R. M.; Achim, C., Metal-Containing Nucleic Acid Structures Based on Synergetic Hydrogen and Coordination Bonding. *Prog. Inorg. Chem.*, **2007**, *55*, 545-612.
4. De, A.; Kong, J.; Achim, C., *Metal Complexes as Alternative Base Pairs or Triplets in Natural and Synthetic Nucleic Acid Structures*. 2013; p 333-377.
5. Popescu, D.-L.; Parolin, T. J.; Achim, C., Metal incorporation in modified PNA duplexes. *J. Am. Chem. Soc.*, **2003**, *125* (21), 6354-6355.
6. Franzini, R. M.; Watson, R. M.; Patra, G. K.; Breece, R. M.; Tierney, D. L.; Hendrich, M. P.; Achim, C., Metal binding to bipyridine-modified PNA. *Inorg. Chem.*, **2006**, *45* (24), 9798-9811.
7. Ma, Z.; Olechnowicz, F.; Skorik, Y. A.; Achim, C., Metal binding to ligand-containing peptide nucleic acids. *Inorg. Chem.*, **2011**, *50* (13), 6083-6092.
8. de Leon, A. R.; Olatunde, A. O.; Morrow, J. R.; Achim, C., Binding of EuIII to 1, 2-Hydroxypyridinone-Modified Peptide Nucleic Acids. *Inorg. Chem.*, **2012**, *51* (23), 12597-12599.
9. Bezer, S.; Rapireddy, S.; Skorik, Y. A.; Ly, D. H.; Achim, C., Coordination-driven inversion of handedness in ligand-modified PNA. *Inorg. Chem.*, **2011**, *50* (23), 11929-11937.
10. Watson, R. M.; Skorik, Y. A.; Patra, G. K.; Achim, C., Influence of metal coordination on the mismatch tolerance of ligand-modified PNA duplexes. *J. Am. Chem. Soc.*, **2005**, *127* (42), 14628-14639.
11. Tanaka, K.; Yamada, Y.; Shionoya, M., Formation of silver (I)-mediated DNA duplex and triplex through an alternative base pair of pyridine nucleobases. *J. Am. Chem. Soc.*, **2002**, *124* (30), 8802-8803.
12. Takezawa, Y.; Maeda, W.; Tanaka, K.; Shionoya, M., Discrete self-assembly of iron (III) ions inside triple-stranded artificial DNA. *Angew. Chem. Int. Ed.*, **2009**, *48* (6), 1081-1084.
13. Ihara, T.; Ishii, T.; Araki, N.; Wilson, A. W.; Jyo, A., Silver ion unusually stabilizes the structure of a parallel-motif DNA triplex. *J. Am. Chem. Soc.*, **2009**, *131* (11), 3826-3827.
14. Urata, S.; Miyahata, T.; Matsuura, H.; Kitamura, Y.; Ihara, T., Alteration of DNase activity by silver ion. *Chem. Lett.*, **2014**, *43* (7), 1020-1022.
15. Feng, L.; Huang, Z.; Ren, J.; Qu, X., Toward site-specific, homogeneous and highly stable fluorescent silver nanoclusters fabrication on triplex DNA scaffolds. *Nucleic Acids Res.*, **2012**, *40* (16), 122-122.
16. Xiao, Z.; Zhu, H.; Xin, A.; Li, Y.; Ling, L., Triplex DNA logic gate based upon switching on/off their structure by Ag⁺/cysteine. *Analyst*, **2015**, *140* (21), 7322-7326.
17. Zhu, D.; Zhu, J.; Zhu, Y.; Wang, L.; Jiang, W., Sensitive detection of transcription factors using an Ag⁺-stabilized self-assembly triplex DNA molecular switch. *Chem. Commun.*, **2014**, *50* (95), 14987-14990.
18. Moser, H. E.; Dervan, P. B., Sequence-specific cleavage of double helical DNA by triple helix formation. *Science*, **1987**, *238* (4827), 645-650.
19. Wittung, P.; Nielsen, P.; Norder, B., Observation of a PNA– PNA– PNA Triplex. *J. Am. Chem. Soc.*, **1997**, *119* (13), 3189-3190.
20. Shimada, H.; Sakurai, T.; Kitamura, Y.; Matsuura, H.; Ihara, T., Metallo-regulation of the bimolecular triplex formation of a peptide nucleic acid. *Dalton Trans.*, **2013**, *42* (45), 16006-16013.
21. Cabani, S.; Landucci, M., Stability constants of zinc (II)-and nickel (II)-2, 2'-bipyridyl complexes. *J. Chem. Soc.*, **1962**, 278-282.

22. Baxendale, J.; George, P., Equilibria in solutions of ferrous ions and $\alpha\alpha'$ -dipyridyl. *J. Chem. Soc. Faraday Trans.*, **1950**, 46, 55-63.
23. Fresco, J.; Freiser, H., Solubilities of Certain Divalent Metal Complexes of 8-Quinolinol and Substituted 8-Quinolinols in Aqueous Media. *Anal. Chem.*, **1964**, 36 (2), 372-375.
24. Irving, H.; Mellor, D., 1002. The stability of metal complexes of 1, 10-phenanthroline and its analogues. Part I. 1, 10-Phenanthroline and 2, 2'-bipyridyl. *J. Chem. Soc.*, **1962**, 5222-5237.
25. Albert, A.; Gibson, M.; Rubbo, S., The influence of chemical constitution on anti-bacterial activity. Part VI: the bactericidal action of 8-hydroxyquinoline (oxine). *Br J Exp Pathol.*, **1953**, 34 (2), 119.
26. Sone, K.; Krumholz, P.; Stammreich, H., Studies on the Coördinate Bond. III. Absorption Spectra of Mono- α , α'' -dipyridyl and Mono-o-phenanthroline Complexes I. *J. Am. Chem. Soc.*, **1955**, 77 (3), 777-780.
27. Jørgensen, C., Spectroscopy of Transition-Group Complexes. *Adv. Chem. Phys.*, **1963**, 33-146.
28. Phillips, J.; Huber, W.; Chung, J.; Merritt Jr, L., Ultraviolet Absorption Spectra of 2-Substituted 8-Quinolinols. *J. Am. Chem. Soc.*, **1951**, 73 (2), 630-632.
29. Sone, K., Absorption Spectra of Some Metallic Chelate Compounds. *J. Am. Chem. Soc.*, **1953**, 75 (21), 5207-5211.
30. Amundsen, A. R.; Whelan, J.; Bosnich, B., Biological analogs. Nature of the binding sites of copper-containing proteins. *J. Am. Chem. Soc.*, **1977**, 99 (20), 6730-6739.
31. Gans, P.; Sabatini, A.; Vacca, A., Investigation of equilibria in solution. Determination of equilibrium constants with the HYPERQUAD suite of programs. *Talanta*, **1996**, 43 (10), 1739-1753.
32. Alderighi, L.; Gans, P.; Ienco, A.; Peters, D.; Sabatini, A.; Vacca, A., Hyperquad simulation and speciation (HySS): a utility program for the investigation of equilibria involving soluble and partially soluble species. *Coord. Chem. Rev.*, **1999**, 184 (1), 311-318.
33. Wittung, P.; Eriksson, M.; Lyng, R.; Nielsen, P. E.; Norden, B., Induced chirality in PNA-PNA duplexes. *J. Am. Chem. Soc.*, **1995**, 117 (41), 10167-10173.
34. Smith, J. O.; Olson, D. A.; Armitage, B. A., Molecular recognition of PNA-containing hybrids: spontaneous assembly of helical cyanine dye aggregates on PNA templates. *J. Am. Chem. Soc.*, **1999**, 121 (12), 2686-2695.
35. Seifert, J. L.; Connor, R. E.; Kushon, S. A.; Wang, M.; Armitage, B. A., Spontaneous assembly of helical cyanine dye aggregates on DNA nanotemplates. *J. Am. Chem. Soc.*, **1999**, 121 (13), 2987-2995.
36. Yeh, J. I.; Pohl, E.; Truan, D.; He, W.; Sheldrick, G. M.; Du, S.; Achim, C., The Crystal Structure of Non-Modified and Bipyridine-Modified PNA Duplexes. *Chem. Eur. J.*, **2010**, 16 (39), 11867-11875.
37. Duprey, J. L. H.; Takezawa, Y.; Shionoya, M., Metal-locked DNA three-way junction. *Angew. Chem.*, **2013**, 125 (4), 1250-1254.
38. McCaffery, A. J.; Mason, S. F.; Norman, B. J., Optical rotatory power of co-ordination compounds. Part XII. Spectroscopic and configurational assignments for the tris-bipyridyl and -phenanthroline complexes of the di- and tri-valent iron-group metal ions. *J. Chem. Soc.*, **1969**, 1428-1441.
39. Mason, S. F.; Norman, B. J., Optical rotatory power of co-ordination compounds. Part XIII. Circular dichroism of hetero-trischelated metal complexes of bipyridyl and phenanthroline. *J. Chem. Soc.*, **1969**, 1442-1447.

40. Mason, S. F.; Peart, B. J.; Waddell, R. E., Optical rotatory power of co-ordination compounds. Part XVI. Intermediate exciton coupling in the circular dichroism of trisbipyridyl complexes. *Dalton Trans.*, **1973**, (9), 944-949.
41. Harding, M. J.; Mason, S. F.; Peart, B. J., Optical rotatory power of co-ordination compounds. Part XVIII. The circular dichroism of trigonal nickel(II) chelate complexes. *Dalton Trans.*, **1973**, (9), 955-960.
42. Christensen, L.; Fitzpatrick, R.; Gildea, B.; Petersen, K. H.; Hansen, H. F.; Koch, T.; Egholm, M.; Buchardt, O.; Nielsen, P. E.; Coull, J., Solid-phase synthesis of peptide nucleic acids. *J. Pept. Sci.*, **1995**, 1 (3), 175-183.
43. Ducholm, K. L.; Egholm, M.; Behrens, C.; Christensen, L.; Hansen, H. F.; Vulpius, T.; Petersen, K. H.; Berg, R. H.; Nielsen, P. E.; Buchardt, O., Synthesis of peptide nucleic acid monomers containing the four natural nucleobases: thymine, cytosine, adenine, and guanine and their oligomerization. *J. Org. Chem.*, **1994**, 59 (19), 5767-5773.
44. Golombek, A. P.; Hendrich, M. P., Quantitative analysis of dinuclear manganese (II) EPR spectra. *J. Magn. Reson.*, **2003**, 165 (1), 33-48.

CHAPTER III: Peptide Nucleic Assisted Dimerization of Gold Nanoclusters

The Scanning transmission electron microscopy (STEM) imaging and analysis presented in this chapter was done by Stephen House from Professor Judith C. Yang's group from University of Pittsburgh.

III.1 Introduction

Hybrid gold nanoparticle(AuNP)-DNA systems have been synthesized for applications in sensing, imaging, catalysis, therapeutics, diagnostics, and drug delivery.¹⁻³ Particularly, AuNP dimers have attracted attention due to their significant plasmonic coupling enhancement upon dimerization. A relatively straightforward method for the construction of AuNP dimers is the synthesis of mono-DNA-functionalized gold nanoparticles and to use the Watson crick base pairing of complimentary DNA strands to bring two AuNP together.⁴⁻⁸ AuNP conjugates bearing a discrete number of oligonucleotide per particle are also useful in bio-diagnostics and as building blocks to construct nanostructures.

To date, there are numerous studies on the preparation and applications of DNA-AuNP conjugates.^{4-5, 9-13} The majority of the papers published on DNA conjugation to AuNP reported the attachment of ss-DNA bearing free thiol or disulfide groups to aqueous gold colloids, including nanoparticles of typically 5-250 nm. There are two established protocol to attach thiol-modified ss-DNA to AuNPs depending on the final coverage of oligonucleotides on the NP, one that produces NPs functionalized with one or a few of oligos, and one that produces NPs functionalized with a dense layer of many oligos.¹⁴ The oligonucleotide-modified NPs are typically separated from side products and unreacted materials by centrifugation or gel-electrophoresis.

In contrast to the studies of DNA-AuNPs conjugates being numerous, only a few reports focused on the modification of AuNPs with synthetic nucleic acid such as peptide nucleic acid (PNA),¹⁵⁻¹⁷ locked nucleic acid (LNA),¹⁸⁻¹⁹ and morpholino oligomers.²⁰⁻²¹ The specific properties of these synthetic molecules are different from those of DNA; hence one can anticipate that their conjugates with AuNPs would also be different from those of DNA-AuNP conjugates and that these differences can be exploited in distinct applications. For example, PNA has a higher affinity for DNA than DNA itself and, consequently, one could anticipate that PNA-AuNP conjugates display superior selectivity in binding to specific positions on DNA nanostructures. To the best of our knowledge, only three papers reported the direct conjugation of PNAs onto AuNPs through Au-thiol bonds.^{15, 22-23} The conjugation reactions have been carried out in sodium phosphate buffer^{15, 24} or pure water.²²

The charge neutrality of PNA can lead to strong, non-specific interactions between PNA and AuNPs, which may underscore the immediate agglomeration and precipitation observed when thiolated PNA is mixed with citrate stabilized AuNPs.^{15, 22} This challenge in the synthesis of stable PNA-AuNPs was addressed by including charged amino acids and hydrophilic linkers to PNA oligomers that vary the charge density and the hydrophobicity of the PNA sequences.¹⁵ This strategy led to conjugates of citrate-stabilized AuNPs with diameter of ~13 nm with modified PNAs that were stable for short time periods. Murphy and co-workers used PNA-DNA chimeras, which carry a negative charge, to improve the solubility of PNA-Au NP conjugates.¹⁷

Surfactants have also been used to improve the solubility of PNA-Au NP conjugates. Duy *et al.* used non-ionic surfactant polyoxyethylene (20) sorbitan monolaurate (Tween 20) to mediate the exchange between citrate anions situated on the surface of Au NPs and thiolated PNA. More recently, Tween 20 and 32-mercapto-

3,6,9,12,15,18,21-hepta-oxadotriacontan-1-oic acid have been used to synthesize highly stable PNA-AuNP conjugates.²³ Anstaett *et al.* argued that non-selective aggregation of PNA-Au-NPs still occurs during the synthesis of PNA-Au NPs in the presence of Tween 20.

The three studies of PNA AuNPs published to date presented evidence that PNAs can be bound to AuNPs and that the bound PNAs are accessible to complementary oligonucleotides. They have not showed a method to synthesize AuNP-PNA conjugates with a specific number of PNA strands per AuNP. One part of our work fills this gap by introducing a method to synthesize and isolate gold-nanocluster (AuNC) conjugates bearing a known number of PNA strands per AuNC. Alivisatos published a couple of papers on the kinetic control of attachment of a few DNA oligonucleotides onto AuNPs and the separation of the DNA-Au NPs by gel electrophoresis based on the number of DNAs per NP.^{6, 25-27} A fairly long oligonucleotide (>50 nucleotides) was necessary to purify the ss-DNA-AuNP conjugates by gel electrophoresis because shorter ss-DNA are “intrinsically bent” and wrap around AuNPs.²⁸⁻³⁰

AuNCs are special types of nanoparticles that have a countable number of atoms (up to ~200), small core diameters (less than ~2 nm), and a precise molecular structure (Figure III.1a).³¹⁻³² Given their size, AuNCs behave as clusters of atoms or molecules and quantum confinement effects are manifest in their properties. AuNCs can manifest HOMO-LUMO electronic transitions (Figure III.1 b and c), enhanced photoluminescence, chirality, and intrinsic magnetism. These properties are different from those of the bulk metal and of conventional nanoparticles (2-100 nm in size). Additionally, AuNCs have a higher biocompatibility than AuNPs.

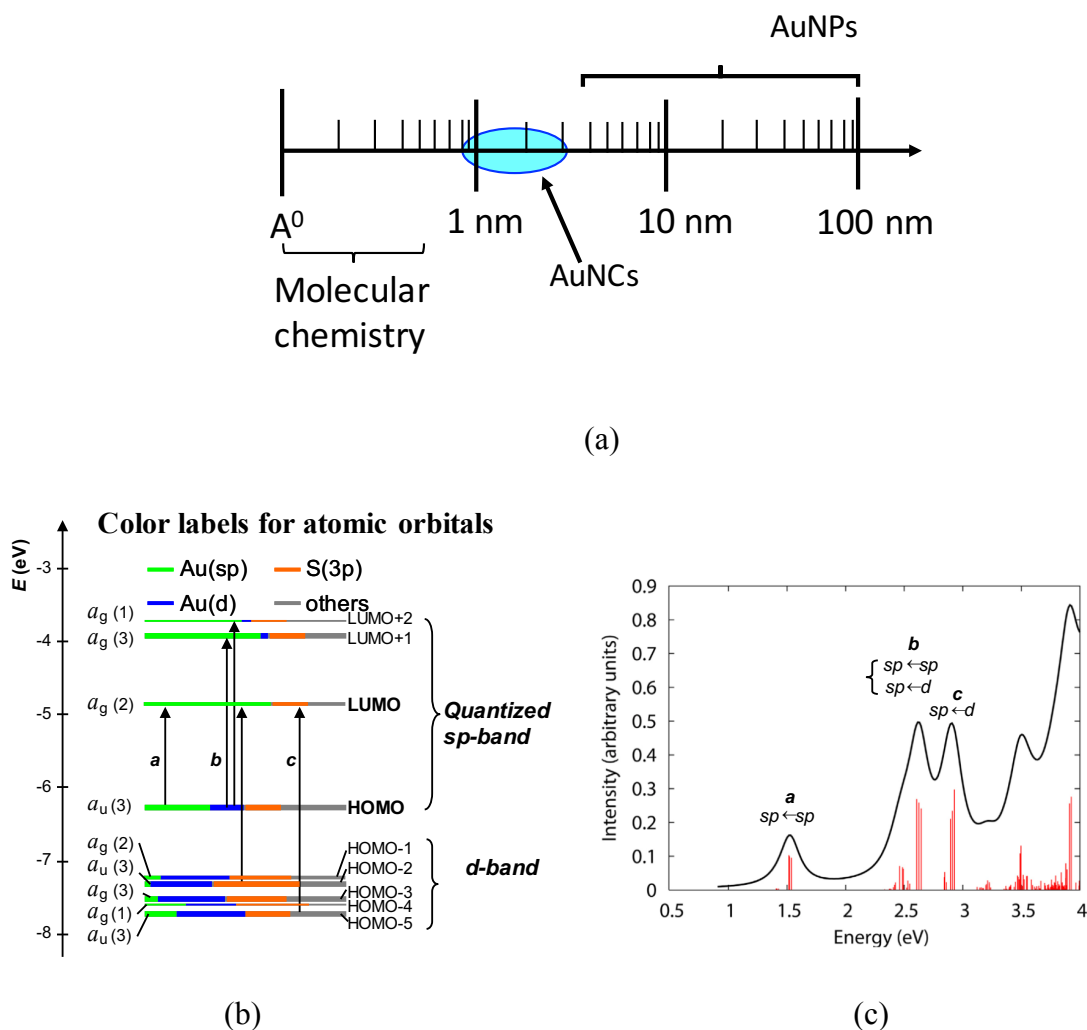


Figure III.1: (a) Size regime to show where AuNC lie compared to the dimensions of molecules and AuNPs. (b) Kohn-Sham orbital energy level diagram to show the electronic transitions in a model $[Au_{25}(SH)_{18}]^-$ cluster. (c) Simulated optical absorption spectrum for $[Au_{25}(SH)_{18}]^-$ clusters. “Reprinted (adapted) with permission from the reference³³. Copyright (2008) American Chemical Society.”

Ackerson *et al.* published a paper in 2005 on the successful conjugation of 19- or 20-residue thiolated ss-DNA onto glutathione monolayer protected clusters with ~ 1.2 nm core diameter.³⁴ They were able to successfully separate the conjugates by gel electrophoresis, based on the number of bound ss-DNAs per particle. The glutathione monolayer suppressed the direct DNA-gold interactions, which is believed to interfere not only with electrophoretic separation but also with the hybridization of the complementary strands when the DNA sequence length is < 50 nucleotides.

In the work presented in this chapter we used $[\text{Au}_{25}(\text{Captopril})_{18}]^-$ to create PNA-AuNC conjugates. Au_{25} clusters typically have diameters of about 1 nm. The ultra-small size of the AuNCs and the potential PNA-induced aggregation of AuNPs were the main challenges in the development of a suitable conjugation protocol, a purification methodology, and the characterization of PNA-AuNC conjugates. PNA oligomers modified with a monothiol (L-Cys, SH1) or a trithiol group (3-mercaptopropionic acid, SH3) were used to modify AuNCs. The properties of PNA-AuNC conjugates were studied by UV-Vis melting, CD spectroscopy and Fluorescence spectroscopy. The PNA-AuNC conjugates that had one PNA/AuNC were used to prepare dimers of AuNCs by PNA hybridization of complementary PNAs attached to different AuNCs. STEM analysis was used to prove the AuNC dimerization, assisted by complementary PNA hybridization. AuNP dimers of particle diameters of 5-36 nm, linked by DNA duplexes that had 11-100 base pairs have been synthesized.⁶ ⁸ These procedures involved tedious, multistep purifications and the yield of dimer formation was up to 26%.⁷ Our method successfully makes AuNC dimers connected by 8 or 10-base pair PNA duplexes in a few synthetic steps with a yield of up to 45-50%.

III.2 Research Design

We hypothesize that PNA can be particularly useful in the assembly of functional groups in larger nanostructures. We chose to synthesize dimers of Au nanoclusters bridged by PNA duplexes as a goal for the research presented in this paper. In this pursuit, we evaluated two steps critical for the realization of PNA's potential as smart glue for nano-scale structures with inorganic components, namely:

(1) the synthesis and purification of gold nanoclusters bearing a discrete and known number of single stranded PNAs and

(2) the ability of complementary PNA strands that carry relatively large inorganic groups to hybridize based on Watson Crick base pairing.

We used $[\text{Au}_{25}(\text{Capt})_{18}]^-$ clusters³⁵ as the inorganic component and 8- or 10-base pair duplexes as a glue. The $[\text{Au}_{25}(\text{Capt})_{18}]^-$ clusters were chosen because they are (1) soluble in water, a solvent in which PNA is also soluble, and (2) stable at temperatures up to 80°C, which is above the melting temperature is shown in Figure III.7 and Table III.3. The 10-bp PNA1.PNA2 duplex has been used in a very large number of published studies, and is thus extremely well-characterized. The 8-bp PNA3.PNA3 duplex had a palindromic sequence. A stretch of three L-Glu amino acids was introduced at the C-end of each PNA strand because at neutral pH it would confer a negative charge to the PNA, and thus reduce the chance that the PNA strands lie down on the negatively-charged nanoclusters to which they are attached. A monothiol (L-Cys, SH1) or a trithiol group (3-mercapto-2,2-bis(mercaptomethyl)propanoic acid, SH3) was introduced at the N-end of each PNA strand to support the formation Au-S bonds between the PNA and the nanoclusters. PNA sequences and MALDI data are given in Table III.1.

Table III.1: PNA sequences and MALDI data

Abbreviation	Sequence (N to C)	MWcalc/exp
PNA 1	H-GTAGATCACT-(L-Glu) ₃ -NH ₂	3113.9/3114.66
PNA 2	H-AGTGATCTAC-(L-Glu) ₃ -NH ₂	3113.9/3115.66
PNA 3	H-CCTTAAGG-(L-Glu) ₃ -NH ₂	2572.47/2571.12
PNA 1-SH3	(HS-CH ₂) ₃ -C-CO-GTAGATCACT-(L-Glu) ₃ -NH ₂	3294.34/3295.99
PNA 2-SH3	(HS-CH ₂) ₃ -C-CO-AGTGATCTAC-(L-Glu) ₃ -NH ₂	3294.34/3295.07
PNA 1-SH1	H-L-Cys- GTAGATCACT-(L-Glu) ₃ -NH ₂	3259.03/3258.28
PNA 2-SH1	H-L-Cys- AGTGATCTAC -(L-Glu) ₃ -NH ₂	3259.03/3259.72
PNA 3-SH3	(HS-CH ₂) ₃ -C-CO-CCTTAAGG-(L-Glu) ₃ -NH ₂	2752.79/2776.57

We anticipated that we will be able to use gel electrophoresis to separate these conjugates because they and the $[\text{Au}_{25}(\text{Capt})_{18}]^-$ clusters are charged (Figure III.12). Therefore, one can expect to get discrete bands in gels based on the number of bound PNAs per cluster.

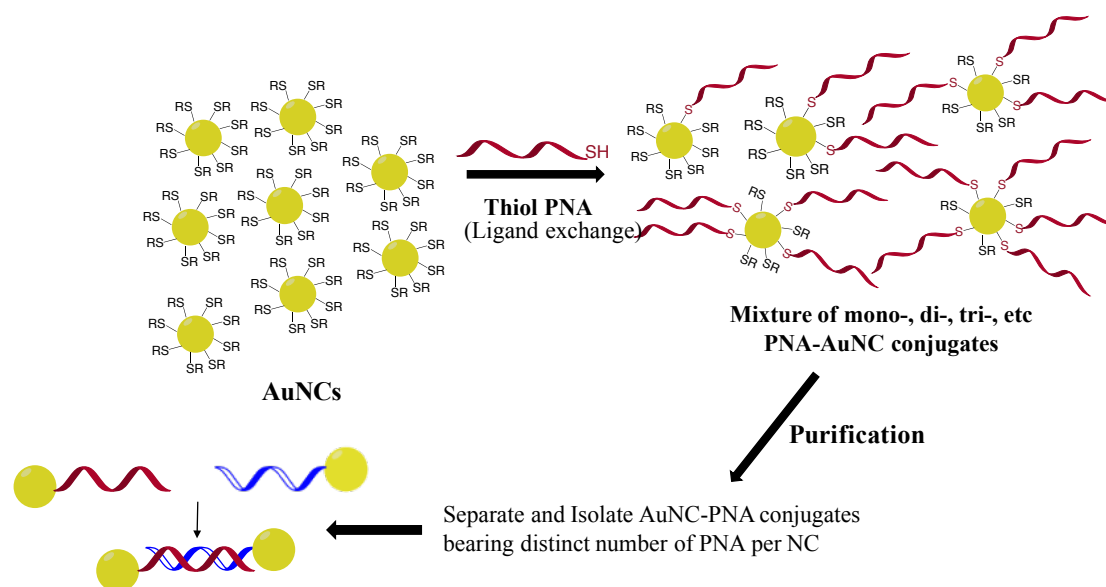


Figure III.2: Schematic representation of the research design

III.3 Results and Discussion

III.3.1 Purification, Isolation and Quantification of PNA-AuNC conjugates bearing a finite number of PNA strands per cluster

One of our main goals for this paper is to establish a protocol to synthesize and isolate individual conjugates bearing a finite number of PNA per Au_{25} cluster, i.e: 1xPNA - Au_{25} , 2xPNA - Au_{25} , 3xPNA - Au_{25} etc. We carried out a series of Au_{25} -PNA conjugation reaction at different PNA1 SH3: Au_{25} ratios of 0.2 to 2.4 and studied the product mixtures by gel electrophoresis (Figure III.3). Lane 10 in Figure III.3 shows the electrophoretic behavior of AuNC only; lane 6 in Figure III.3 shows the PNA only. The intense low mobility band (top band) observed for all reaction mixtures that contain

both PNA and AuNCs is attributed to Au₂₅-PNA aggregates. Its intensity increases when the PNA1-SH3: Au₂₅ ratio in the reaction mixtures increases. We attribute the other, intermediate mobility bands to Au₂₅-PNA conjugates with discrete numbers of ss-PNAs/cluster. The highest number of distinct gel bands (up to 4-PNAs per Au₂₅) with the best resolution is seen for a PNA: Au₂₅ molar ratio of 0.4 (Figure III.3 lane 2). The same experiment was done with mono-thiol modified PNA1-SH1 (Figure III.4) While PNA1-SH3 gives rise to distinct gel bands at ratios as high as 2.4, PNA1-SH1 induced full aggregation of Au₂₅ at ratios as low as 0.5. The molar ratio that gives rise to the highest number of well-resolved distinct gel bands for PNA1-SH1 – Au₂₅ conjugates is 0.10. At this ratio, two distinct gel bands for specific PNA1-SH1 – Au₂₅ conjugates and almost no unreacted PNAs or PNA-Au₂₅ aggregates are observed. Thus, one can choose to carry out their PNA-AuNC conjugation reactions starting with either mono- or tri-thiol PNAs based on the final goal of the experiment.

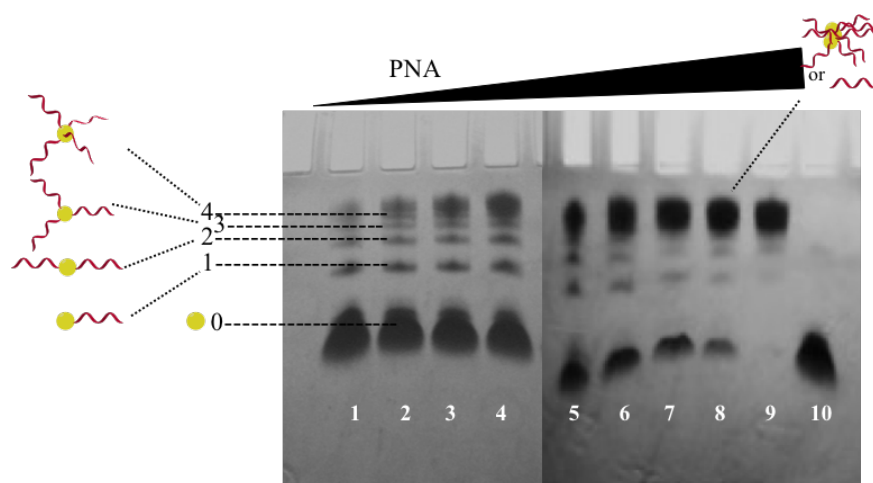


Figure III.3: The gel migration pattern for reaction products obtained from the incubation of Au NCs with PNA1-SH3 for 1 hour at 50°C. The PNA1-SH3:AuNC ratios were 0.2, 0.4, 0.5, 0.7, 0.9, 1.3, 1.7, 2.1 and 2.4 (left to right, lanes 1-9) and AuNC only (lane 10)

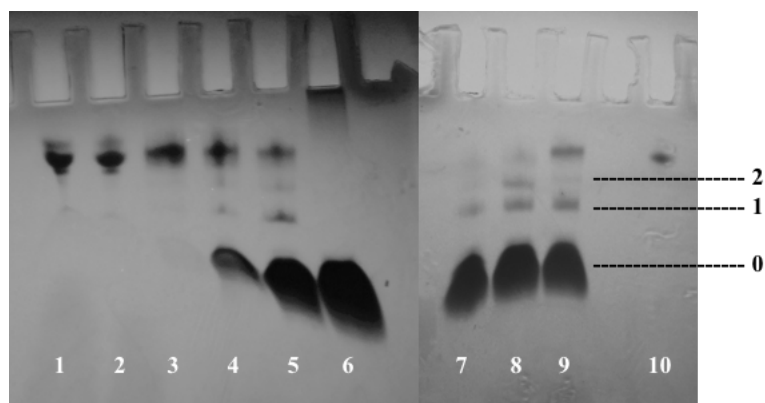


Figure III.4: The gel migration pattern for reaction products obtained from the incubation of Au NCs with PNA1-SH1 for 1 hour at 50°C. Lanes 1-5 and 7-9, PNA1-SH1: Au₂₅ ratios 0.90, 0.70, 0.50, 0.40, 0.20, 0.05, 0.10, 0.15. Lane 6: AuNC only and Lane 10: PNA 1-SH1 only.

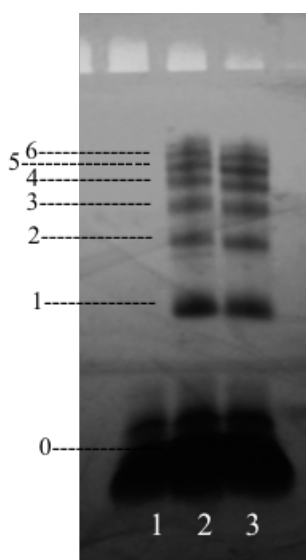


Figure III.5: The gel migration pattern for scaled up reactions between PNA1-SH3 or PNA2-SH3 and Au₂₅ at PNA : Au₂₅ molar ratio 0.4. Up to six distinct gel bands are seen that correspond to conjugates bearing distinct number of PNAs per Au₂₅ cluster. Lane 1: Au₂₅ only, lane 2: PNA2-SH3: Au₂₅ reaction mixture and lane 3: PNA1-SH3: Au₂₅ reaction mixture.

Since the beginning of the use of gel-electrophoresis to purify DNA-AuNP conjugates, each discrete gel band was assigned to a conjugate bearing a unique number of DNA strands per particle.^{6, 25} Ancona and co-workers used a simple UV-Vis absorption spectroscopy based method to verify the ratio between DNA and AuEO3

(EO3: methyl-terminated tri(oxyethylene) thiol, $\text{CH}_3(\text{OCH}_2\text{CH}_2)_3\text{SH}$) for mono-DNA-AuEO3 conjugate extracted from gel-electrophoretic purification.³⁶ They incubated 5'-HS-(CH_2)₆-ACACACACACACACA-fluorescein-3' with AuEO3 AuNC with a diameter of about 1.8 ± 0.2 nm at DNA : AuNC molar ratio of 0.09 for 16 hours at 35 °C. The resultant product was purified by 2% agarose gel electrophoresis. The mono-DNA-AuEO3 conjugate was extracted from the cut gel band pieces following an organic-aqueous extraction method. UV-Vis absorption spectrum was recorded for the extracted DNA-AuEO3 conjugate. Since the ϵ_{260} nm for EO3SH is known, absorbance at 260 nm due to conjugated DNA could be corrected for the contribution by EO3SH at 260 nm. Number of moles of DNA in the conjugate was calculated from the corrected absorbance data. Absorbance at 507 nm was used to determine the number of moles of AuEO3. Finally, the number of DNA strands per cluster was calculated to be 0.82 ± 0.13 .

We wanted to quantitatively identify the nature of the PNA-Au₂₅ conjugates in each discrete gel band observed for reaction mixtures of Au₂₅ with PNAs. We used a procedure similar to that used by Ancona and co-workers to determine the ratio between PNA and Au₂₅ in each gel band. Figure III.6 shows the absorption spectra for PNA1-SH3 Au₂₅ conjugates and Table III.2 gives the average number of PNA1-SH3 : Au₂₅ for conjugates extracted from the gel bands numbered 1-3 in Figure III.5 lane 2. The three bands contain 1 PNA1/cluster, 2 PNA1/cluster and 3 PNA1/cluster respectively.

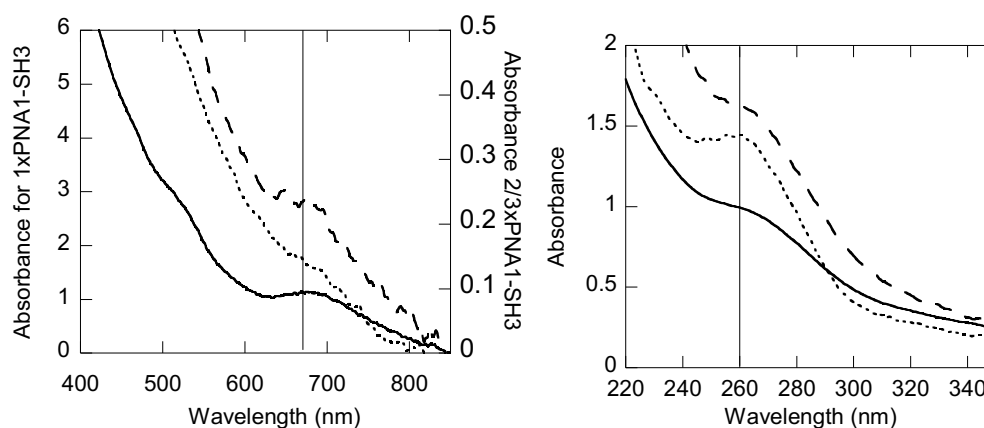





Figure III.6: Absorption spectra for 1x (solid line) PNA1-SH3 – Au₂₅ conjugate, 2x (dashed line) PNA1-SH3 - Au₂₅ conjugate or 3x (dotted line) PNA1-SH3 – Au₂₅ conjugates in the wavelength ranges (a) 400 – 850 nm, and (b) 220 – 350 nm. 670 nm and 260 nm are identified by vertical lines. Each extracted conjugate was diluted with water to get reasonable absorbance at 670 nm (Au₂₅ absorption) and 260 nm (PNA absorption).

Table III.2: Average PNA1-SH3 : Au₂₅ ratio in the conjugates from gel electrophoresis bands 1-3

Gel bands	Conjugate	PNA : Au ₂₅ ratio
 ----- 3	3xPNA-Au ₂₅	3.53±0.55
 ----- 2	2xPNA-Au ₂₅	2.35±0.22
 ----- 1	1xPNA-Au ₂₅	1.12±0.18

III.3.2 Melting behavior of PNA-AuNC conjugates

The PNA1.PNA2 duplex has a melting temperature T_m of 68°C in nanopure water and in 10 mM pH 7.00 NaPi buffer (Figure III.7(a) and Table III.3). The melting temperature is not affected by the introduction of three L-Glu residues at the C-end of the strands. This finding is in agreement with previous results that showed similar T_m for the duplex with a C-terminal single D/L-Lysine, L-Glutamic acid, L-Alanine, L-Phenylalanine or L-Isoleucine.³⁷⁻³⁸ The PNA3.PNA3 duplex has a melting temperature

of 58°C, which is lower than that of the PNA1.PNA2 duplex. The fact that the two duplexes, which have similar GC content, have different T_m can be related to the differences in their lengths. The melting temperatures for the PNA1.PNA2 duplex decreased by 10 °C when Au₂₅ nanoclusters have been attached to the PNA strands (Figure III.7(a) and Table III.3).

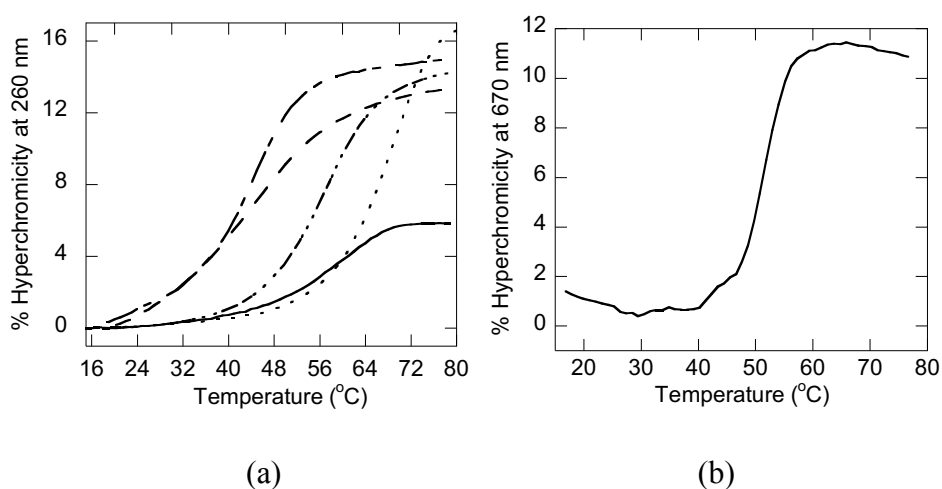


Figure III.7: Melting curves (a) monitored at 260 nm for ss PNA 1 (10 μ M, dotted-dashed line), ss PNA 2 (10 μ M, dashed line), PNA 1 – PNA 2 duplex (5 μ M, dotted line), PNA 3 duplex (10 μ M, double dotted-double dashed line), PNA 1-SH3 – PNA 2-SH3 Au₂₅ assembly (4 μ M in duplex concentration, solid line) or (b) monitored at 670 nm for same PNA 1-SH3 – PNA 2-SH3 Au₂₅ assembly. All samples were in 10 mM, pH 7.00 sodium phosphate buffer.

We attribute this decrease to the fact that the Au₂₅ clusters can negatively affect the π -stacking of the terminal base pairs. This explanation is supported by the fact that the hyperchromicity change induced by duplex melting is ~10% smaller when Au₂₅ NCs are attached to the strands. We have also observed a sharp sigmoidal increase in the absorbance at 670 nm, where AuNCs absorbs, as the temperature of a solution containing PNA1-SH3 and PNA2-SH3 attached to AuNCs solution was heated to 52°C (Figure III.7(b)), which indicates a cooperative melting of the duplexes.

We note that in this experiment, we used conjugates of Au₂₅ NCs with PNA1 and with PNA2 that have not been purified based on the number of PNA strands per cluster. Hence the samples contain a mixture of Au₂₅ clusters with different number of attached PNA strands. Hence the cooperative melting can occur from multiple equivalent melting sites in the PNA-AuNP structures in which each pair of AuNPs may be linked by multiple PNA linkers, as previously noted for DNA-AuNP structures.³⁹

Table III.3: Melting temperatures (T_m)^a for single stranded (ss) PNAs or PNA duplexes with no thiol modifications and for Au₂₅-PNA assemblies.

PNA assembly	T_m (°C) ^b	
	260 nm	670 nm
ss PNA 1	44	-
ss PNA 2	45	-
PNA 1 - PNA 2 duplex	68	-
PNA 3 duplex	59	-
PNA 1-SH3 - PNA 2-SH3 Au ₂₅ assembly	58	52

^a T_m were determined by the first derivative plot of the melting curves and are known within 1°C; ^b Changes in absorbance with temperature were monitored at both 260 nm, where nucleobases absorb and at 670 nm, where the Au₂₅ clusters absorb.

III.3.3 Chiral Properties of PNA-AuNC conjugates

The PNA1.PNA2 duplex adopts a helical structure at pH 7.00. A preferred handedness can be induced in the duplex by a terminal, chiral amino acid.³⁸ Figure III.8 shows the CD spectra for PNA1.PNA2 duplex, [Au₂₅(Capt)₁₈]⁻ clusters, Captopril ligand, PNA1-SH3 - Au₂₅ conjugate, PNA2-SH3 - Au₂₅ conjugate and PNA1-SH3.PNA2-SH3 Au₂₅ assembly.

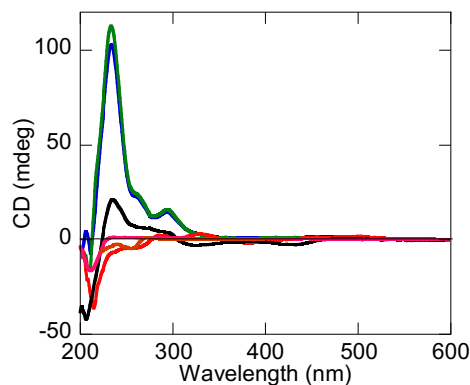


Figure III.8: CD spectra for PNA1.PNA2 duplex (10 μ M, orange), $[\text{Au}_{25}(\text{Capt})_{18}]^-$ clusters (8 μ M, black), Captopril ligand (60 μ M, pink), PNA1-SH3 - Au_{25} conjugate (4 μ M PNA1-SH3, blue) , PNA2-SH3 - Au_{25} conjugate (4 μ M PNA2-SH3, green) or PNA1-SH3-PNA2-SH3 Au_{25} assembly (2 μ M PNA1-SH3-PNA2-SH3 duplex, red) in 10 mM pH 7.00 sodium phosphate buffer. UV-Vis spectra for these samples are given in Figure III.19.

PNA1-SH3- or PNA2-SH3- Au_{25} conjugates have identical CD spectra that are significantly different from the CD spectra for $[\text{Au}_{25}(\text{Capt})_{18}]^-$. The CD spectrum for $[\text{Au}_{25}(\text{Capt})_{18}]^-$ clusters shows two positive peaks 275 nm, 480 nm and two negative peaks ~ 310 nm and 430 nm, which is in agreement with previously published results.³⁵ These CD features correspond to metal-based electronic transitions that manifest in the CD due to the chiral induction effect exerted by chiral captopril ligands on the metal core. We observed another positive peak at 235 nm and a negative peak at 208 nm. The peak at 208 nm is attributed to the chiral captopril ligands.⁴⁰ The substitution of captopril ligand/s by PNA1-SH3 or PNA2-SH3 significantly enhances the intensity of the positive peak at 235 nm for $[\text{Au}_{25}(\text{Capt})_{18}]^-$. New CD positive features are observed at 260 nm, 295 nm and ~ 460 nm for Au_{25} conjugates with single stranded PNA1-SH3 and PNA2-SH3. The positive peaks observed for $[\text{Au}_{25}(\text{Capt})_{18}]^-$ clusters at 275 nm, at 580 nm and negative peaks at 325 nm and 430 nm disappear.

A sample prepared by annealing 1:1 mixture of PNA1-SH3- Au_{25} conjugate and PNA2-SH3- Au_{25} , which we call as PNA1-SH3-PNA2-SH3 Au_{25} assembly, shows CD

features different from those of spectra for $[\text{Au}_{25}(\text{Capt})_{18}]^-$ clusters and for Au_{25} conjugates with single stranded PNAs. Note that the PNA1/2 SH3- Au_{25} conjugates used to prepare these samples were not separated based on the number of PNA strands/cluster. Therefore, the PNA1-SH3-PNA2-SH3 Au_{25} sample is likely to contain a mixture of dimers, trimers, tetramers or even extended networks duplexes that form during the annealing process between Au_{25} conjugates with a variable number of PNAs. Specifically, a negative peak is observed at 260 nm and a small positive peak is observed at 270 nm; these features are due to $\pi - \pi^*$ transitions of the nucleobases and are indicative of a left-handed PNA duplex.³⁸ The fact that the strong positive peak seen at 235 nm in both PNA1-SH3/ PNA2-SH3 Au_{25} conjugates disappears and that a negative peak appears at 260 nm in PNA1-SH3-PNA2-SH3 Au_{25} assembly clearly indicates that the Au_{25} clusters are brought together into dimers bridged by PNA1-PNA2 duplexes. The peak intensity for the negative 260 nm feature observed for the non-modified PNA duplex and the Au_{25} -modified duplex is the same although the duplex concentration in the two samples is different, namely 10 μM and 2 μM , respectively. This suggests that the Au_{25} nanoclusters amplify the CD peak due to nucleobase absorption of the duplexes to which they are linked. Two positive peaks at 288 nm, 330 nm, a broad peak centered ~ 500 nm and a negative peak at 380 nm are also observed in the spectrum of the PNA1-SH3-PNA2-SH3 Au_{25} assembly. The CD features of $[\text{Au}_{25}(\text{Capt})_{18}]^-$ clusters continue to change from ss-PNA modification to complementary PNA assisted assembly formation of Au_{25} clusters. These observations show that the chirality of Au_{25} clusters are very sensitive to fine changes in the nature of the surface ligands.⁴¹

III.3.4 STEM analysis of AuNC dimerization

Scanning transmission electron microscopy (STEM) was employed to confirm the AuNC size as well as to determine the degree of pair self-assembly in each sample. Example images of the PNA-functionalized AuNCs are shown in Figure III.9 along with their size histograms. The particle size distributions were slightly lognormal (right skew), with means and standard deviations of 1.04 ± 0.12 nm and 1.07 ± 0.10 nm for the annealed PNA1-SH3+PNA2-SH3 and annealed PNA3-SH3 specimens, respectively. The corresponding lognormal quantile plots are included in Figure III.21.

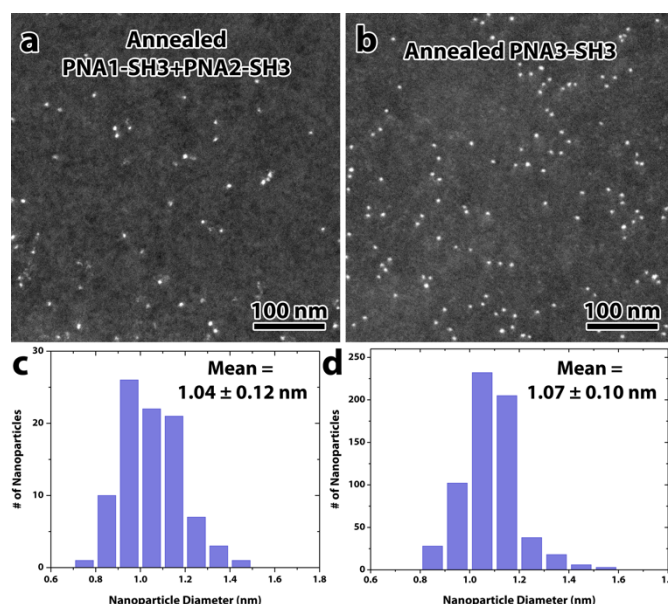


Figure III.9: Example HAADF-STEM micrographs (a,b) and corresponding particle size histograms (c,d) from the annealed PNA1-SH3+PNA2-SH3 (a,c) and annealed PNA3-SH3 (b,d) specimens.

The presence and degree of self-assembly of the PNA-functionalized AuNCs was characterized by examining the nearest neighbor (nn) distances. Because each AuNC should only have a single PNA attached to it, self-assembly into AuNC would be expected. The pairing up on AuNCs in this manner should most strongly a deviation in the first nn distances. Deviations in higher-order nn distances as

the radial distribution function would also occur but not manifest as clear a
Only images from regions of the specimens without the presence of additional
that would impact the spatial distribution were selected for analysis. Examples of
factors include edges of the lacy carbon “holes,” “coffee ring”-like drying artifacts,
support imperfections. Roughly ten images were analyzed for each specimen, with
populations of ~1000-18000 particles measured (Table III.6). A typical image from
each of these datasets is included in

Figure III.10 (a)-(e).

In conventional nn analysis, the “random” distribution used for comparison is typically assumed to be of a given form, such as a Poisson. This, is not an ideal approach, however, as it does not take into account the impact that differences in images’ spatial densities of AuNCs and the finite dimensions of the micrograph have on the resulting distribution. For this study, a program was composed that takes into account these aspects to produce more accurate “random” distributions that are tailored to reflect the details of each experimental dataset. This same program was also used to perform the analysis herein applied to both the experimental and simulated datasets. These distributions thus more accurately represent what would be expected if the AuNCs were truly randomly distributed, providing a more robust and meaningful comparison.

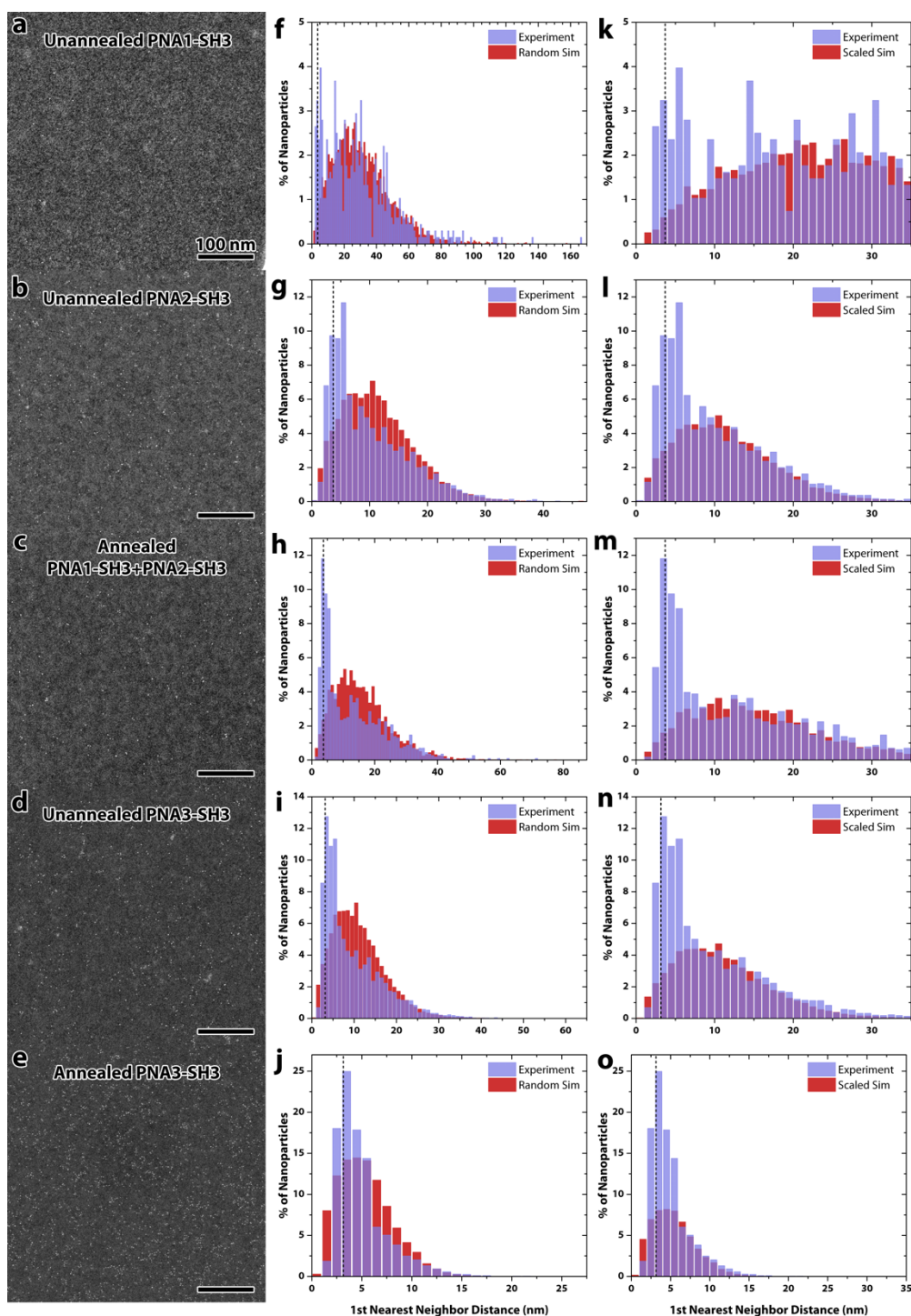


Figure III.10: Example HAADF-STEM micrographs (a-e), experimental and simulated-random nn distance distributions (f-j), and center-to-center nn distributions where the simulated-random distribution has been scaled to the non-spike regions of the experimental (k-o) for each of the five samples examined. The simulated-random distributions are in red, while the experimental are overlaid in semi-transparent blue. The dashed lines correspond to the theoretical max-extension distance assuming fully bonded PNA chains for the given sample. In (k-o), the x-axes for each plot have been set to the same range for ease of visual comparison.

The first nn distributions from the experimental and simulated random datasets for each specimen are shown in

Figure III.10 (f)-(j). The distances analyzed are the center-to-center distances of each AuNC. The vertical dashed lines correspond to the theoretical distance between the centers of two mean-sized AuNCs whose PNA bases have 1:1 bonded to each other and are stretched to max extension: ~ 3.7 nm for the specimens from the system composed of two different PNA chains (

Figure III.10 (f)-(h)) and ~ 3.1 nm for the specimens from the system with a single self-complimentary PNA chain (

Figure III.10 (i),(j)). The shallowness and extent of the PNA 1-SH3 sample is due to the significantly lower spatial density of the AuNCs in the specimen. As can be seen, however, the corresponding simulation takes this into account, highlighting the importance and value of that approach.

In all cases the experimental exhibits significant deviation from random behavior in the form of a spike towards the beginning of the distribution. The bins spanned by the spike as well as the most populated bin are listed in Table III.4. The positions of these spikes are also in good agreement with the distances that would be expected of particles dimerizing through interaction of the PNA chains, centered roughly around the max-extension distance. This is clear evidence of self-assembly into dimers. The spikes are a few bins wide, extending out in both directions from this point. The portion of the spike below the max-extension bin likely corresponds to AuNCs whose PNA chains have bonded but are not stretched out straight. The portion of the spike above the max-extension bin likely corresponds to AuNCs whose PNA chains have partially bonded or are otherwise entangled. This agrees well with the shapes and positions of the spikes, e.g., self-complementary binding of the 2nd and 3rd bases from

the end in PNA2-SH3 (AT to TA) corresponds to a ~5.5 nm distance, which is indeed the most populous bin in the PNA2 distribution. The sharp drop-offs on the right-hand sides of the spikes are also consistent with this interpretation, as beyond a certain distance – $2 \times (\text{NP radius} + \text{PNA chain length})$ – the AuNCs are too far away for any portion of the PNA chains to reach each other. The sigmoidal shape melting curves with a melting transition at ~ 45°C (Figure III.7 and Table III.3) also suggest that the ss-PNA1-SH3 and ss-PNA2-SH3 form secondary structures due their self-complementary nature.

The degree of AuNCs pairing in each specimen was quantified by calculating the portion of the distribution that could not be accounted for by randomly particles. The fitted scaling factors and fraction of dimerized AuNCs are listed in III.4. The first nn distributions with scaled random distributions are shown in

Figure III.10 (k)-(o).

Table III.4: Summary of AuNC pairing behavior from nn distributions. Spike Span is the distance range spanned by the non-random spike. Highest Bin is the bin with the largest population. The scaling factor yielding the best fit to the non-spike regions of each nn distribution and the resulting calculated of % of AuNCs exhibiting non-random pairing are listed in the last two columns.

Specimen*	Spike Span (nm)	Highest Bin (nm)	Scaling Factor	% Non-random
PNA1-SH3 unannealed	2-7	5-6	0.861	11.1
PNA2-SH3 unannealed	2-7	5-6	0.713	26.3
PNA1-SH3+PNA2-SH3 annealed	2-6	3-4	0.681	28.5
PNA3-SH3 unannealed	2-6	3-4	0.647	32.2
PNA3-SH3 Annealed	2-6	3-4	0.566	44.1
PNA3-SH3 Annealed (2 M×)	1.5-4.5	2.5-3	0.539	47.3

*unannealed means as extracted 1xPNA-AuNC conjugates from gels, desalted, lyophilized and dissolved in water. 1xPNA-AuNC conjugates modified with complementary PNA (PNA1-SH3 and PNA2-SH3 or self-complementary PNA3-SH3) were extracted from the gels, desalted, lyophilized and dissolved in water and then mixed and warmed to 80 °C in a heating block and slowly cooled to room temperature to obtain the annealed samples

In the two PNA system, the PNA2-SH3 and mixed specimen exhibited similar overall degrees of pairing, but the other features indicate a difference in the nature of the pairing. The sharper spike of the mixed specimen suggests a more uniform pairing, while the shift in the dominant bin from 5-6 nm down to 3-4 nm is consistent with dimers predominantly of the PNA1-SH1+PNA2-SH3 type rather than the self-complementary partial-bonding that the PNA2-SH3 specimen is limited to. The height of the 5-6 nm bin, however indicates that dimerization due to partial binding was still present. In the one PNA system (PNA3-SH3), annealing not only increased the amount of pairing by ~38%, but also significantly enhanced the uniformity of the dimerization, as evidenced by the much sharper spike and increased relative height of the 3-4 nm bin (corresponding to fully bonded max-extension). As in the previous system, some partial-binding or entanglement still remained.

An additional dataset was acquired from the annealed specimen, this time at a higher magnification (2 M \times) to obtain a finer spatial resolution. An example micrograph and the corresponding full and scaled nn distributions are shown in Figure III.11, with the distribution analysis included in Table III.5. The results are consistent with 500 k \times dataset, confirming the validity of using those magnifications as well as the success of dimerization. The spike is both narrower as well as more strongly centered around the fully bonded max-extension distance, indicating the dimerization was substantial (nearly half) and quite uniform.

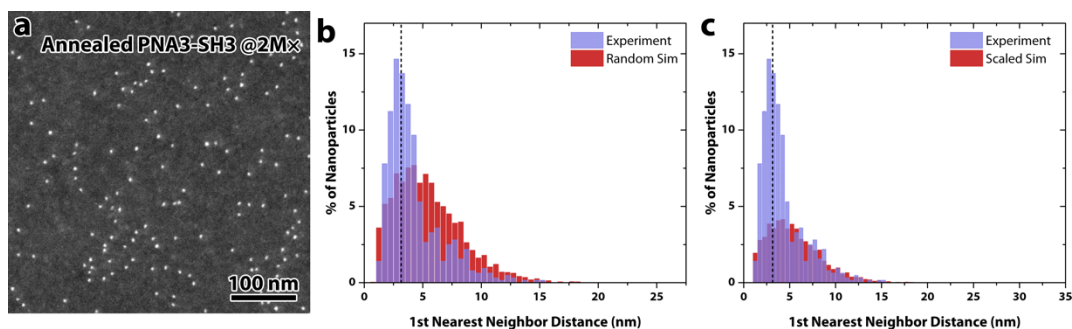


Figure III.11: Example HAADF-STEM micrograph (a), experimental and simulated-random center-to-center nn distance distribution (b), and nn distributions where the random distribution was scaled to the non-spike regions of the experimental (c) for the annealed PNA3-SH3 specimen at 2 M \times magnification. The simulated-random distributions are in red, while the experimental are overlaid in semi-transparent blue.

III.4 Conclusions

Binding of thiol modified PNA oligomers to AuNCs is a statistical process. The number of ss-PNAs that attaches per cluster depends on the molar ratio between PNA and AuNC in the reaction mixture and the type of thiol modification on PNA. Gel electrophoresis successfully separates PNA-AuNC conjugates based on the number of PNA strands attached per each cluster. A simple UV-Vis spectroscopy based method was developed to quantitatively prove that the distinct gel bands that appear during gel electrophoresis are due to AuNC-PNA conjugates bearing a specific number of PNA strands.

The stability of PNA duplexes decreases from 68 $^{\circ}\text{C}$ to 58 $^{\circ}\text{C}$ accompanied by a 16% to 6% hyperchromicity reduction upon AuNC modifications at the ends of the duplexes. Fluorescence emission intensity of AuNC increased when they were modified with PNA. Increments that varied from 1.9 ± 0.3 to 6.7 ± 0.8 were achieved based on the number of PNA strands that were attached per AuNC. The fluorescence emission intensity enhancements were accompanied with a 11-24 nm blue shift in

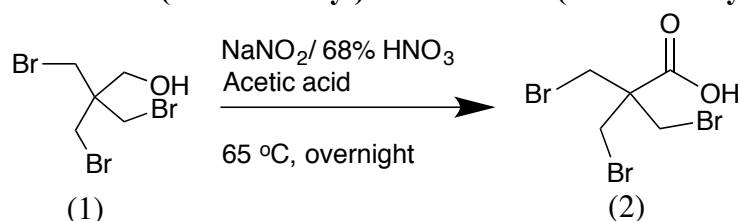
emission maximum wavelength. The chiral properties of AuNC dramatically changed with PNA modifications.

AuNC-PNA conjugates that had one PNA strand attached per cluster were used to make AuNC dimers. STEM image analysis proved the complementary mono-PNA modification can glue two AuNCs together to form AuNC dimers, with dimerization yields as high as 45-50%.

III.5 Material and Methods

III.5.1 Synthesis of 3-(tritylthio)-2,2-bis(tritylthio)methyl propanoic acid.

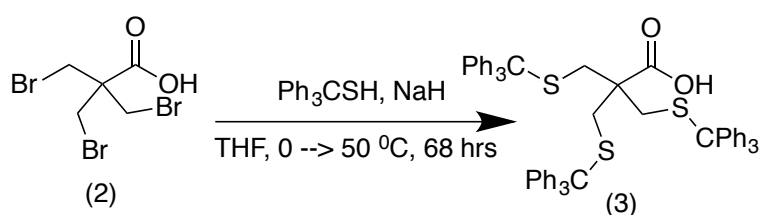
Step 1: Oxidation of tris(bromomethyl)ethanol to tris(bromomethyl)acetic acid.



The procedure from Shimizu et. al.⁴² was modified in two ways to synthesize to *tris*(bromomethyl)acetic acid. First, the reaction mixture was allowed to stir at 65 °C overnight, instead of monitoring the completion of reaction by HPLC after 1 hour of stirring. Secondly, instead of aging the slurry after adding water for 3 hours and further stirring at 5 °C for 1 hour, the reaction mixture was scratched and kept in the fridge for 3 hours to maximize the yield. A few specs of NaNO₂ was dissolved in 68% nitric acid (2.34 ml, 25.2 mmol) and the mixture was heated to 65 °C. Solid tris(bromomethyl)ethanol (**1**; 1g, 3.1 mmol) was dissolved in acetic acid (1 ml) and 10% of this solution was added to nitric acid solution at 65 °C. The reaction mixture was stirred for half an hour. Then, the remaining alcohol was added slowly over about 2 hours. Evolution of brown fumes became intense upon addition of the alcohol. It was continued to stir overnight at 65 °C. Then, it was cooled to 32 °C and stirred for an hour

at the same temperature. After that, the reaction mixture was withdrawn from the reaction flask and cold-water (2.7 ml) was added to it. A milky solution was obtained and it was scratched to yield a white solid. The mixture was kept in the fridge for three hours to maximize the precipitation. The white crystalline solid was filtered and washed with cold water (isolation yield 63 %). ^1H NMR (300 MHz, CDCl_3) δ 3.78 (s, 6H).

Step 2: Synthesis of 3-(tritylthio)-2,2-bis(tritylthio)methyl)propanoic acid.



For the synthesis of 3-(tritylthio)-2,2-bis(tritylthio)methyl)propanoic acid from *tris*(bromomethyl)acetic acid, the procedure from Gasser and co-workers²⁴ was used with no major modification, except the extended reaction time. Triphenylmethanethiol (TCI America: 432 mg, 1.56 mmol) was slowly added to a cooled suspension of NaH (100 mg, 2.35 mmol) in dry THF (10 ml). After 15 min, *tris*(bromomethyl)acetic acid (150 mg, 0.39 mmol) was added. The mixture was heated to 50 °C and stirred at that temperature for 68 hours. The reaction was quenched with water. CH_2Cl_2 (20 ml) and HCl (1M, 8 ml) were added. The layers were separated and the aqueous layer was washed with CH_2Cl_2 (3×20 ml). The combined organic layers were washed with brine, dried (NaSO_4), filtered and concentrated. The crude was purified by column chromatography (hexanes/ethyl acetate 100% to 80%) to obtain pure 3-(tritylthio)-2,2-bis(tritylthio)methyl)propanoic acid as an off-white crystalline solid (isolation yield 40%). ^1H NMR (300 MHz, CDCl_3) δ 7.43-7.34 (m, 18 H), 7.24-7.12 (m, 27 H), 2.29 (s,

6H). m/z calc for $[M-H]^-$ 923.3 and m/z exp for $[M-H]^-$ 922.8, for $2[M-H]^-$ 1848.1 and for $2[M-H]^-Na^+$ 1870.4.

III.5.2 Solid Phase PNA Synthesis

PNA oligomers were synthesized by solid phase Boc-protection peptide synthesis strategy as described in Chapter II, except for the differences that are presented herein.⁴³ The *p*-Methyl-Benzhydrylamine resin.HCl (1.03 meq/g, Peptides International) resin was downloaded to approximately 0.10 meq/g by preloading with a L-glutamic acid using Boc-L-Glu-(OBzl)-OH (Anaspec). Boc-L-Glu-(OBzl)-OH or N-Fmoc-S-trityl-LCysteine (AK Scientific) was coupled on to the resin and/or on to the growing PNA chain using 1-[Bis(dimethylamino)methylene]-1*H*-1,2,3-triazolo[4,5-*b*]pyridinium 3-oxid hexafluorophosphate (HATU from Chem-Impex) and *N,N*-Diisopropylethylamine (DIEA from Sigma Aldrich) as the coupling reagent and the base, respectively. 3-(tritylthio)-2,2-bis(tritylthio)methylpropanoic acid was coupled using 6-Chloro-Benzotriazole-1-yl-oxy-tris-Pyrrolidino-Phosphonium Hexafluorophosphate (Pyclock from Peptides International) as the coupling reagent and DIEA as the base. L-Cysteine modified PNAs were capped with Acetic Anhydride (Sigma Aldrich) prior to cleavage from the resin. PNA oligomers were cleaved from the resin using *m*-cresol (Sigma Aldrich) /thioanisole (Alfa Aesar) /TFMSA (Alfa Aesar) /TFA (EMD Milipore) (1:1:2:6) and two drops of immobilized (tris(2-carboxyethyl)phosphine) disulfide reducing resin (Thermo Scientific). Purification of the PNA was achieved by reversed-phase high pressure liquid chromatography (HPLC). (tris(2-carboxyethyl)phosphine).HCl (Chem-Impex) was added to crude PNA solutions prior to the injection in to HPLC. Molecular weights of purified PNA oligomers were determined by MALDI-ToF mass spectroscopy on an Applied

Biosystems Voyager biospectrometry workstation using 2,5-Dihydroxybenzoic acid as the matrix (10mg/ml in 1:1 acetonitrile: 0.1% trimethylamine in water).

III.5.3 Synthesis and Polyacrylamide gel electrophoretic purification of the $[\text{Au}_{25}(\text{Capt})_{18}]^-$ clusters

$[\text{Au}_{25}(\text{Capt})_{18}]^-$ clusters were synthesized following a published procedure.⁴⁴ The clusters were purified by Polyacrylamide gel electrophoretic purification. The gel was prepared with 15 % acrylamide and 3.3 % bis-acrylamide concentrations (15T/3.3C). The crude $[\text{Au}_{25}(\text{Capt})_{18}]^-$ was loaded on to the wells at a concentration of 9 mg/ml in water and 200 μl per well. The gel was run in 0.5x TBE buffer (44.4 mM Tris, 44.4 mM Boric acid, 1 mM EDTA) at 4 W for 3 hours. Each gel band was crushed and subjected to electroelution at 200 V in 0.5x TBE buffer for 3 hours to efficiently recover the purified $[\text{Au}_{25}(\text{Capt})_{18}]^-$ from the gel slabs. Aliquots of solutions were withdrawn every half an hour from the electroelution chambers to maximize the recovery yield of pure $[\text{Au}_{25}(\text{Capt})_{18}]^-$ clusters. The electroeluted, purified $[\text{Au}_{25}(\text{Capt})_{18}]^-$ clusters were concentrated and desalted on 3 kDa molecular weight cut-off filters. The concentrated ultra-pure $[\text{Au}_{25}(\text{Capt})_{18}]^-$ cluster solution was lyophilized to obtain a dark brown, shiny powder. The molar concentration of the purified $[\text{Au}_{25}(\text{Capt})_{18}]^-$ clusters was determined by using $\epsilon_{670\text{nm}} = 8800 \text{ M}^{-1} \text{ cm}^{-1}$.

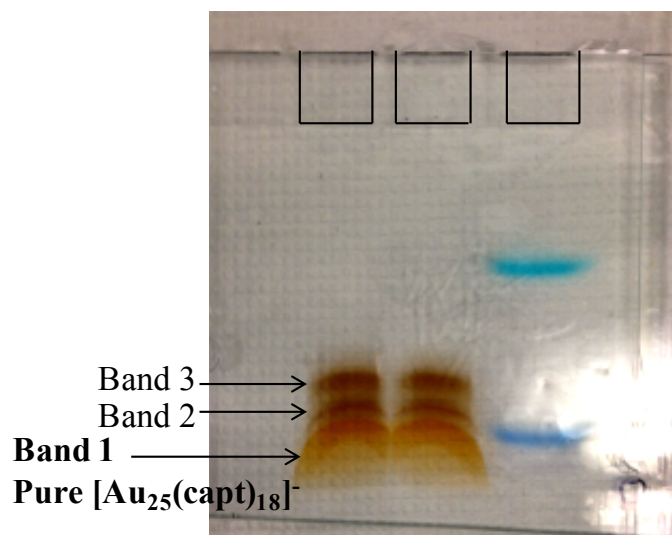
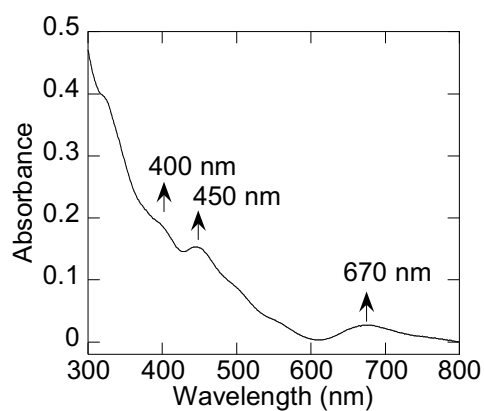
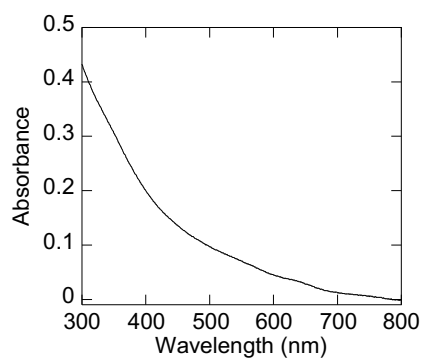


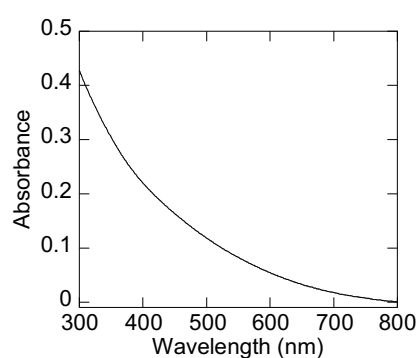
Figure III.12: Gel photograph for purification of $[\text{Au}_{25}(\text{Capt})_{18}]^-$ clusters. Right lane contains Bromophenol blue and Xylene cyanol, which function as a marker to monitor the gel running.



(a)



(b)



(c)

Figure III.13: Absorption spectra for (a) band 1 (pure $[\text{Au}_{25}(\text{Capt})_{18}]^-$), (b) band 2 and (c) band 3. Band 2 and band 3 are impurities, bigger clusters.

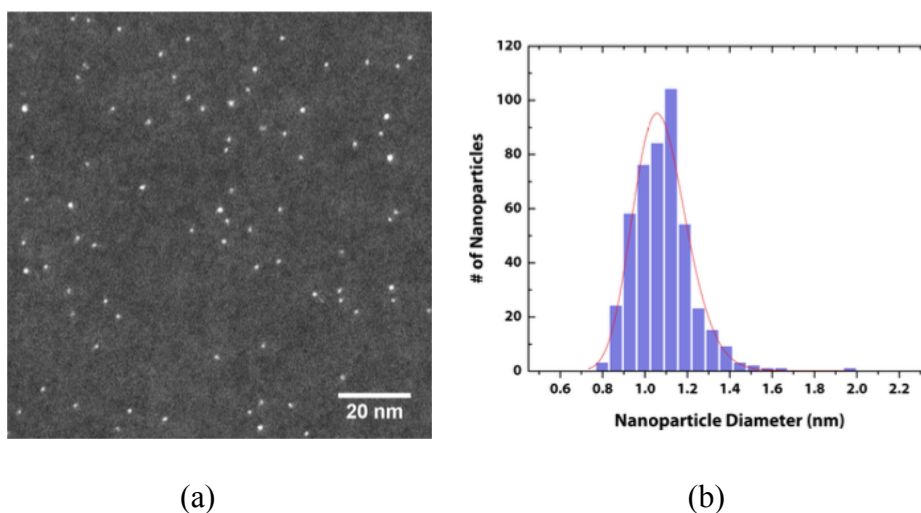


Figure III.14: STEM (a) image and (b) size distribution of purified $[\text{Au}_{25}(\text{Capt})_{18}]^-$ clusters

III.5.4 Synthesis, PAGE purification and Isolation of PNA-AuNC conjugates

The protocol for synthesis and purification of PNA-AuNC conjugations was developed, following a procedure published by Kornberg *et. al.*³⁴ Their protocol explains the synthesis and PAGE purification of 19- or 20-mer mono-thiolated DNAs conjugated on to glutathione-monolayer protected Au_{46} clusters.

We first confirmed that our PNAs attach on to Au_{25} clusters via specific Au-thiol bonds. $[\text{Au}_{25}(\text{Capt})_{18}]^-$ clusters were reacted with PNA1-SH3, PNA2-SH3, PNA1 and PNA2 under the same experimental conditions (see below) and run through gel-electrophoresis (Figure III.15). Only thiol modified PNAs (lanes 3 and 4) give rise to discrete gel bands that are mono- and di-PNA - Au_{25} conjugates. Under these conditions, almost all of the Au_{25} clusters react with PNA1-SH3 and PNA2-SH3. In contrast, PNA1 and PNA2 (lanes 1 and 2) do not show discrete bands that parallel with mono- or di-PNA - Au_{25} conjugates and majority of the Au_{25} clusters remain unreacted. The very top band either can come from unreacted PNAs or from possible aggregates of Au_{25} -PNA. It is not our concern, as far as we can get discrete gel bands for conjugates

bearing defined number of PNAs per clusters, which are only seen when Au₂₅ clusters are incubated with thiol modified PNAs. Therefore, we verify from this experiment that only thiol modified PNAs are capable of forming conjugates with distinct number of PNAs per cluster attached.

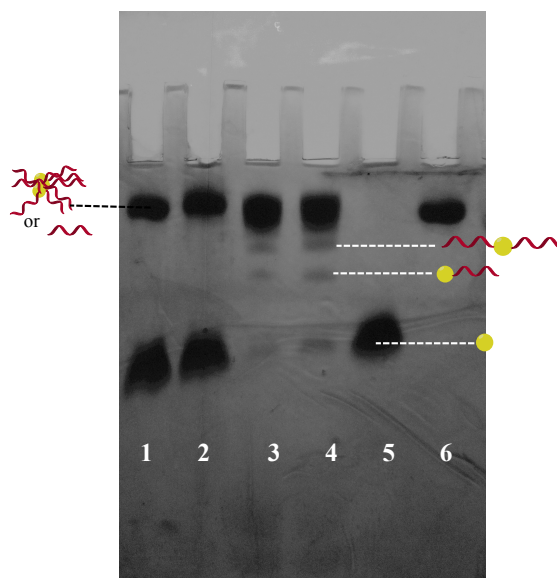
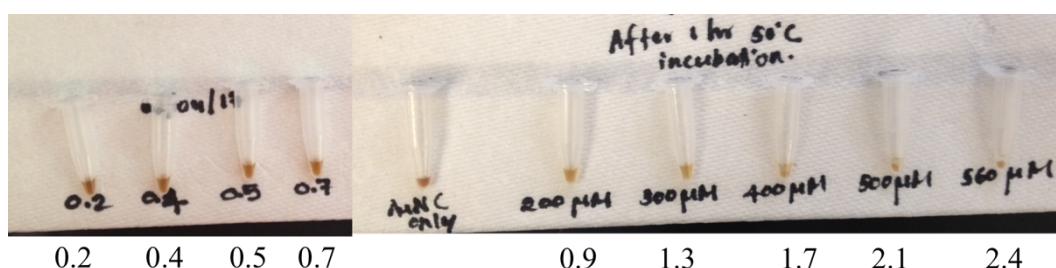


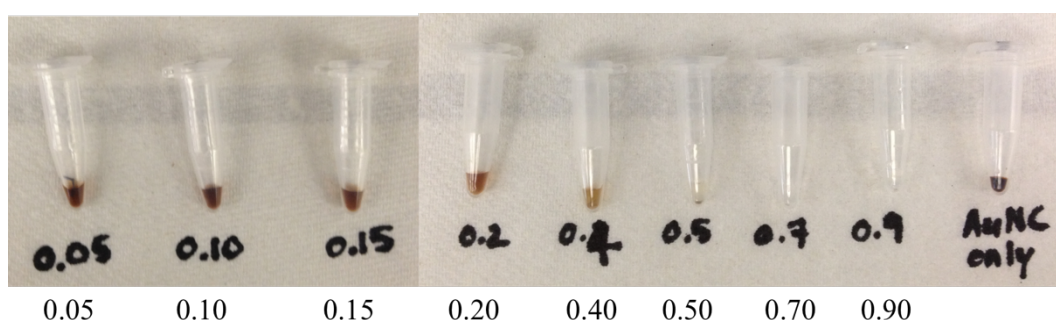
Figure III.15: Gel photograph that shows specific Au-thiol interactions produce Au₂₅-PNA conjugates with distinct number of PNAs per cluster attached. Lane 1: Au₂₅+PNA1, lane 2: Au₂₅+PNA2, lane 3: Au₂₅+PNA1-SH3, lane 4: Au₂₅+PNA2-SH3, lane 5: Au₂₅ NC only, lane 6: PNA only. The top band for lanes 1,2,3 and 4 represents PNA only and/or PNA- Au₂₅ aggregates. The top band for lane 6 is PNA only. Other bands are parallel to the structures illustrated by cartoons. The PNA : Au₂₅ molar ratio used in the reaction mixtures in the gel shown in is 2.4.

Thiol modified PNA oligomers were incubated with Tris(2-carboxyethyl)phosphine (TCEP, Chem impex) at 1:10 molar ratio for half an hour at room temperature. Then, [Au₂₅(Capt)₁₈]⁻ was mixed with PNA solutions at the molar ratios of interest and the reaction mixtures were incubated for one hour in a 50 °C water bath. Samples were then lyophilized and dissolved in 1:1 (v:v) mixture of 10 mM pH 7.00 sodium phosphate buffer : denaturing PAGE gel loading solution to have 0.7 mM PNA concentration in the final solution to load to the gel. Denaturing PAGE gel loading solution consists of 9:1 (v:v) Formamide:pH 8.00 0.1 M EDTA. All the gels for

reaction molar ratio optimization and purification of Au₂₅-PNA conjugates were 15 % acrylamide and 3.3 % bis-acrylamide (15T/3.3C) and run in 0.5x TBE buffer. Analytical gel set-up was used to optimize the reaction molar ratios and was run at a constant 120 V for 1 hour. The PAGE gels for purification of PNA-Au₂₅ conjugates were carried out at a constant 5 W for 3.5 hours. The gel bands that correspond to specific number of PNA-Au₂₅ conjugates were cut, crushed and extracted in a GE Whatman Elutrap electroelution device in 0.5x TBE buffer at a constant 200 V for 3 hours. Mono-PNA-Au₂₅ conjugates for TEM imaging were concentrated and desalted on 3 kDa molecular weight cut-off filters (Merck Millipore). The conjugates for quantification of PNA:Au₂₅ ratio were desalted by Sep-pack C18 classic cartridge (Waters). Desalted conjugates were lyophilized and dissolved in nanopure water.



(a)



(b)

Figure III.16: Reaction mixtures after 1 hour incubation at 50 °C those correspond to gel photographs in (a) Figure III.3 and (b) Figure III.4. Aggregation is visible in the reaction mixtures starting from the PNA: AuNC ratio ~1.7 and ~0.5 for PNA1-SH3 and PNA1-SH1 conjugation, respectively.

III.5.5 Quantification of Au₂₅:PNA ratio in Conjugates

The lyophilized PNA-AuNC conjugates bearing a specific number of ss-PNA attached were dissolved in nanopure water. Dilution of the samples was first adjusted to get a measurable absorbance at 670 nm and the solutions were further diluted to measure the absorbance at 260 nm. Dissolved volumes for 670 nm/260 nm peak detection were, 1xPNA1-SH3 (10 μ l/400 μ l water), 2xPNA1-SH3 (10 μ l/100 μ l), 3xPNA1-SH3 (9 μ l/99 μ l). UV-Vis spectra for the isolated Au₂₅-PNA conjugates were measured in NanoDrop One instrument. Absorption at 670 nm is due to Au₂₅ cluster core HOMO-LUMO electronic transition.³³ $\epsilon_{670\text{nm}}$ for [Au₂₅(Capt)₁₈]⁻ is not reported in literature. $\epsilon_{670\text{nm}}$ for [Au₂₅(SG)₁₈]⁻ is 8800 M⁻¹ cm⁻¹.⁴⁵ Optical properties of Au₂₅ clusters are highly independent from the nature of the surface ligand. Therefore, it is reasonable for one to assume that [Au₂₅(Capt)₁₈]⁻ and [Au₂₅(SG)₁₈]⁻ clusters have similar extinction coefficients at 670 nm to calculate number of moles of Au₂₅ clusters in each extracted conjugate. Both [Au₂₅(Capt)₁₈]⁻ clusters and PNA nucleobases absorb at 260 nm. The relative contribution by each for total absorbance at 260 nm depends on $\epsilon_{260\text{nm}}$ of the two components. While we know the $\epsilon_{260\text{nm}}$ for PNAs (PNA1/2-SH3: 103500 M⁻¹ cm⁻¹, PNA 3-SH3: 81200 M⁻¹ cm⁻¹), $\epsilon_{260\text{nm}}$ for [Au₂₅(Capt)₁₈]⁻ was calculated to be 181020 M⁻¹ cm⁻¹ (Figure III.17). Measured absorbance data, along with respective ϵ values were used to calculate the Au₂₅:PNA molar ratio in each conjugate.

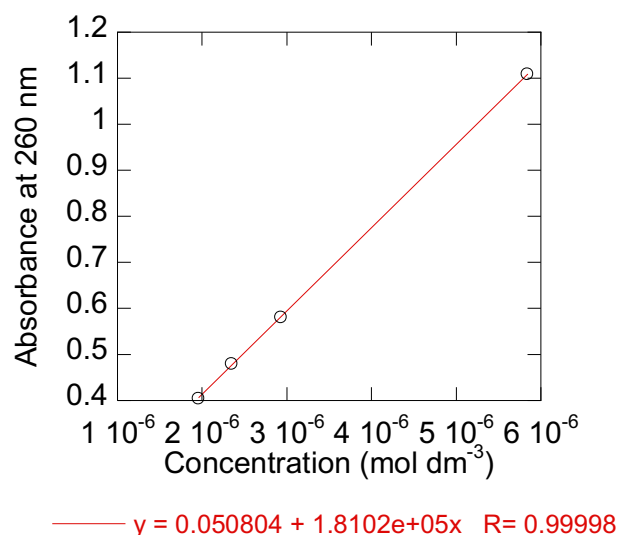


Figure III.17: Plot of absorbance at 260 nm vs concentration to determine $\epsilon_{260 \text{ nm}}$ for $[\text{Au}_{25}(\text{Capt})_{18}]^-$. Concentration of $[\text{Au}_{25}(\text{Capt})_{18}]^-$ was determined based on $\epsilon_{670 \text{ nm}} = 8800 \text{ M}^{-1} \text{ cm}^{-1}$.

Figure III.18 shows the UV-Vis spectra for 1xPNA1-SH1 conjugate to calculate the PNA: AuNC ratio. The PNA1-SH1: Au₂₅ ratio was calculated to be 0.99 ± 0.15 .

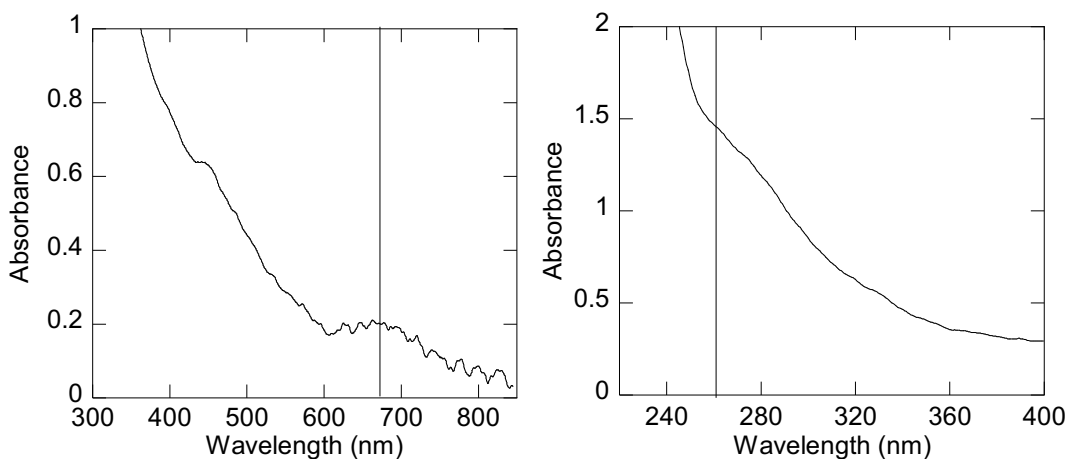


Figure III.18: UV-Vis spectra for 1xPNA1-SH1-Au₂₅ conjugate (a) Au₂₅ absorption region and (b) PNA absorption region. The conjugate was dissolved in 3 μl and 14 μl of nano-pure water to measure the Au₂₅ and PNA absorption, respectively. The solid vertical lines are drawn through 670 nm and 260 nm.

III.5.6 Melting analysis

Melting experiments were done in a Varian Cary 300 spectrophotometer equipped with a programmable temperature block in 1 cm optical-path length, quartz cells. Change in absorbance was monitored both at 260 nm and 670 nm for PNA-Au₂₅ assemblies while only at 260 nm for PNA only samples. The melting curves were recorded from 15-80 °C over two cooling and one heating cycles. The rate of cooling and heating was set to 1 °C/min. The samples were maintained at 80 °C before cooling and at 15 °C before heating, for 2 minutes. The molar ratio between Au₂₅ : PNA was set to 2.4 so that there is no excess Au₂₅ present in the reaction mixture to saturate the detector at 260 nm. Lyophilized reaction mixtures were re-suspended in 10 mM pH 7.00 NaPi buffer.

III.5.7 CD Spectroscopy

The CD spectra were measured on a JASCO J-715 spectrometer equipped with a thermoelectrically controlled, single-cell holder in a 1 cm path length cuvette at 20 °C. The scan rate was 50 nm/min and scan accumulation was 10. PNA-Au₂₅ conjugation reactions were carried out as described in the section of synthesis of PNA-Au₂₅ conjugates, at 2.4 PNA: Au₂₅ molar ratio. When the PNA: Au₂₅ ratio is 2.4, the final product PNA-Au₂₅ conjugates consists of a mixture of conjugates bearing different number of PNAs per cluster attached, with no excess [Au₂₅(Capt)₁₈]⁻ that can mask the inherent CD features of Au₂₅-PNA1-SH3/PNA2-SH3 conjugates. At the end of the conjugation, the reaction mixture was lyophilized and re-dissolved in 10 mM pH 7.00 NaPi buffer. Absorption spectra of dissolved samples were recorded and diluted accordingly to have absorbance at 260 nm around 1, so that the sample does not saturate the CD detector (SI). PNA1-SH3-PNA2-SH3 Au₂₅ assembly sample was prepared by

annealing 1:1 mixture of PNA1-SH3-Au₂₅ : PNA2-SH3 -Au₂₅. The concentration of PNA in CD samples were calculated based on absorbance at 260 nm. The absorption at 670 nm was noisy, which made it impossible for us to specify the exact concentration of Au₂₅ in the samples. However, the initial concentrated samples which were diluted to record the given CD spectra show clear peaks at 670 nm.

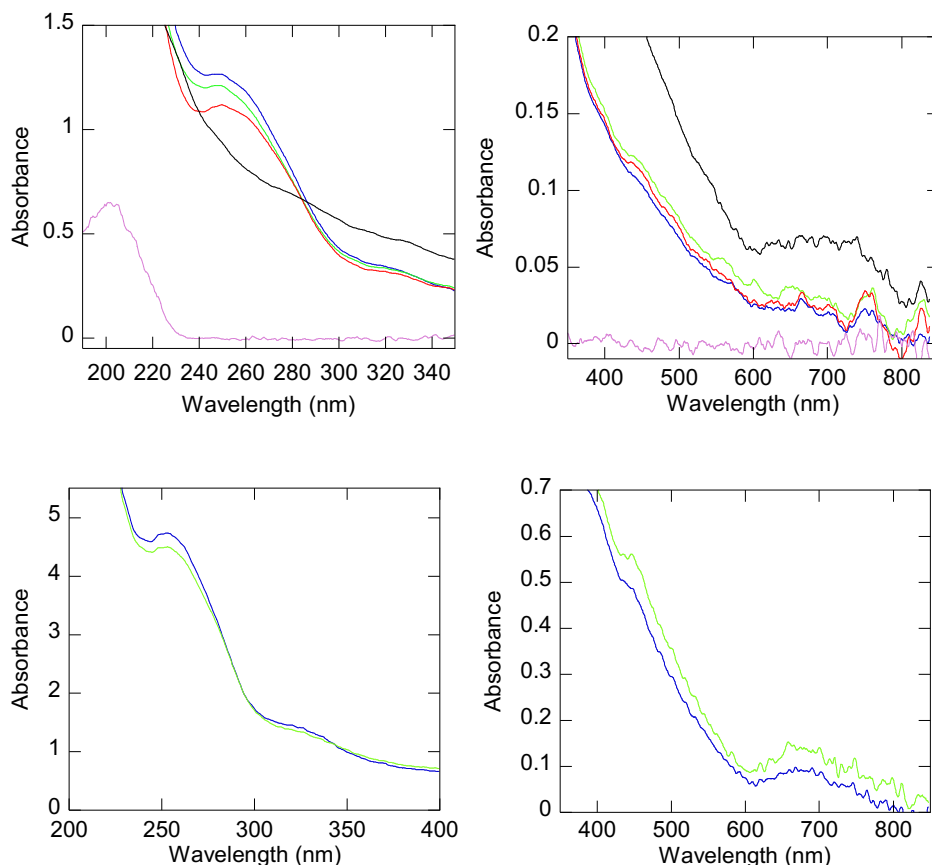


Figure III.19: Absorption spectra for the samples of which CD spectra were measured (a) 200 – 350 nm and (b) 350 -850 nm). (c) and (d) are absorption spectra from 200 – 400 nm and 400 – 850 nm, respectively for concentrated samples of PNA 1-SH3 - Au₂₅ conjugate and PNA 2-SH3 - Au₂₅ conjugate. These samples were diluted by four-fold to prepare the samples of which CD spectra are given in Figure III.8. Line styles are consistent with Figure III.8 caption.

III.5.8 Fluorescence Spectroscopy

We also measured how the fluorescence properties of AuNC are affected upon ss-PNA modifications. The fluorescence emission [Au₂₅(Capt)₁₈]⁻ increases upon

binding of PNA1-SH3 to the cluster. More importantly, we see that the fluorescence intensity enhancement correlates to the number of PNA1-SH3 strands attached per cluster.

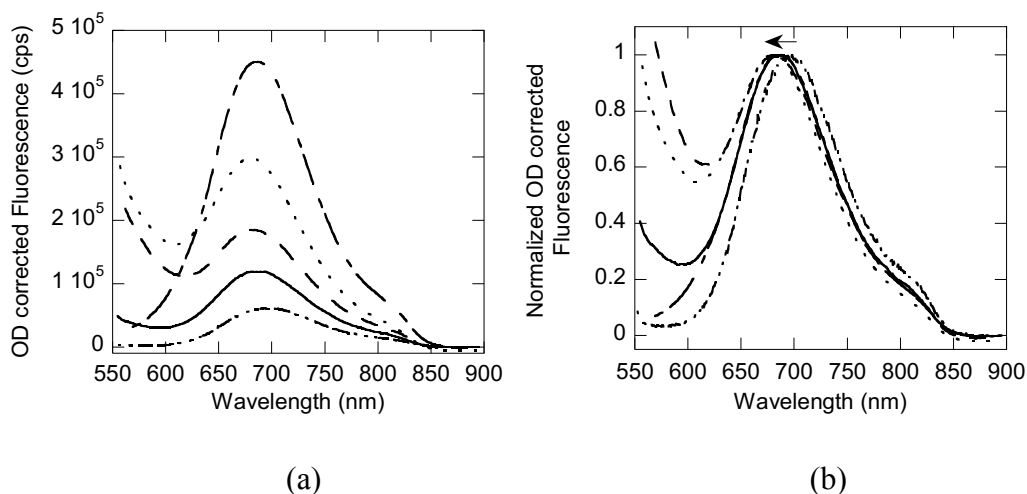


Figure III.20: Fluorescence properties of PNA-Au₂₅ conjugates. (a) Fluorescence emission intensity enhancement and (b) blue shift in emission maxima for [Au₂₅(Capt)₁₈]⁻ clusters (double dotted – double dashed line), 1 PNA1 – Au₂₅ conjugate (solid line), 2 PNA1 – Au₂₅ conjugate (dashed line), 3 PNA1 – Au₂₅ conjugate (dotted line), crude PNA1-Au₂₅ conjugates (dotted-dashed line). Excitation wavelength is 460 nm.

We obtained reproducible results that 1xPNA1-SH3-Au₂₅ fluorescence is ~1.9 times greater than [Au₂₅(Capt)₁₈]⁻ only fluorescence and always lower than 2/3/crude-PNA1-SH3-Au₂₅ fluorescence. Fluorescence intensity enhancements were variable among trials for 2 or 3- PNA1-SH3 conjugates, but always higher than [Au₂₅(Capt)₁₈]⁻ only or 1PNA1-SH3-Au₂₅ fluorescence and lower than crude- PNA1-SH3-Au₂₅. Figure III.20(a) shows results from a trail in which we observed that the fluorescence intensity enhancement correlates exactly with the number of PNA1-SH3 strands attached. Table III.5 summarizes the fluorescence results.

Table III.5: Fluorescence properties of PNA-Au₂₅ conjugates.

Conjugate	FL $\lambda_{em}max$ (nm, Ex at 460 nm)	FL enhancement
[Au ₂₅ (Capt) ₁₈] ⁻	698±1	-
1PNA1-SH3-Au ₂₅	687±1	1.9±0.3
2PNA1-SH3-Au ₂₅	677±2	4.0±1.3
3PNA1-SH3-Au ₂₅	676±3	4.9±0.2
Crude PNA1-SH3-Au ₂₅	684±3	6.7±0.8

Wu and co-worker incubated [Au₂₅(SG)₁₈]⁻ clusters with a very high excess of ssPNA and obtained only ~1.8 times increase in fluorescence intensity.⁴⁶ We also note that in their work, cysteine modified 5-mer PNA was used and excited at 514 nm while we used tri-thiol modified 10-mer PNA and excited at 460 nm, which would also account for any differences between the results. The fact that we see a systematic increase in fluorescence emission with number of PNAs, agrees well the proposed explanation by Wu et. al. because increase in number of bound PNA means, increase in the number of electron rich atoms and functional groups to delocalize the electron density to AuNC surface. We also see that that the emission maximum wavelength of [Au₂₅(Capt)₁₈]⁻ blue shifts with PNA attachment (Figure III.20 (b) and Table III.5). Near infrared fluorescence emission maximum wavelength for Au₂₅⁻ clusters capped with different ligands oscillates ~ 700 nm.^{35, 46-48} Specifically, a similar result to ours was obtained when a 20 nm blue shift in emission maximum was seen as Au₂₅(SG)₁₈ was ligand exchanged with 3-mercapto-2-butanol (MB) to get Au₂₅(MB)₅(SG)₁₃.⁴⁷ Overall, we see that sequential exchange of captopril ligands in [Au₂₅(Capt)₁₈]⁻ clusters with thiol-modified PNA, systematically tune the cluster fluorescence properties. One can also exploit our finding to tailor the AuNC fluorescence by controlling the PNA loading onto AuNCs. Our observations support the existing theory that Au₂₅ nanocluster fluorescence is sensitive to subtle changes of the surface ligand environment.^{46, 48-50}

Fluorescence emission spectra were recorded using a Jobin-Yvon FluorMAX 2. The excitation wavelength was set to 460 nm. All the samples were in nanopure water. Fluorescence spectra were OD corrected by dividing emission data by the absorbance at excitation wavelength, 460 nm.

III.5.9 STEM Imaging and Analysis

Specimens for TEM were prepared by drop-casting 3-4 uL of the suspended AuNC solutions onto ultrathin carbon-coated TEM grids (from Ted Pella). The droplet liquid was carefully wicked away after a given wait time and the remaining liquid film was allowed to dry. A range of wicking times was used for each sample (from 3-60 minutes) with the best resulting dispersion of each selected for subsequent TEM analysis. A JEOL JEM2100F TEM/STEM was operated at a 200 kV accelerating voltage in high-angle annular dark-field (HAADF) imaging mode. A nominal spot size of 0.2 nm, camera length of 20 cm, and dwell time of 64.8 μ s were used. 1024 x 1024 px images for particle size analysis were acquired at a 2 M \times magnification, while images for determining pairing were acquired at 500 k \times . The latter provided the largest field of view possible (to obtain the largest number of particles for better population sizes) while still clearly resolving each AuNC's position to within half a nanometer (pixel size of 0.457 nm). Under these conditions, no changes in the AuNCs were observed during STEM examination. AuNC positions were determined using Find Foci,⁵¹ a plugin for ImageJ⁵², with manual adjustment as needed. Size analysis was performed using WMI⁵³, a freely available MATLAB program.

To briefly summarize the program used to simulate the image, for each experimental micrograph an otherwise identical image, but without any particular interactions beyond that of space occupation, is simulated many times (in this case, 10) using the same spatial density and dimensions. AuNC sizes are determined following

the same distribution as the experimental samples. An equivalent random distribution for each experimental dataset was reconstructed from the corresponding simulated images.

In order to calculate the degree of AuNC pairing, for each specimen, the random-simulation distribution was uniformly scaled to best match the non-spike portion of the experimental distribution through a least-squared fitting approach. Then, for each bin in the spike region (which corresponds to particles interacting via PNA chains), the scaled-simulation value was subtracted from the experimental value. Because these values are all population fractions, the sum of the remainders provides a lower-bound estimate of the fraction of the AuNCs in each specimen that is exhibiting non-random pairing behavior.

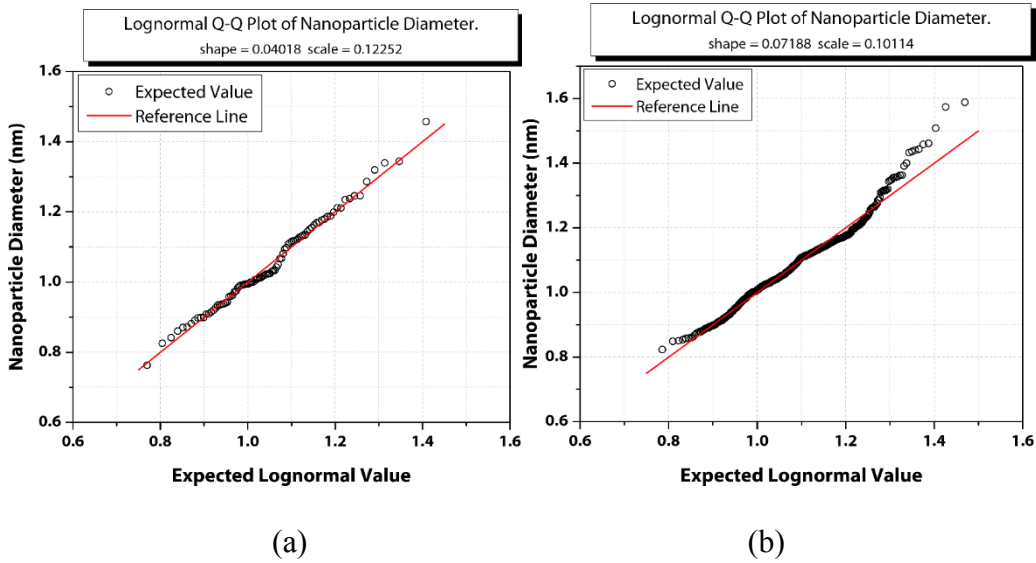


Figure III.21: Lognormal quantile (qq) plots of the size distributions for the (a) annealed PNA1-SH3+PNA2-SH3 and (b) annealed PNA3-SH3 specimens. The red line is a visual guide for an ideal lognormal distribution.

Table III.6: Number of micrographs and total number of nanoparticles comprising each of the experimental datasets used for nearest neighbor analysis.

Sample	Number of Images Analyzed	Total Number of Nanoparticles Analyzed
Unannealed PNA1-SH3	11	680
Unannealed PNA2-SH3	8	3516
Annealed PNA1-SH3+PNA2-SH3	5	1160
Unannealed PNA3-SH3	10	4377
Annealed PNA3-SH3	9	17852
Annealed PNA3-SH3 at 2 M×	5	642

III.6 References

1. Daniel, M.-C.; Astruc, D., Gold nanoparticles: assembly, supramolecular chemistry, quantum-size-related properties, and applications toward biology, catalysis, and nanotechnology. *Chem. Rev.*, **2004**, *104* (1), 293-346.
2. Dreaden, E. C.; Alkilany, A. M.; Huang, X.; Murphy, C. J.; El-Sayed, M. A., The golden age: gold nanoparticles for biomedicine. *Chem. Soc. Rev.*, **2012**, *41* (7), 2740-2779.
3. Boisselier, E.; Astruc, D., Gold nanoparticles in nanomedicine: preparations, imaging, diagnostics, therapies and toxicity. *Chem. Soc. Rev.*, **2009**, *38* (6), 1759-1782.
4. Alivisatos, A. P.; Johnsson, K. P.; Peng, X.; Wilson, T. E., Organization of 'nanocrystal molecules' using DNA. *Nature*, **1996**, *382* (6592), 609.
5. Mirkin, C. A.; Letsinger, R. L.; Mucic, R. C.; Storhoff, J. J., A DNA-based method for rationally assembling nanoparticles into macroscopic materials. *Nature*, **1996**, *382* (6592), 607.
6. Zanchet, D.; Micheel, C. M.; Parak, W. J.; Gerion, D.; Williams, S. C.; Alivisatos, A. P., Electrophoretic and structural studies of DNA-directed Au nanoparticle groupings. *J. Phys. Chem. B*, **2002**, *106* (45), 11758-11763.
7. Piantanida, L.; Naumenko, D.; Lazzarino, M., Highly efficient gold nanoparticle dimer formation via DNA hybridization. *RSC Adv.*, **2014**, *4* (29), 15281-15287.
8. Busson, M. P.; Rolly, B.; Stout, B.; Bonod, N.; Larquet, E.; Polman, A.; Bidault, S., Optical and topological characterization of gold nanoparticle dimers linked by a single DNA double strand. *Nano Lett.*, **2011**, *11* (11), 5060-5065.
9. Park, S. Y.; Lytton-Jean, A. K.; Lee, B.; Weigand, S.; Schatz, G. C.; Mirkin, C. A., DNA-programmable nanoparticle crystallization. *Nature*, **2008**, *451* (7178), 553-556.
10. Storhoff, J. J.; Elghanian, R.; Mucic, R. C.; Mirkin, C. A.; Letsinger, R. L., One-pot colorimetric differentiation of polynucleotides with single base imperfections using gold nanoparticle probes. *J. Am. Chem. Soc.*, **1998**, *120* (9), 1959-1964.
11. Cutler, J. I.; Auyeung, E.; Mirkin, C. A., Spherical nucleic acids. *J. Am. Chem. Soc.*, **2012**, *134* (3), 1376-1391.
12. Rosi, N. L.; Mirkin, C. A., Nanostructures in biodiagnostics. *Chem. Rev.*, **2005**, *105* (4), 1547-1562.
13. Liu, B.; Liu, J., Methods for preparing DNA-functionalized gold nanoparticles, a key reagent of bioanalytical chemistry. *Anal. Methods*, **2017**, *9* (18), 2633-2643.
14. Taton, T. A., Preparation of gold nanoparticle–DNA conjugates. *Current Protocols in Nucleic Acid Chemistry*, **2002**, 12.2.1-12.2.12.

15. Chakrabarti, R.; Klibanov, A. M., Nanocrystals Modified with Peptide Nucleic Acids (PNAs) for Selective Self-Assembly and DNA Detection. *Journal of the American Chemical Society*, **2003**, *125* (41), 12531-12540.
16. Duy, J.; Connell, L. B.; Eck, W.; Collins, S. D.; Smith, R. L., Preparation of surfactant-stabilized gold nanoparticle-peptide nucleic acid conjugates. *J. Nanopart. Res.*, **2010**, *12* (7), 2363-2369.
17. Murphy, D.; Redmond, G.; de la Torre, B. G.; Eritja, R., Hybridization and melting behavior of peptide nucleic acid (PNA) oligonucleotide chimeras conjugated to gold nanoparticles. *Helvetica chimica acta*, **2004**, *87* (11), 2727-2734.
18. Seferos, D. S.; Giljohann, D. A.; Rosi, N. L.; Mirkin, C. A., Locked nucleic acid-nanoparticle conjugates. *ChemBioChem*, **2007**, *8* (11), 1230-1232.
19. McKenzie, F.; Faulds, K.; Graham, D., LNA functionalized gold nanoparticles as probes for double stranded DNA through triplex formation. *Chem. Commun.*, **2008**, (20), 2367-2369.
20. Zu, Y.; Ting, A. L.; Yi, G.; Gao, Z., Sequence-selective recognition of nucleic acids under extremely low salt conditions using nanoparticle probes. *Anal. Chem.*, **2011**, *83* (11), 4090-4094.
21. Zhao, Y.; Cao, L.; Ouyang, J.; Wang, M.; Wang, K.; Xia, X.-H., Reversible plasmonic probe sensitive for pH in micro/nanospaces based on i-motif-modulated morpholino-gold nanoparticle assembly. *Anal. Chem.*, **2012**, *85* (2), 1053-1057.
22. Duy, J.; Connell, L.; Eck, W.; Collins, S.; Smith, R., Preparation of surfactant-stabilized gold nanoparticle-peptide nucleic acid conjugates. *J. Nanopart. Res.*, **2010**, *12* (7), 2363-2369.
23. Anstaett, P.; Zheng, Y.; Thai, T.; Funston, A. M.; Bach, U.; Gasser, G., Synthesis of Stable Peptide Nucleic Acid-Modified Gold Nanoparticles and their Assembly onto Gold Surfaces. *Angewandte Chemie International Edition*, **2013**, *52* (15), 4217-4220.
24. Anstaett, P.; Zheng, Y.; Thai, T.; Funston, A. M.; Bach, U.; Gasser, G., Synthesis of Stable Peptide Nucleic Acid-Modified Gold Nanoparticles and their Assembly onto Gold Surfaces. *Angew. Chem. Int. Ed.*, **2013**, *52* (15), 4217-4220.
25. Zanchet, D.; Micheel, C. M.; Parak, W. J.; Gerion, D.; Alivisatos, A. P., Electrophoretic isolation of discrete Au nanocrystal/DNA conjugates. *Nano Lett.*, **2001**, *1* (1), 32-35.
26. Claridge, S. A.; Goh, S. L.; Fréchet, J. M.; Williams, S. C.; Micheel, C. M.; Alivisatos, A. P., Directed assembly of discrete gold nanoparticle groupings using branched DNA scaffolds. *Chem. Mater.*, **2005**, *17* (7), 1628-1635.
27. Pellegrino, T.; Sperling, R. A.; Alivisatos, A. P.; Parak, W. J., Gel electrophoresis of gold-DNA nanoconjugates. *BioMed Res. Int.*, **2008**, *2007*.
28. Gearheart, L. A.; Ploehn, H. J.; Murphy, C. J., Oligonucleotide adsorption to gold nanoparticles: a surface-enhanced Raman spectroscopy study of intrinsically bent DNA. *J. Phys. Chem. B*, **2001**, *105* (50), 12609-12615.
29. Parak, W. J.; Pellegrino, T.; Micheel, C. M.; Gerion, D.; Williams, S. C.; Alivisatos, A. P., Conformation of oligonucleotides attached to gold nanocrystals probed by gel electrophoresis. *Nano Lett.*, **2003**, *3* (1), 33-36.
30. Storhoff, J. J.; Elghanian, R.; Mirkin, C. A.; Letsinger, R. L., Sequence-dependent stability of DNA-modified gold nanoparticles. *Langmuir*, **2002**, *18* (17), 6666-6670.
31. Jin, R., Quantum sized, thiolate-protected gold nanoclusters. *Nanoscale*, **2010**, *2* (3), 343-362.
32. Jin, R.; Zeng, C.; Zhou, M.; Chen, Y., Atomically precise colloidal metal nanoclusters and nanoparticles: Fundamentals and opportunities. *Chem. Rev.*, **2016**, *116* (18), 10346-10413.

33. Zhu, M.; Aikens, C. M.; Hollander, F. J.; Schatz, G. C.; Jin, R., Correlating the crystal structure of a thiol-protected Au₂₅ cluster and optical properties. *J. Am. Chem. Soc.*, **2008**, *130* (18), 5883-5885.
34. Ackerson, C. J.; Sykes, M. T.; Kornberg, R. D., Defined DNA/nanoparticle conjugates. *Proc. Natl. Acad. Sci. U.S.A.*, **2005**, *102* (38), 13383-13385.
35. Kumar, S. Synthesis, Characterization and Application of Water-soluble Gold and Silver Nanoclusters. Carnegie Mellon University, 2013.
36. Jhaveri, S. D.; Foos, E. E.; Lowy, D. A.; Chang, E. L.; Snow, A. W.; Ancona, M. G., Isolation and characterization of trioxethylene-encapsulated gold nanoclusters functionalized with a single DNA strand. *Nano Lett.*, **2004**, *4* (4), 737-740.
37. Wittung, P.; Nielsen, P. E.; Buchardt, O.; Egholm, M.; Norde, B., DNA-like double helix formed by peptide nucleic acid. *Nature*, **1994**, 561-563.
38. Wittung, P.; Eriksson, M.; Lyng, R.; Nielsen, P. E.; Norden, B., Induced chirality in PNA-PNA duplexes. *J. Am. Chem. Soc.*, **1995**, *117* (41), 10167-10173.
39. Jin, R.; Wu, G.; Li, Z.; Mirkin, C. A.; Schatz, G. C., What controls the melting properties of DNA-linked gold nanoparticle assemblies?, *J. Am. Chem. Soc.*, **2003**, *125* (6), 1643-1654.
40. Brittain, H. G.; Kadin, H., Ultraviolet (UV) Absorption and Circular Dichroism (CD) Spectra of Captopril. *Pharmaceutical research*, **1990**, *7* (10), 1082-1085.
41. Zhu, M.; Qian, H.; Meng, X.; Jin, S.; Wu, Z.; Jin, R., Chiral Au₂₅ nanospheres and nanorods: synthesis and insight into the origin of chirality. *Nano Lett.*, **2011**, *11* (9), 3963-3969.
42. Osato, H.; Kabaki, M.; Shimizu, S., Development of safe, scalable nitric acid oxidation using a catalytic amount of NaNO₂ for 3-Bromo-2, 2-bis (bromomethyl) propanoic acid: an intermediate of s-013420. *Org. Process Res. Dev*, **2011**, *15* (3), 581-584.
43. Christensen, L.; Fitzpatrick, R.; Gildea, B.; Petersen, K. H.; Hansen, H. F.; Koch, T.; Egholm, M.; Buchardt, O.; Nielsen, P. E.; Coull, J., Solid-phase synthesis of peptide nucleic acids. *J. Pept. Sci.*, **1995**, *1* (3), 175-183.
44. Kumar, S.; Jin, R., Water-soluble Au₂₅ (Capt) 18 nanoclusters: Synthesis, thermal stability, and optical properties. *Nanoscale*, **2012**, *4* (14), 4222-4227.
45. Negishi, Y.; Nobusada, K.; Tsukuda, T., Glutathione-protected gold clusters revisited: Bridging the gap between gold (I)-thiolate complexes and thiolate-protected gold nanocrystals. *J. Am. Chem. Soc.*, **2005**, *127* (14), 5261-5270.
46. Wu, Z.; Jin, R., On the ligand's role in the fluorescence of gold nanoclusters. *Nano Lett.*, **2010**, *10* (7), 2568-2573.
47. Shibu, E.; Muhammed, M. H.; Tsukuda, T.; Pradeep, T., Ligand exchange of Au₂₅SG18 leading to functionalized gold clusters: spectroscopy, kinetics, and luminescence. *J. Phys. Chem. C*, **2008**, *112* (32), 12168-12176.
48. Devadas, M. S.; Kim, J.; Sinn, E.; Lee, D.; Goodson III, T.; Ramakrishna, G., Unique ultrafast visible luminescence in monolayer-protected Au₂₅ clusters. *J. Phys. Chem. C*, **2010**, *114* (51), 22417-22423.
49. Wang, S.; Zhu, X.; Cao, T.; Zhu, M., A simple model for understanding the fluorescence behavior of Au₂₅ nanoclusters. *Nanoscale*, **2014**, *6* (11), 5777-5781.
50. Weerawardene, K. D. M.; Aikens, C. M., Theoretical Insights into the Origin of Photoluminescence of Au₂₅ (SR) 18-Nanoparticles. *J. Am. Chem. Soc.*, **2016**, *138* (35), 11202-11210.
51. Herbert, A. D.; Carr, A. M.; Hoffmann, E., FindFoci: a focus detection algorithm with automated parameter training that closely matches human assignments, reduces

human inconsistencies and increases speed of analysis. *PloS one*, **2014**, 9 (12), e114749.

52. Schneider, C. A.; Rasband, W. S.; Eliceiri, K. W., NIH Image to ImageJ: 25 years of image analysis. *Nat Meth*, **2012**, 9 (7), 671-675.

53. House, S. D.; Chen, Y.; Jin, R.; Yang, J. C., High-throughput, Semi-automated Quantitative STEM Mass Measurement of Supported Metal Nanoparticles Using a Conventional TEM/STEM. *Ultramicroscopy*, **2017**, 182, 145-155.

CHAPTER IV: Chirality Based Probing of Plasmon-Dot Coupling

The work presented in this chapter is a collaboration project with Professor Yossi Paltiel's group from the Hebrew University of Jerusalem, Israel. I worked on synthesis and characterization of opposite handed PNA oligomers. Device fabrication and extinction measurements were done by Lior Bezen. Results were discussed and interpreted by all the authors.

IV.1 Introduction

Semiconductor colloidal quantum dots (CQDs) have electrical and optical properties that can be tuned by varying the size¹⁻², shape³ and extent of impurity doping.⁴ Self-assembled hybrid CQDs coupled with specific organic linker molecules, are a promising way to realize spectrally-tunable photovoltaics⁵, light-emitting diodes⁶⁻⁷ and photodetectors⁸ that operate at room-temperature. However, these devices demonstrate low quantum efficiency due to low light absorption ability of CQDs.⁷⁻⁹ Therefore, there is a need to develop simple and cost-effective ways to enhance the light absorption ability of CQDs to develop sensitive devices. One way to enhance absorption of CQDs is to couple them to plasmonics.¹⁰ Since the surface plasmon of Au nanoparticles depends on size, shape and local environment¹¹, plasmonics can be used to control light at nanoscale dimensions. As plasmonic modes exhibit highly confined fields, they locally increase light-matter interactions and consequently enhance the performance of CQD-based devices. This effect has previously been used to increase absorption efficiency by enhancing the photoluminescence.¹²⁻¹⁶

Recently, Paltiel and co-workers reported a large extinction enhancement from a monolayer of CQDs coupled to random Au nanoparticle islands by an achiral organic molecule.¹¹ Three plasmonic Au nanoislands of thicknesses 2, 5 and 7 nm with different

plasmonic resonances and four types of CQDs (CdS 420 nm, CdSe 520 nm, CdSe 610 nm and PbS 850 nm) were used in their study. A light extinction up to 16% (13-fold enhancement) compared to the reference self-assembled monolayer of CQDs on a glass substrate was achieved by matching the plasmonic resonance frequency and the band gaps of CQDs. The random Au nanoislands functioned as plasmonic antennas to induce the observed extinction enhancement. The random structures guarantee no sensitivity to the light polarization changes. Theoretical calculations using a two-dimensional finite-difference, time-domain method demonstrate plasmonic control of the enhancement factor near the Au nanoislands' plasmon resonance.¹⁷

Chiral molecules have identical composition and connectivity but can adopt conformations that are non-superimposable mirror images of each other, these different conformations have left or right symmetry. Recent experiments have shown that ordered films of chiral organic molecules on surfaces can act as electron spin filters with an efficiency of up to 60% at room temperature.¹⁸ This effect is called the chiral-induced spin selectivity (CISS),¹⁹ opened the possibility of using chiral molecules to create spin-specific devices operated at room temperature. Some works present chiral imprinting using chiral molecule,²⁰ a common approach for preparing chiral surfaces based on molecular monolayers using chiral molecules as templates, which allows the easy design of chiral materials with specific properties related to those of the molecules used as templates. Paltiel and co-workers created a thin-layer, nano-scale charge separation device which operates at room temperature using semiconductor CQDs and chiral helical peptides.²¹ The device operation was explained based on CISS effect and chiral imprinting on semiconductor CQDs by chiral helical peptides.

In this chapter, we show that the extinction enhancement in the visible spectrum by random Au nanoislands and CQD monolayer is higher when the linkers between the

nanoislands and the CQDs is made of helical chiral molecules when compared to achiral molecules. The chiral molecules improve the light extinction using random Au nanoislands that act as plasmonic antennas. A light extinction of up to 35% is attained when the plasmonic resonance of the Au nanoislands and the bandgap of the CQDs deposited onto the nanoislands are matched. This extinction is 28-fold higher than that measured for a monolayer of CQDs in the absence of the Au nanoislands.

For the work presented in this chapter, self-assembled monolayers of left- or right-handed PNA duplexes on Au nanoislands were used. The left- and right-handed PNAs were made by incorporating (R) and (S)- γ -Serine-PNA monomers, respectively, at intermittent positions along the PNA oligomer chain. The PNA duplex monolayers were attached to CQDs by C-terminal glutamic acid modification. The helicity of the ss- and duplex PNAs in solution were characterized by circular dichroism (CD) spectroscopy. The stability of the duplexes was accessed by UV-melting.

IV.2 Research Design

In the work by Paltiel and coworkers, they used an achiral organic linker molecule, 1,9-nonanedithiol, to create a monolayer of CdSe CQDs to Au plasmonic nanoislands and achieved a 13-fold light extinction enhancement.¹⁰ In this project, we chose to substitute the achiral linker, by a chiral linker, and study the effect on extinction properties of a monolayer of CQDs coupled to Au nanoislands. Ly and coworkers showed that a randomly coiled PNA can be pre-organized in to a right-handed helical structure by introducing a (S)-serine modification at the γ -position of N-(2-aminoethyl) glycine (AEG) unit of the PNA backbone.²² Similarly, one can synthesize left-handed PNA by introducing (R)-serine modification at the γ -position of the PNA monomer. We decided to synthesize both right- and left-handed PNA and

study the effect of both handed linkers on extinction properties of the monolayers CdSe CQDs coupled on Au nanoislands. We anticipated the possibility to link the CdSe QDs to Au nanoislands by opposite-handed chiral molecules would add another control parameter to tune the extinction properties of CQD based future electronic devices.

CD spectra for ss-PNA with one, three or ten γ -(R)-serine modifications in the AEG unit of PNA backbone show similar biphasic exciton coupling pattern that is characteristic for a right-handed helix and the peak intensity at 260 nm does not change significantly with increase number of γ -modifications.²² Based on these results, we chose to synthesize the 10-mer PNAs which have similar nucleobase composition reported by Ly et.al. and to synthesize them with three γ -(S) or (R)-serine modifications. The complementary PNA strand was synthesized with no γ -modification as one γ -modified ss-PNA in a PNA homoduplex is enough to induce a preferred helicity. ss- γ -PNA strands were modified with D or L-Glutamic acid (Glu) at the C-end to couple the PNAs onto QDs. We incorporated D-Glu to (S)-serine PNA and L-Glu to (R)-serine PNA so that the helicity induced by the γ -monomers matches with the helicity induced by the terminal amino acid modification. The PNA sequences are given in Table IV.1.

Table IV.1: PNA Sequences and MALDI data

Abbreviation	PNA sequence (N to C)	MWcalc/exp
PNA 1S	H-GC ^S ATG ^S TTT ^S GA- ^D Glu-NH ₂	2976.88/2976.44
PNA 1R	H-GC ^R ATG ^R TTT ^R GA- ^L Glu-NH ₂	2976.88/2975.80
PNA 2	H-TCAAACATGC-NH ₂	2695.65/2964.69

*Underlined letters show γ -modified PNA monomers. Superscripts stand for specific enantiomer of γ -modified PNA monomers and terminal amino acid.

IV.3 Results and Discussion

IV.3.1 Thermal Stability and Helicity Characterization of PNA Duplexes

Duplexes PNA 1S.PNA 2 and PNA 1R.PNA have the same melting temperature $T_m = 60$ °C (Figure IV.1).

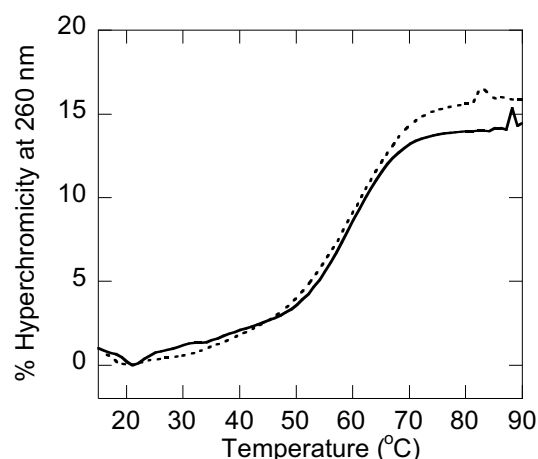


Figure IV.1: Melting curves measured at 260 nm for 5 μ M solutions of duplexes PNA 1S.PNA 2 (black dotted line) and PNA 1R.PNA 2 (black solid line) in 10 mM pH 7.00 NaPi buffer.

The CD spectra for ss- and duplex PNAs are shown in Figure IV.2. The exciton coupling pattern with minima at ~ 220 and 260 nm and a maximum at ~ 280 nm observed for both single stranded PNA 1R and duplex PNA 1R.PNA is indicative of a left-handed helical structure, which is in agreement with results previously reported for PNA containing γ -(S)-serine modifications.²²⁻²³ The spectra obtained for ss-PNA 1S and PNA 1S.PNA 2 are mirror images of those for ss-PNA 1R and PNA 1R.PNA 2, which indicates that the γ -(S)-serine modification induces a right-handed structure. Amplitudes of all the CD peak intensities are higher for duplexes compared to ss-PNAs. The increase in 260 nm peak intensity, which is due to the nucleobase absorption, indicates improved base stacking in duplexes compared to a ss-PNAs. The peak in the region of 200-230 nm is due to $n-\pi^*$ transitions in the amide backbone. This peak intensity is significantly higher for PNA duplexes compared to ss-PNA. It can be attributed to the increase in helical twist, reflecting the tightening of the backbone conformation, as ss-PNAs hybridize to form duplexes. Analysis of CD spectra confirms

that the γ -(S) and (R)-serine backbone modifications induce right and left handed helical structures, respectively, in both ss- and PNA homo-duplexes.

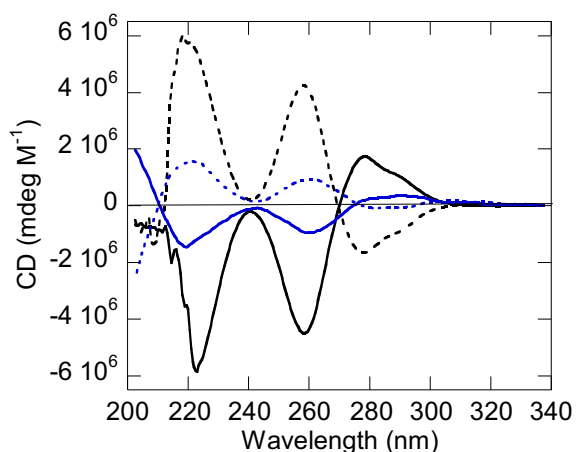


Figure IV.2: CD spectra of 5 μ M solutions of duplexes PNA 1S.PNA 2 (black dotted line) and PNA 1R.PNA 2 (black solid line) and of 2 μ M solutions of single stranded PNA 1S (blue dotted line), and single stranded PNA 1R (blue solid line). All the samples were prepared in 10 mM pH 7.00 NaPi buffer.

IV.3.2 Light Extinction Measurements

Plasmonic properties are highly dispersive.²⁴ Consequently, spectral analysis is a common tool for the characterization of the surface plasmons. In order to estimate the effects of the monolayer of organic molecules that connects the random-shaped Au nanoislands and the CQDs, we measured separately and then compared the light extinction properties of the monolayer of CQDs and random-shaped Au nanoislands in the presence of absence of the monolayer of Au nanoislands. Comparison of the light enhancement caused by chiral and achiral linker molecules was used to identify the effect of the chirality on the light extinction. The light extinction by a device with a given CQD and Au nanoislands should depend on the spectral overlap of the two

resonances of these components and not on the organic linker between the two components if the dipole-dipole interactions are random in direction.¹⁰

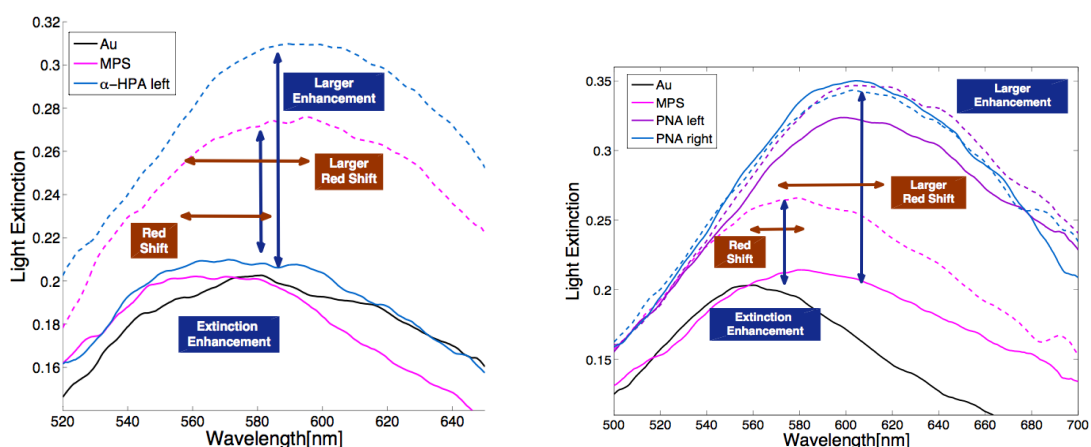


Figure IV.3: Light extinction spectra for samples that have a monolayer of achiral (MPS, pink) or chiral molecules α -HPA (a, blue lines) and γ -PNA (b, purple lines for left-handed PNA and pink lines for right handed PNA) on top of Au nanoislands created from a 5 nm-thick layer of evaporated Au. The solid lines correspond to samples without CQDs; the dashed lines correspond to samples that have adsorbed CQDs. The horizontal arrows mark the red shift in the position of the maximum light extinction caused by the adsorption of CQDs. The vertical arrows identify the increase in light extinction due to adsorption of CQDs, at the wavelength of the maximum light extinction for samples that have the CQDs.

The data shown in Figure IV.3 reflects a 28-fold enhancement in light extinction of the CQDs on the plasmonic samples with chiral molecules compared to the light extinction of a single quantum dot monolayer without Au nanoislands which is around 1.1% at peak (Refer to the work by Paltiel and co-workers¹⁰ for this spectrum). The enhancement for the MPS achiral molecules 13-fold, which is consistent with our previous work on achiral molecules.¹⁰ The relative enhancement depends on the detuning between the quantum dot band gap and the plasmonic resonance through the molecules. Nevertheless, for all the detuning range, using the same CQD and Au nanoislands a two-fold enhancement is measured for chiral linkers as compared to the non-chiral molecules. Furthermore, a clear red shift is seen for the CQD - Au nanoisland

coupling through both achiral and chiral molecules. The red shift observed for chiral molecules is larger than that for achiral molecules, which indicates that chiral molecules support a better Au nanoislands-CQDs coupling than the achiral ones.

We attribute this high enhancing effect to the chiral imprinting on the Au nanoislands and QDs, which aligns the dipole moments of the CQDs parallel to the dipole moment of the Au nanoislands. While an achiral molecule has very low polarization parallel to the Au surface, the chiral molecules induce about the same magnitude of polarization parallel and perpendicular to the surface. This argument based on dipole alignment is supported by the fact that the enhancement is larger for the γ -PNA, which has a diameter of ~ 2 nm, and thus a larger interface area with the CQD than α -HPA, which has a 1.2 nm diameter.

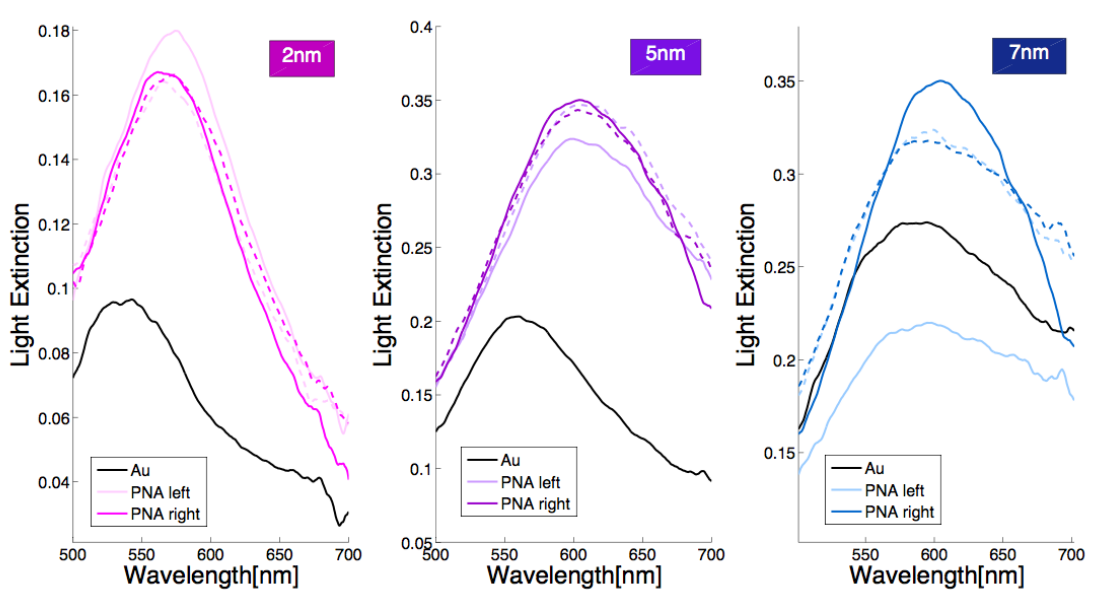


Figure IV.4: The light extinction of the samples that have monolayers of chiral PNA on Au nanoislands obtained from evaporated Au with 2, 5 or 7nm thickness. The solid lines correspond to the light extinction by the random-shaped Au nanoislands that have a PNA (left/right) monolayer. The dashed lines correspond to samples which a CQD monolayer was added over the PNA (left/right) monolayer.

Figure IV.4 shows the light extinction of the samples due to the adsorption of the CQD monolayers on top on the chiral molecules using evaporated Au that has 2 nm, 5 nm or 7 nm thickness. As the nominal thickness of the Au film increases, the light extinction of the plasmonic NP increases to the point where the plasmonic extinction peak becomes less obvious due to light scattering from the sample (as expected for a metallic layer). Also, as the thickness increases, the islands start to connect, the plasmonic chiral imprinting is less pronounced, and the in-plane plasmonic dipole moment is reduced. Note that the large extinction enhancement at the peak is consistent with the results shown in Figure IV.3.

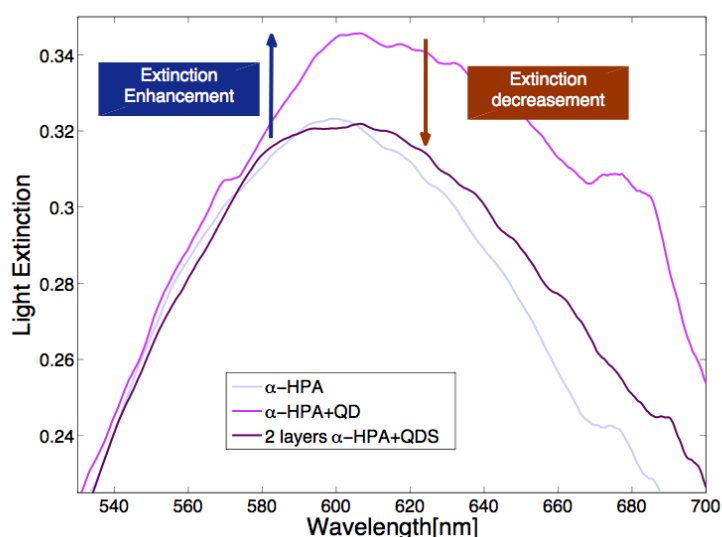


Figure IV.5: The changes in light extinction due to the adsorption of another chiral molecules layer on top of the CQDs monolayer.

Figure IV.5 shows the light extinction due to the adsorption of an additional layer of chiral molecules on top of the CQDs monolayer (besides the layer of chiral molecules situated between the Au nanoislands and the CQDs). This data indicates that the light extinction decreases when the second layer of the chiral molecules is adsorbed on top of the CQDs. Also, the red shift of the maximum light extinction caused by the adsorption of the CQDs on the first monolayer of chiral molecules is reduced by the

layer of chiral molecules adsorbed on top of the CQDs. These two results strengthen the argument that the symmetry-breaking caused by imprinting chirality to one side of the CQDs is the main reason for the extinction ratio enhancement. The layer of chiral molecules added on top of the CQDs causes a reduction in the alignment of the dipole moment of the CQDs with respect to the dipole moment of the Au nanoislands because it restores (some of) the symmetry that was broken by the chiral imprinting effect exerted by the first layer of chiral molecules.

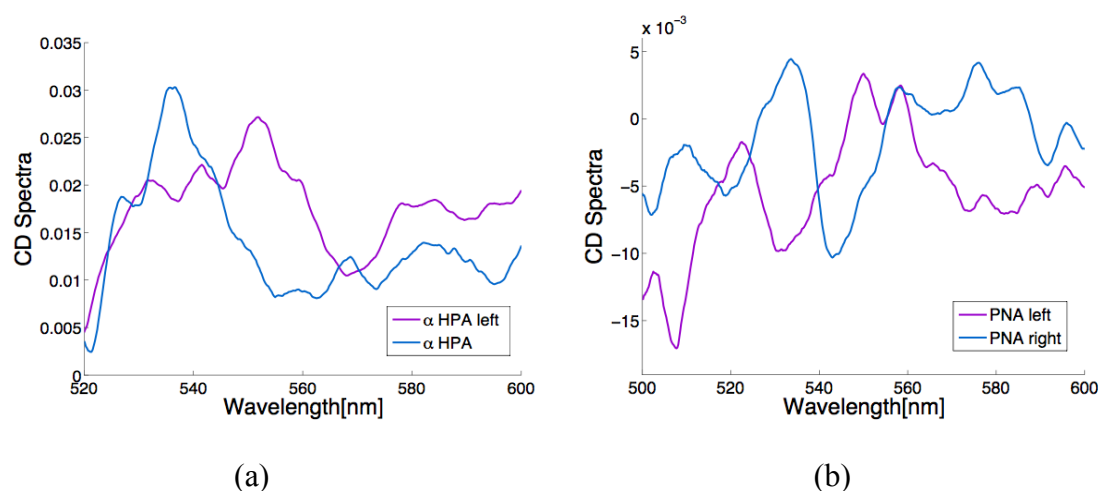


Figure IV.6: CD spectra of a monolayer of chiral organic molecules on top of the Au nanoislands structure (a) α -HPA or (b) γ -PNA) measured using a circular polarized light source and calculated as the difference between the light extinction of a sample measured using left circular polarized light and the light extinction of the same sample measured using right circular polarized light.

The same system seems to enable measuring for the first time the circular dichroism originating from a single adsorbed chiral monolayer. We are sensitive only in wavelength that are in proximity the Au nanoisland resonance. For this type of measurement, the resonance should be tuned to the required CD spectra range. In Figure IV.6 CD spectra of a monolayer of chiral organic molecules α -HPA or γ -PNA on top of the Au nanoislands. The CD spectra are calculated as the difference between light extinction spectra measured using left circular polarized light and light extinction

spectra measured using right circular polarized light. The spectra are noisy but shows around 1% change between the two helicities. Similar spectra are measured using different samples. Using silver nanoislands and smaller CQDs the resonance could be shifted to the UV range and is expected to result in a less noisy behavior.

IV.4 Conclusions

The chiral molecules enhance the light extinction by a monolayer of CQDs using random Au nanoislands that act as plasmonic antennas. The extinction enhancement is higher for chiral γ -PNAs compared to chiral α -HPA. By matching the plasmonic resonance and the colloidal quantum dots' bandgap, we achieve light extinction of up to 35%, which represents a 28-fold enhancement over a reference that has a monolayer of CQD only. This surprising effect results from the coupling between the chiral plasmons and the quantum dots, which breaks the symmetry of the plasmonic coupling and align the dipole-dipole interactions. The same effect could be used to map the circular dichroism of the monolayers of chiral molecules. These results may pave the way toward realizing more efficient and sensitive photon detectors and may provide a simple way to map circular dichroism of chiral monolayers.

IV.5 Material and Methods

γ -(S)/(R)-serine modified AEG PNA monomer synthesis reactions were performed under nitrogen atmosphere unless otherwise stated. All commercially available materials were used without further purification unless otherwise specified. Anhydrous solvents, purchased from EMD Millipore, such as dimethylformamide (DMF), dichloromethane (DCM), and tetrahydrofuran (THF), were dried by standard methods and freshly distilled prior to use. All anhydrous reagents were purchased

from Sigma Aldrich. Common reagents were purchased from either Chem-Impex or Alfa Aesar.

The two polyalanine molecules with two opposite handedness, AHPA-L and AHPA-D handedness, were purchased from Sigma Adrich. These peptides contain L- and D-amino acids, (H-CAAAAKAAAAKAAAAKAAAAKAAAAKAAAAKAAAAK-OH respectively, where C, A, and K represent cysteine, alanine and lysine, respectively. Both molecules adopt an α -helix structure.

IV.5.1 Solid-Phase PNA Synthesis

The Boc/Z-PNA monomers were purchased from Polyorg and ASM Research Chemicals and used with no further purification. Boc-protected γ -(S)/(R)-serine modified AEG PNA monomers were synthesized by adapting previously published procedures.^{22, 25} PNA oligomers were synthesized by solid phase Boc-protection peptide synthesis strategy.²⁶ p-Methyl-Benzhydrylamine resin.HCl (1.03 meq/g, Peptides International) was used as the solid support for PNA synthesis. The resin was downloaded to between 0.10 meq/g by preloading with D- and L –Glutamic acid for PNA 1S and PNA 1R, respectively, using Boc-D- or L- Glu-OBzl (Anaspec) and with Boc/Z- C- PNA monomer for PNA 2. PNA oligomers were cleaved, purified as described in Chapter II. Mass of PNA oligomers MALDI-ToF-MS using 2,5-Dihydroxybenzoic acid (for PNA 1S and PNA 1R) or α -cyano-4-hydroxycinnamic acid (for PNA 2) as the matrix (10mg/ml in water/acetonitrile, 0.1% TFA). Concentrations of PNA solutions were determined as described in Chapter II.

IV.5.2 Sample Preparations for Extinction Measurements

The samples were prepared in four main steps A-D. Figure IV.7 shows the sample after each of these preparation steps.

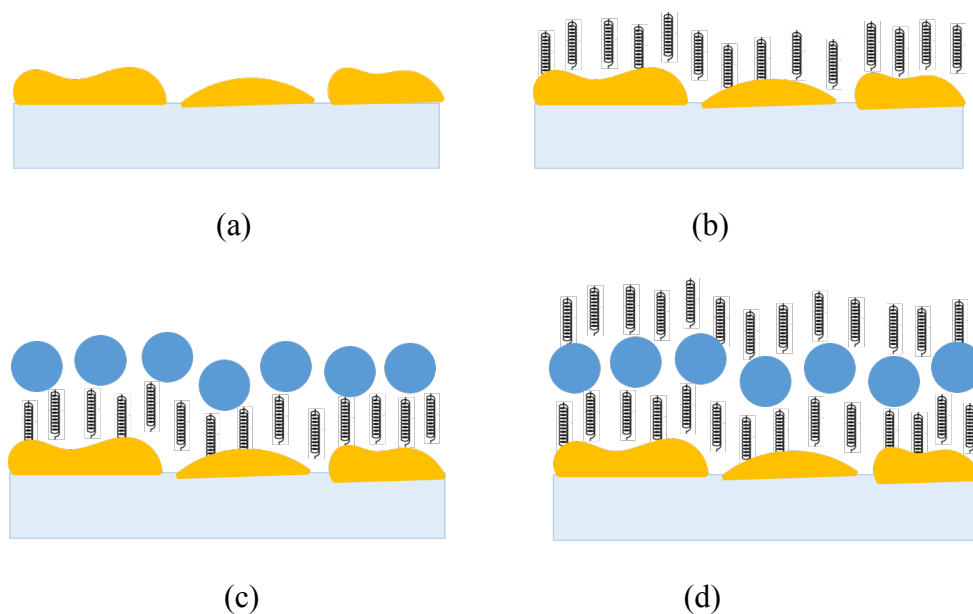


Figure IV.7: (a) Schematic sketch of the plasmonic layer of Au nanoislands evaporated on top of a glass substrate; (b) A homogeneous, closely-packed monolayer of organic molecules is covalently-adsorbed onto plasmonic layer of Au nanoislands. The organic molecules may be chiral or achiral. (c) CdSe CQDs with energy band gap of 590nm is covalently adsorbed onto the monolayer of organic molecules. (d) Lastly, an additional monolayer of organic molecules similar to those used in step (b) is formed on top of the monolayer of CQDs.

(A) Au nanoislands were created in step A. First, thin 2 nm, 5 nm or 7 nm Au nanoparticles were evaporated on top of cleaned glass substrates. Then the samples were annealed on a hot plate at 400°C for several minutes to form random-shaped, Au plasmonic islands, termed nanoislands through this manuscript. Figure IV.8 shows that the size of the nanoislands increased with the thickness of the layer of Au NPs evaporated on the glass substrate. The nanoisland structures are stable for months at ambient conditions enabling wet chemistry processes that withstand washing and rinsing with water or organic solvents.

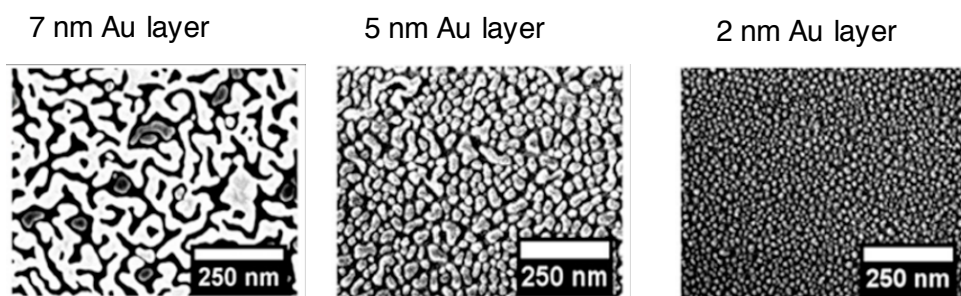


Figure IV.8: Au nanoislands evaporated on top of a glass substrate. The size of the islands depends on the Au thickness of the layer of Au NPs evaporated onto the glass surface, which was (a) 7 nm, (b) 5 nm, or (c) 2 nm.

(B) In the second step, a homogeneous, closely-packed monolayer of organic molecules was covalently adsorbed on the Au nanoislands by immersing the samples in solutions of the organic molecules for 3 hours. Five types of organic molecules have been used: achiral (3-Mercaptopropyl)trimethoxysilane (MPS), α -helix L-polyalanine (HPA), which is right-handed, α -helix D-polyalanine, left handed, and right- and left-handed peptide nucleic acid (PNA). The organic molecules bound to the Au nanoislands through thiol linkers (MPS and polyalanine) or amino linkers (PNA). **(C)** The samples were washed with the solvent that dissolves the organic molecules and then immersed in a dilute 0.1% (w/w) solution of CdSe CQDs with band gap 590 nm for 3 hours. Lastly, they were cleaned with toluene. The structure of the device is shown in Figure 3. Figure IV.9.

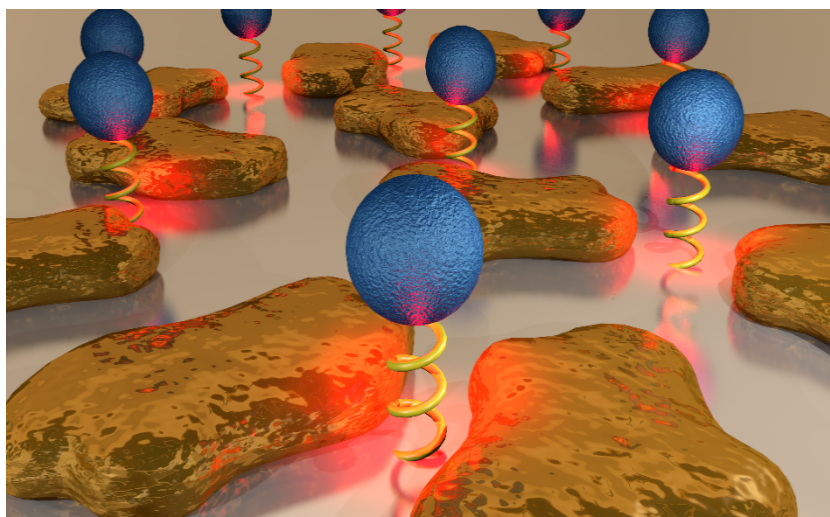


Figure IV.9: The device contains CdSe CQDs (blue) attached to Au nanoislands through chiral (yellow) or achiral molecules.

(D) Another homogeneous, closely-packed monolayer of organic molecules was adsorbed on top of the layer of the CQDs.

IV.5.3 Light Extinction Curve Measurements

The light transmission and reflection spectra were measured using high intensity LED as a white light source and an integrating sphere (Figure IV.10). A linear polarizer and quarter wave plate were placed in front of the light source to determine the polarization of the exciting light. The light extinction of the sample is mostly due to absorption because the measured reflection of the samples is very small and the scattering is minimized in this optical setup. The spectra were recorded using Ocean Optics usb4000 VIS-NIR spectrometer.

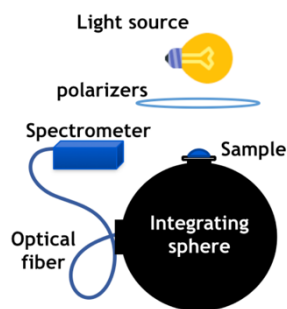


Figure IV.10: Experimental set up for measuring the extinction spectra.

IV.5.4 UV-Melting and CD Spectroscopy

Variable temperature UV-vis experiments for PNA duplexes and CD spectroscopy for ss- and duplex PNAs were performed as explained in Chapter II. Experimentally obtained CD spectra were corrected for concentration and plotted in the y-axis. Absorption spectra were recorded for each sample of which CD spectra were recorded. In the case of duplexes, the absorption spectra were recorded at 90 °C and 15 °C. The decrease in absorbance at 260 nm with decreasing temperature proves that the ss-PNA hybridized with complementary strands to form the duplexes (Figure IV.11).

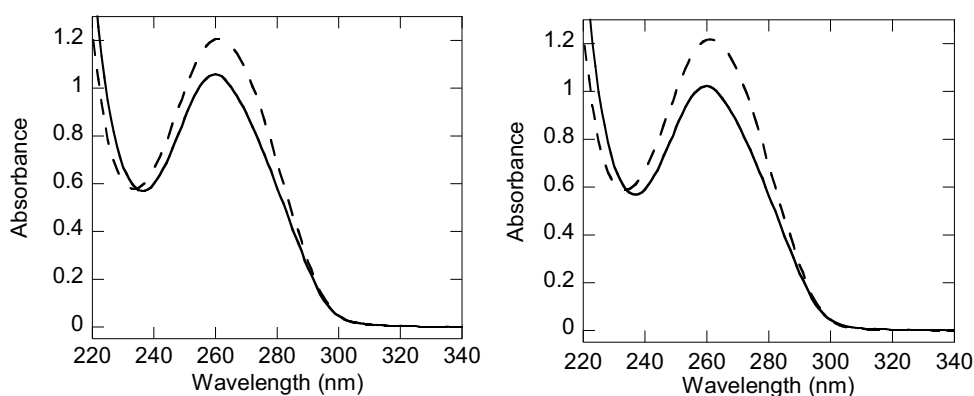


Figure IV.11: Absorption spectra at 90 °C (dashed line) and 15 °C (solid line) for 5 μ M CD samples of (a) PNA 1S.PNA 2 and (b) PNA 1R.PNA 2.

IV.6 References

1. Moras, J. D.; Strandberg, B.; Suc, D.; Wilson, K., Semiconductor clusters, nanocrystals, and quantum dots. *Science*, **1996**, *271*, 933.
2. Murray, C.; Norris, D. J.; Bawendi, M. G., Synthesis and characterization of nearly monodisperse CdE (E= sulfur, selenium, tellurium) semiconductor nanocrystallites. *J. Am. Chem. Soc.*, **1993**, *115* (19), 8706-8715.
3. Peng, X.; Manna, L.; Yang, W.; Wickham, J.; Scher, E.; Kadavanich, A.; Alivisatos, A. P., Shape control of CdSe nanocrystals. *Nature*, **2000**, *404* (6773), 59-61.
4. Mocatta, D.; Cohen, G.; Schattner, J.; Millo, O.; Rabani, E.; Banin, U., Heavily doped semiconductor nanocrystal quantum dots. *Science*, **2011**, *332* (6025), 77-81.
5. Chistyakov, A. A.; Zvaigzne, M. A.; Nikitenko, V. R.; Tameev, A. R.; Martynov, I. L.; Prezhdo, O. V., Optoelectronic Properties of Semiconductor Quantum Dot Solids for Photovoltaic Applications. *J. Phys. Chem. Lett.*, **2017**, *8* (17), 4129-4139.
6. Sun, Q.; Wang, Y. A.; Li, L. S.; Wang, D.; Zhu, T.; Xu, J.; Yang, C.; Li, Y., Bright, multicoloured light-emitting diodes based on quantum dots. *Nat. Photonics*, **2007**, *1* (12), 717-722.
7. Caruge, J.; Halpert, J. E.; Wood, V.; Bulović, V.; Bawendi, M., Colloidal quantum-dot light-emitting diodes with metal-oxide charge transport layers. *Nat. Photonics*, **2008**, *2* (4), 247-250.
8. Clifford, J. P.; Konstantatos, G.; Johnston, K. W.; Hoogland, S.; Levina, L.; Sargent, E. H., Fast, sensitive and spectrally tuneable colloidal-quantum-dot photodetectors. *Nat. Nanotechnol.*, **2009**, *4* (1), 40-44.
9. Debnath, R.; Bakr, O.; Sargent, E. H., Solution-processed colloidal quantum dot photovoltaics: A perspective. *Energy & Environmental Science*, **2011**, *4* (12), 4870-4881.
10. Galanty, M.; Yochelis, S.; Stern, L.; Dujovne, I.; Levy, U.; Paltiel, Y., Extinction enhancement from a self-assembled quantum dots monolayer using a simple thin films process. *J. Phys. Chem. C*, **2015**, *119* (44), 24991-24995.
11. Myroshnychenko, V.; Rodríguez-Fernández, J.; Pastoriza-Santos, I.; Funston, A. M.; Novo, C.; Mulvaney, P.; Liz-Marzán, L. M.; de Abajo, F. J. G., Modelling the optical response of gold nanoparticles. *Chem. Soc. Rev.*, **2008**, *37* (9), 1792-1805.
12. Kwon, M. K.; Kim, J. Y.; Kim, B. H.; Park, I. K.; Cho, C. Y.; Byeon, C. C.; Park, S. J., Surface-plasmon-enhanced light-emitting diodes. *Advanced Materials*, **2008**, *20* (7), 1253-1257.
13. Liang, Z.; Sun, J.; Jiang, Y.; Jiang, L.; Chen, X., Plasmonic enhanced optoelectronic devices. *Plasmonics*, **2014**, *9* (4), 859-866.
14. Ming, T.; Chen, H.; Jiang, R.; Li, Q.; Wang, J., Plasmon-controlled fluorescence: beyond the intensity enhancement. *J. Phys. Chem. Lett.*, **2012**, *3* (2), 191-202.
15. Song, J.-H.; Atay, T.; Shi, S.; Urabe, H.; Nurmikko, A. V., Large enhancement of fluorescence efficiency from CdSe/ZnS quantum dots induced by resonant coupling to spatially controlled surface plasmons. *Nano Lett.*, **2005**, *5* (8), 1557-1561.
16. Mendes, M. J.; Hernández, E.; López, E.; García-Linares, P.; Ramiro, I.; Artacho, I.; Antolín, E.; Tobías, I.; Martí, A.; Luque, A., Self-organized colloidal quantum dots and metal nanoparticles for plasmon-enhanced intermediate-band solar cells. *Nanotechnology*, **2013**, *24* (34), 345402.
17. Purcell, T. A.; Galanty, M.; Yochelis, S.; Paltiel, Y.; Seideman, T., Coupling Quantum Emitters to Random 2D Nanoplasmonic Structures. *J. Phys. Chem. C*, **2016**, *120* (38), 21837-21842.

18. Göhler, B.; Hamelbeck, V.; Markus, T.; Kettner, M.; Hanne, G.; Vager, Z.; Naaman, R.; Zacharias, H., Spin selectivity in electron transmission through self-assembled monolayers of double-stranded DNA. *Science*, **2011**, *331* (6019), 894-897.
19. Naaman, R.; Waldeck, D. H., Chiral-induced spin selectivity effect. *J. Phys. Chem. Lett.*, **2012**, *3* (16), 2178-2187.
20. Maoz, B. M.; Chaikin, Y.; Tesler, A. B.; Bar Elli, O.; Fan, Z.; Govorov, A. O.; Markovich, G., Amplification of chiroptical activity of chiral biomolecules by surface plasmons. *Nano Lett.*, **2013**, *13* (3), 1203-1209.
21. Peer, N.; Dujovne, I.; Yochelis, S.; Paltiel, Y., Nanoscale charge separation using chiral molecules. *ACS Photonics*, **2015**, *2* (10), 1476-1481.
22. Dragulescu-Andrasi, A.; Rapireddy, S.; Frezza, B. M.; Gayathri, C.; Gil, R. R.; Ly, D. H., A simple γ -backbone modification preorganizes peptide nucleic acid into a helical structure. *J. Am. Chem. Soc.*, **2006**, *128* (31), 10258-10267.
23. Sahu, B.; Sacui, I.; Rapireddy, S.; Zanotti, K. J.; Bahal, R.; Armitage, B. A.; Ly, D. H., Synthesis and characterization of conformationally preorganized,(R)-diethylene glycol-containing γ -peptide nucleic acids with superior hybridization properties and water solubility. *J. Org. Chem.*, **2011**, *76* (14), 5614-5627.
24. Yao, K.; Liu, Y., Plasmonic metamaterials. *Nanotechnology Reviews*, **2014**, *3* (2), 177-210.
25. Beall, E.; Ulku, S.; Liu, C.; Wierzbinski, E.; Zhang, Y.; Bae, Y.; Zhang, P.; Achim, C.; Beratan, D. N.; Waldeck, D. H., Effects of the Backbone and Chemical Linker on the Molecular Conductance of Nucleic Acid Duplexes. *J. Am. Chem. Soc.*, **2017**, *139* (19), 6726-6735.
26. Christensen, L.; Fitzpatrick, R.; Gildea, B.; Petersen, K. H.; Hansen, H. F.; Koch, T.; Egholm, M.; Buchardt, O.; Nielsen, P. E.; Coull, J., Solid-phase synthesis of peptide nucleic acids. *J. Pept. Sci.*, **1995**, *1* (3), 175-183.

CHAPTER V: Spin Dependent Mechanism of Charge Transfer through Helical Peptides

This chapter presents the results of a collaborative project with the group of Prof. Ron Naaman from the Weizmann Institute of Science, Rehovot, Israel. I worked on synthesis and characterization of opposite-handed, helical peptides. Self-assembled monolayer preparations, characterizations, electrochemistry, contact potential difference (CPD) and superconducting quantum interference device (SQUID) measurements were done by Francesco Tassinari. The results were discussed by all authors.

V.1 Introduction

Metal-based conductors, semiconductors, and conjugated polymers are used as electron transport materials in most man-made electronic devices. Electrons are also transferred in living beings, in order to transfer energy and information from one place to another. Chiral/helical proteins are used to transfer electrons in living systems.¹ The investigation of the charge transfer through proteins is important, not only to gain a better understanding of biological functions, but also to design future molecular electronic devices at nanoscale.²

Self-assembled monolayers of peptides modified with a redox group such as ferrocene (Fc) and attached to gold surfaces are a popular tool to study and model charge transfer through proteins. To date, a large number of peptides has been studied.³ The charge transfer through peptides monolayers depends on many properties of the peptide chain such as the length,⁴⁻⁷ dipole moment,⁸⁻¹¹ the secondary structure,¹²⁻¹³ hydrogen bonding capability,¹⁴⁻¹⁵ backbone conformation¹⁶ and the quality of monolayer.¹⁷ Two main mechanisms have been proposed to explain the charge transfer between a donor and an acceptor bridged by a peptide. They are electron tunneling and

hopping.^{4-7, 18-21} As shown in Figure V.1, reported by Arikuma and co-workers,⁴ electronic coupling between an acceptor and a donor through molecular orbitals of the peptide bridge underscores the electron transfer by tunneling mechanism. They also report that, in the hopping mechanism, electrons “hop” from a donor to an acceptor through the peptide bridge using amide groups as the hopping sites for electron transfer. The peptide length is the main determinant factor to decide whether the electrons travel by tunneling or hopping. Electron transfer mechanism switches from tunneling to hopping when the peptide exceeds a certain length. The charge transfer rate constant decreases exponentially as the peptide length increases when tunneling is the operating mechanism.²⁰ The charge transfer rate constants show weak distance dependence in the case of hopping mechanism.^{4, 6-8}

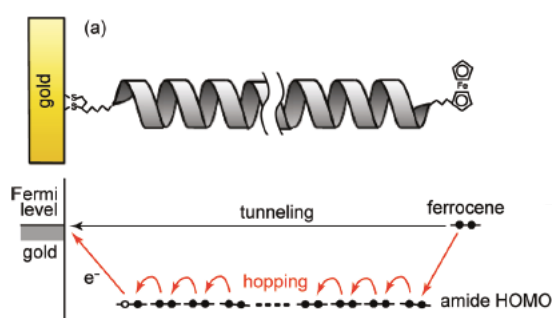


Figure V.1: A schematic diagram of electron tunneling and hopping mechanisms of electron transfer from ferrocene (donor) to Au surface (acceptor), connected by a helical peptide bridge. “Reprinted (adapted) with permission from the reference⁴. Copyright (2011) American Chemical Society.”

Experimentally, it has also been shown that the electron transmission through chiral peptides is spin selective.²² Naaman and co-workers studied spin selectivity of electron transmission through right-handed (Ala:Alanine-Leu:Leucine)_n peptides (n=5-7) by photoelectron spectroscopy, electrochemistry and single molecule conduction.²² Photoelectron experiment showed that the majority of electrons that travel through the

peptides and reach the detector have a negative spin polarization. Electrons are negative spin polarized means, majority of the electrons have spin orientations antiparallel to the direction of propagation. Higher(-17%) and lower(-11%) spin polarizations were observed for (AlaLeu)₇ and (AlaLeu)₅, respectively. Polarization of the detected electrons increased linearly with the length of the peptide. Cyclic Voltammetry was used to determine the effect of applied magnetic field direction on the charge transfer through the peptides. If the current varies with the applied magnetic field direction, that means the electron transfer through peptides is spin selective. They observed that the current for both oxidation and reduction of the Fe²⁺/Fe³⁺ redox couple, depends on the direction of the applied magnetic field, for all three peptides. They also showed that the spin selective electron transfer through the peptides can be seen only if the α -helicity of the peptide remains intact. In a different study, Naaman and co-workers used conductive atomic force microscopy to show the spin dependent electron conduction through right-handed helical peptides of two different lengths, (Ala-2-aminoisobutyric acid:Aib)₅ and (Ala-Aib)₇.²³ The spin selectivity increased with the length of the peptides.

Spin selectivity of electron transfer through chiral peptides was explained based on the “Chiral Induced Spin Selectivity” (CISS) effect.²⁴ Transfer of one electron spin orientation (spin orientation parallel or antiparallel to the direction of propagation), to one direction through one enantiomer of a chiral molecule is favoured than the transfer of the same spin through the same enantiomer to the opposite direction (Figure V.2). The spin filtering depends on the chirality/handedness, the number of helical turns, and the length of the molecule.²⁵

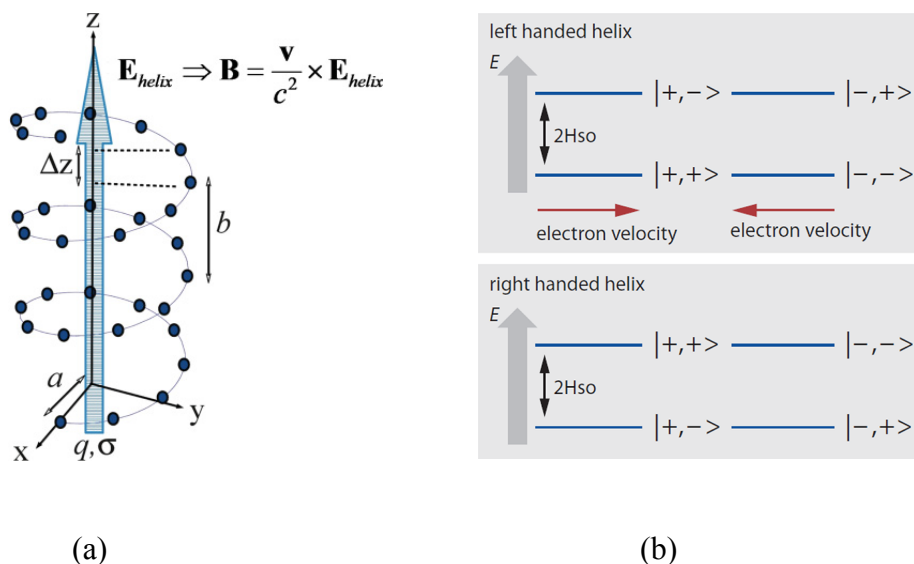


Figure V.2: (a) A schematic representation of the movement of a charge q with spin state σ along a helical electric field (path of the charge is shown by blue circles). “ a ”, “ b ” and “ Δz ” are the radius of the helix, the pitch of the helix and the position vector of the charges distributed along the helix, respectively. The helical electric field, \mathbf{E}_{helix} induces a magnetic field \mathbf{B} in the rest frame of the charge and thus influences its spin state.²⁵ The degenerate magnetic dipole associated with a moving electron (charge q of spin state σ) along the helix becomes split due to the generated magnetic field \mathbf{B} .²⁶ (b) An energy diagram to explain the CISS effect. A freely moving electron has four states associated with its motion. Those states are given by $|+, +\rangle$, $|-, -\rangle$, $|+, -\rangle$ and $|-, +\rangle$. The first and second variables denote the direction of motion and spin, respectively. Spin up (+) is stabilized relative to the spin down (−) state for an electron that moves towards the positive (+) direction along a left-handed helix. Thus, the $|+, +\rangle$ state is stabilized by spin-orbit coupling to the same extent that the $|+, -\rangle$ state is destabilized. $|+, +\rangle$ state is also degenerate with the state $|-, -\rangle$ which is the stabilized state for the electron moving in the opposite direction of the same helix. The $|+, -\rangle$ state has a $|-, +\rangle$ degenerate state. An electron of $|+, +\rangle$ state moving towards positive (+) direction to elastically backscatter within the left-handed helix, has to change to $|-, -\rangle$ state, changing its both spin state and momentum (direction). This flipping requires a high energy, and thus unlikely. For the right-handed helix, $|+, -\rangle$, $|-, +\rangle$ and $|+, +\rangle$, $|-, -\rangle$ are the ground states and high energy states, respectively. “Reprinted (adapted) with permission from the reference²⁶. Copyright (2012) American Chemical Society.”

In the research presented in this chapter, we investigated electrochemically the charge transfer through self-assembled monolayers of opposite handed chiral peptides modified with a terminal Fc group adsorbed on the gold substrate. We observed that the charge transfer through chiral peptides is asymmetric and the asymmetry of charge transfer rate is opposite for the opposite handed L- and D- peptides. Asymmetric charge

transfer refers to the different rate constants observed for charge transfer from the electrode to the redox active group situated at the opposite end of the molecule compared to the rate constant for transfer in the opposite sense (Figure V.3).⁹⁻¹⁰

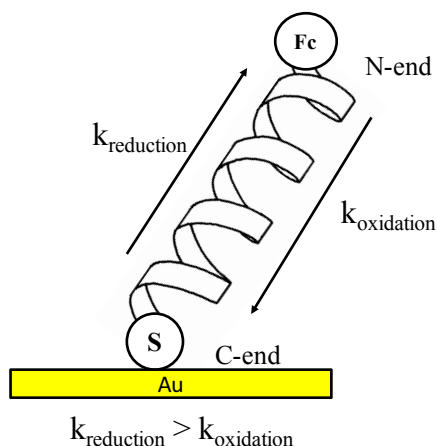


Figure V.3: A cartoon representation to illustrate the asymmetry in charge transfer through Fc-modified peptide attached to a gold substrate. Asymmetric charge transfer means, the rate constant for charge transfer from substrate to Fc group is different than the rate constant for charge transfer from Fc to substrate.

The peptides used for the work presented in this chapter were synthesized by manual solid phase Fmoc-peptide synthesis. The helicity of the peptides was characterized by Circular Dichroism (CD) spectroscopy. Charge transfer through self-assembled monolayers of helical peptides was studied by Cyclic Voltammetry(CV). Dipole moments of the peptides were determined by CPD measurements. The magnetization of the peptide monolayers on gold surface was measured using SQUID.

V.2 Research Design

Naturally-occurring α -helical peptides are right-handed and made up exclusively of L-amino acids. Therefore, one can synthesize opposite handed peptides of same sequence using the L or D enantiomer of the amino acid. A peptide's ability to fold into a helical structure depends mainly on the amino acid sequence and on the peptide length. α -helix formation propensity is high in peptides that are made up of

alanine (Ala/A) residues.²⁷ One disadvantage of polyalanine peptides is that they are extremely hydrophobic, which makes it difficult for one to purify these peptides by reverse phase HPLC to obtain pure batches of single-length polypeptides. The impure nature of the peptide batches influence the quality of the monolayer formation on gold surfaces and makes it hard for one to obtain reproducible results in experiments.²⁸

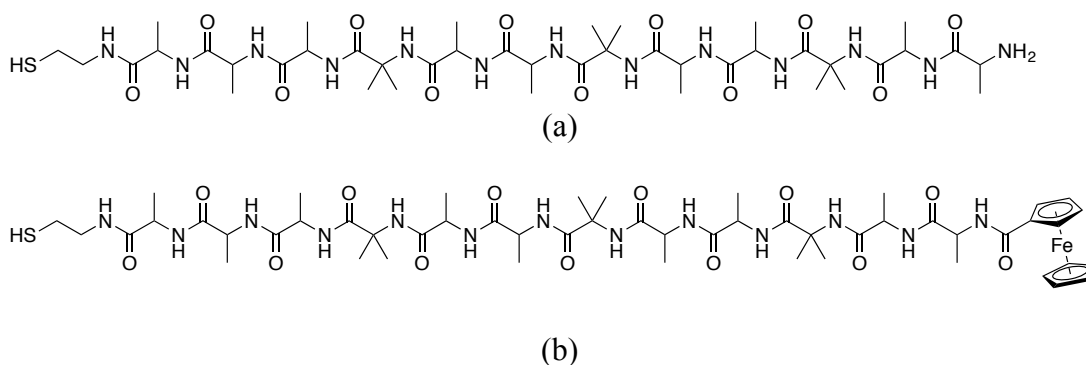
Incorporation of 2-aminoisobutyric acid (Aib/B) residues at intermittent positions along a polyalanine peptide chain improves the solubility of the peptide in aqueous solvents. Aib is also known as a helix promoter in peptide chains.²⁹⁻³¹ Therefore, one can synthesize hydrophilic peptides that fold in to helices by incorporating Aib at intermittent positions in a polyalanine peptide chain. Peptides that fold into helices can adopt either α or 3_{10} helix types. 3_{10} helices have conformational parameters similar to α -helices except, the 3_{10} helix is slightly tighter and more elongated. Several findings have established correlations between helix type and the Aib content or the length of a polypeptide. Peptides which are seven or more amino acids long and consists of 50% Aib residues are likely to adopt a 3_{10} helix whereas peptides of the similar lengths, but contain 30-35% AIB residues favor to adopt an α -helix.³² Bavoso and co-workers stated that Aib rich peptides longer or equal to 8-mer length fold into either a 3_{10} helix or a hybrid 3_{10} - α -helix type.³³ Based on these reported conclusions and the work by Bezer *et.al.*³⁴, I synthesized D/L-9, 12 and 15 mer peptides with cysteamine (Cya) modification at the C-end (Table V.1). Cya is the thiol modification that attaches the peptides onto the gold surface. Peptide chain needed to be modified with a Fc group to do electrochemical studies. The incorporation of the Fc modification to the shortest helical peptide that has a high helix content is both synthetically feasible and cost effective. Therefore, the helicity of the peptides was characterized to determine the shortest peptide that adopt a helical structure.

Table V.1: Peptide sequences and mass spectrometry results

Abbreviation	Sequence from N to C*	MW _{calc}	MW _{exp} D peptide	MW _{exp} L peptide
D/L- 9 mer	H-AABAABAAA-Cya	744.9	745.5	746.1
D/L- 12 mer	H-AABAABAABAAA-Cya	972.2	972.3	972.2
D/L- 12 mer Fc	Fc- AABAABAABAAA-Cya	1184.2	1184.2	1184.2
D/L- 15 mer	H-AABAABAABAABAAA-Cya	1199.42	1220.8	1220.87

*D or L-enantiomer of Ala (A) was used to synthesize D or L peptides.

12 mer peptide was the shortest peptides that adopted a helical structure and it had a similar helix content to the longer 15 mers (Table V.2). Therefore, I chose to synthesize D/L-12 mer peptides with N-terminal Fc modification to study the charge transfer by electrochemistry. The chemical structure of the D/L-12 mers and D/L-12 mers-Fc is shown in Figure V.4.

**Figure V.4:** Chemical structures of (a) D/L-12 mer or (b) D/L-12 mer Fc peptides.

V.3 Results and Discussion

V.3.1 Characterization of the Helicity of the Peptides

CD spectroscopy is usually used to probe peptide or protein secondary structures. The helicity of the peptides was characterized by CD spectroscopy in the same solvent system in which peptide monolayers were formed for electrochemical studies. The CD spectra proved that regardless of the terminal Fc-modification, L and D-peptides adopt right- and left-handed helical structures, respectively (Figure V.5).

Negative peaks at 208 nm and 222 nm and a positive peak at 192 nm are characteristic of right-handed α -helix.³⁵ A mirror image spectrum for a right-handed helix is distinctive for a left-handed helix.³⁶ The negative band at 222 nm arises from $n\text{-}\pi^*$ transitions of the backbone amide chromophore; the negative band at 208 nm and the positive band at 192 nm arise from the $\pi\text{-}\pi^*$ electronic transitions of the same chromophore.³⁷⁻³⁸ The CD spectrum for a right-handed 3_{10} helix is similar to that of an α -helix in their peak positions and signs. However, the peak ~ 190 nm exhibits a much-reduced intensity. 3_{10} helices also show a much weaker peak ~ 222 nm compared to the peak at ~ 208 nm.³⁹

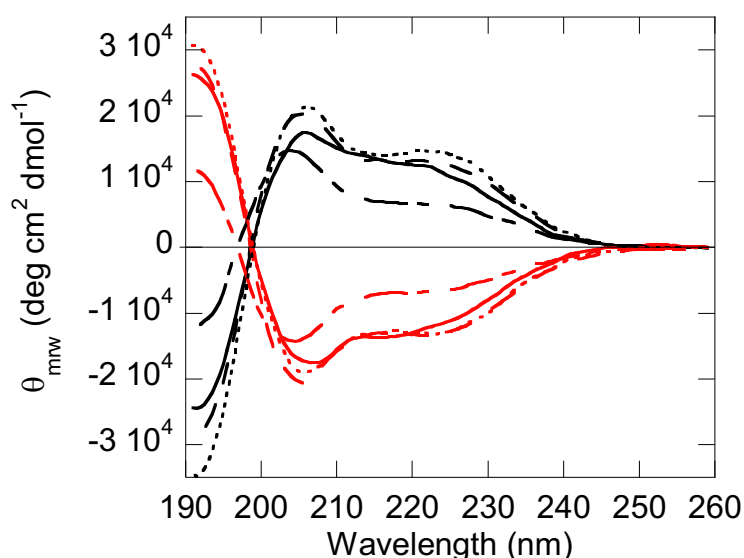


Figure V.5: CD spectra for 0.1 mg/ml solutions of D/L-9 mers (dotted-dashed line), D/L-12 mers (dashed line), D/L-12 mers Fc (solid line) or D/L-15 mers (dotted line) in 1:1(v/v) 10 mM pH 7.00 NaPi:TFE. Black lines are for D-peptides while red lines are for L-peptides.

One can extract additional structural details from a CD spectrum of a helical peptide, i.e. (1) whether the peptide is a 3_{10} helix, mixture of 3_{10} and α helices or an α helix and (2) the percentage helix content (both 3_{10} and α). Specifically, the $\theta_{222\text{ nm}}/\theta_{208\text{ nm}}$ ratio, where $\theta_{222\text{ nm}}$ and $\theta_{208\text{ nm}}$ are ellipticities at 222 and 208 nm, is 0.4 for an

ideal 3_{10} helix and 1.0 for an ideal α helix.³⁹ Ratios between 0.4-1.0 denote that the peptide exists as a mixture of 3_{10} and α helices. The calculated ratios were 0.6 - 0.8 for all the peptides, which indicate that they exist as a mixture of 3_{10} and α helices (Table V.2). This observation is consistent with literature reports, which indicated that Aib-rich peptides longer than eight residues may adopt either a 3_{10} or a mixed $3_{10}/\alpha$ helical structures.³³ The helix content of D/L-9 mers was lower than those for D/L-12 or 15 mers. D/L- 12 and 15 mers have with similar helix contents. (Table V.2). Minor differences in the helix content are observed between the unmodified and Fc-modified peptides.

Table V.2: θ_{222} nm/ θ_{208} nm and percentage helix content of the peptides

Peptide	θ_{222} nm/ θ_{208} nm	Percentage helix content (f_H)
D-9 mer	0.54 \pm 0.02	14 \pm 1
L-9 mer	0.59 \pm 0.02	15 \pm 1
D-12 mer	0.71 \pm 0.02	35 \pm 1
L-12 mer	0.72 \pm 0.03	36 \pm 1
D-12 mer Fc	0.75 \pm 0.02	32 \pm 1
L-12 mer Fc	0.71 \pm 0.02	33 \pm 1
D-15 mer	0.73 \pm 0.01	41 \pm 2
L-15 mer	0.76 \pm 0.04	35 \pm 1

V.3.2 Characterization of Peptide Monolayers formed on Gold Surface

Polarization Modulation Infrared Reflection Absorption Spectroscopy (PM-IRRAS) was used to confirm that the helicity of the peptides is preserved in the monolayers and to assess the packing of the peptide monolayers on the gold electrode surface. Structural data can be derived from the position and intensity of the amide I and amide II absorption bands. Amide I band arises mainly due to stretching vibrations of the C=O group of the peptide backbone of a protein arranged in a helix. This band appears between 1600-1700 cm^{-1} and the exact position depends on the backbone

conformation and the hydrogen bonding pattern. Amide II peak appears between 1510-1580 cm^{-1} and derives mainly from in plane N-H bending vibrations.⁴⁰ Amide I and amide II bands for both D/L-12mer Fc peptide monolayers appear at 1670 cm^{-1} and at 1544 cm^{-1} , respectively (Figure V.6). Exactly same values for amide I and amide II vibrations have been observed for monolayers formed on gold surfaces by α -helical L-(Ala-Aib)_n-Fc peptides.¹⁷ Moreover, the intensities of the amide I and amide II bands for two peptides are identical as well. The extracted tilt angle, γ , of the helix with respect to the surface normal is 48°, which is in good agreement to the reported value for similar systems.¹⁰ Hence, the properties determined using PM-IRRAS indicate that the two peptide enantiomers form similar, densely packed monolayers and adopt the same structure within these monolayers.

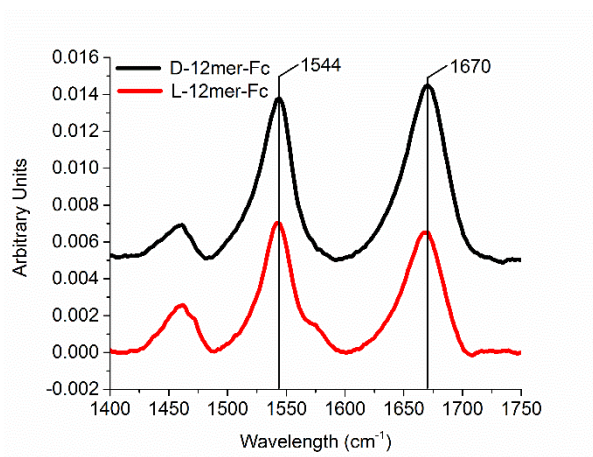


Figure V.6: The amide region of PMIRRAS spectra recorded for the self-assembled monolayers of L-12 mer-Fc and D-12 mer-Fc. The D-12 mer-Fc spectrum is shifted up for clarity.

V.3.3 Charge Transfer Rates Through Opposite-Handed Helical Peptides

The analysis of the electrochemistry data proves that the self-assembled monolayers of D/L-12 mer-Fc peptides, formed on gold, have similar surface coverages (Table V.3). This observation further proves that the two peptide enantiomers form similar monolayers on gold surface. The calculated electron transfer rate constants for

the D and L peptides (Table V.3) are close to what was previously reported for a polyalanine 14-mer.¹⁰ Figure V.7 presents the experimental data compared to the theoretical curve for a k_0 of 0.48 s^{-1} . For the D-peptide, the rate constant, as determined by the analysis of the anodic process, is larger than that determined by the analysis of the cathodic process. In contrast, for the L-peptide, the situation is reversed and the rate constant determined from the cathodic process is larger than that determined from the anodic process.

Table V.3: The electron transfer rate constants and surface coverage for the self-assembled monolayers of L/D-12 mer-Fc.

Peptide	Surface coverage (mol/cm ²)	Rate constant for oxidation (s ⁻¹)	Rate constant for reduction (s ⁻¹)
L-12 mer-Fc	$3.6 \cdot 10^{-11}$	0.30 ± 0.02	0.47 ± 0.03
D-12 mer-Fc	$3.7 \cdot 10^{-11}$	0.48 ± 0.03	0.28 ± 0.03

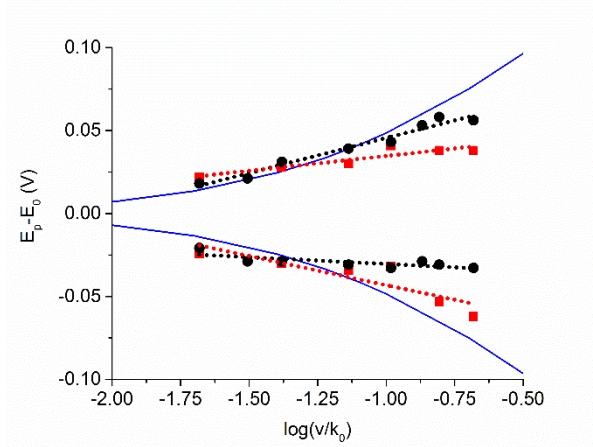


Figure V.7: Plot of peak position relative to the formal potential ($E_p - E_0$) as a function of the normalized scan rate (v/k_0) for either L-12mer-Fc (red squares) or D-12mer-Fc (black dots). The blue solid lines are calculated using the Marcus theory applying a standard electrochemical rate constant (k_0) of 0.48 s^{-1} and assuming the reorganization energy for the ferrocene to be 0.8 eV . The dotted lines are a guide for the eye.

Several groups have reported an asymmetry in the charge transfer through peptides, which contain L-amino acids and adopt a right-handed helical structure.⁹⁻¹⁰

Several reasons have been suggested for the asymmetry (Figure V.3) in the rate constant for electron transfer through peptide monolayers, measured from the anodic and cathodic process: 1) The dipole moment of the helix was suggested to play a role, as it may favor electron-transfer in the direction towards the positive end of the dipole;¹⁰ 2) The amide-ferrocene strong electronic coupling promotes fast electron transfer⁸ that would promote electron transfer between the C-terminal amide group and the sulphur, which was considered the rate-determining step; 3) the polarity of the Au-S junction defines a favorite direction for electron transfer.⁹ These explanations cannot be used to rationalize the asymmetry observed for the two enantiomers because the orientation and strength of the dipole moment, the amide-ferrocene electronic coupling, and the polarity of the Au-S junction do not depend on the chirality of the two peptides. The CPD measurements reported in Table V.4, show that the two enantiomers of the peptides have similar dipole moments. The change of the work function of the Au surfaces, after the monolayer formation, is similar for the two enantiomers.

Table V.4: CPD of gold substrate coated with self-assembled monolayers of peptides.

	CPD (V)
Gold (blank)	0.0±0.004
L-12 mer-Fc monolayer	-0.539±0.017
D-12 mer-Fc monolayer	-0.486±0.006

V.3.4 The Proposed Model

It has been shown that the properties of the gold surface, bridge organic molecule, and redox group are not independent from each other and new properties may emerge when these three components are linked. For example, several groups reported that gold may show magnetic properties when molecules are self-assembled on its surface.^{28, 41-45} The magnetic properties were explained as resulting from both Pauli

principle and orbital paramagnetism in the gold.⁴⁶ Pauli paramagnetism comes from the electrons in the conduction band. When an external magnetic field is applied, the electrons with spin aligned with the field are stabilized. This leads to a different density between the two populations, which yields a positive paramagnetic susceptibility. Orbital paramagnetism arises from the orbital motion of the electrons around the nucleus.

Furthermore, spin-dependent electron transfer was found when a monolayer of organic molecules containing paramagnetic atoms was adsorbed on gold, which indicated that the gold was magnetized.⁴⁷ The magnetic properties of gold may influence electron transfer through self-assembled monolayer of chiral molecules. In recent years it was established that electron transfer through chiral systems is spin dependent.⁴⁸ If the gold is indeed magnetic, its direction of magnetization may affect the spin of the electrons or holes injected from the substrate into the chiral molecule and thereby affect the charge transfer rate through the chiral molecule.

The model we propose to explain the observed asymmetry in the rate constant for the two peptides is based on two components, the magnetization of the system and the spin selective electron transfer through the chiral molecules. It was reported before that linking chromophores to a substrate via organic monolayer may cause a large magnetic anisotropy in the sample.⁴⁹ Several groups already observed that binding paramagnetic molecules to gold, through an organic linker, causes spin selective conduction through the molecules.^{41, 50-52} Hence we propose, that as a result of the induced anisotropy, both the surface magnetization of the gold and the spin on the ferrocene are magnetized parallel to each other, along the axis of the molecule.

To verify this assumption, we measured the magnetization of the peptide monolayer on gold surface at room temperature, using SQUID. Figure V.8 shows the magnetic

moment as a function of the magnetic field applied either perpendicular or parallel to the surface. The results are presented after the subtraction of the contribution of the substrate without the monolayer. A ferromagnetic response with a significant hysteresis is observed for both magnetic field directions. However, the response is non-isotropic. For the field applied perpendicular to the surface, the magnetic susceptibility is large and the hysteresis is about 40 Oe. For the magnetic field applied parallel to the surface, the magnetic susceptibility is somewhat smaller however the hysteresis is much larger, namely 120 Oe. Assuming that the measured magnetic moment at $H=0$ is proportional to the density of the monolayer, we calculated that per molecule the magnetic field corresponds to a $0.86 \mu_B$ for the parallel field and $0.64 \mu_B$ for the perpendicular one. These two values are consistent with a SAM in which the molecules are at a tilt angle with respect to the surface normal of $\sim 50^\circ$, which is similar to the tilt angle inferred from the PM-IRRAS (48°). Based on these results, we conclude that the easy axis of the ferromagnet is along the molecular axis.

In attempting to rationalize the enantio-dependant asymmetry in the electron transfer rate, we propose a model that invokes spin-dependent electron transfer through the chiral molecules, based on CISS and the magnetization of the gold substrate. (Figure V.9).

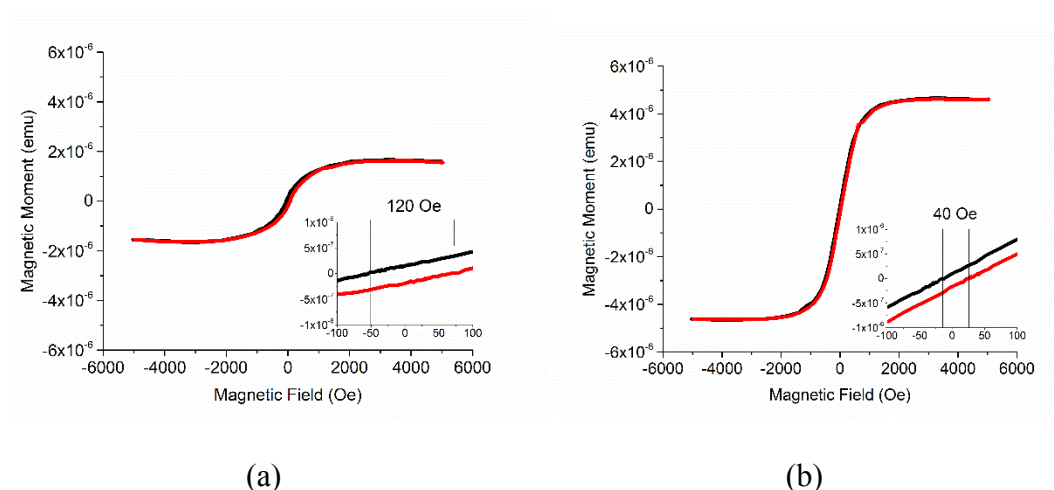


Figure V.8: Magnetic moment versus magnetic field measured by SQUID at 300K for the L-12mer-Fc monolayer adsorbed on gold film. The substrate contribution to the signal has been subtracted from the data. The magnetic field was applied either (a) parallel or (b) perpendicular to the sample surface. The inset is a zoom of the low field region where the hysteresis is largest.

The CISS has an inherent asymmetry, for a given enantiomer, the preferred spin of electrons conducted in one direction is the opposite to that of electrons conducted in the opposite direction. In our system, we assume that both the gold substrate and the ferrocene have a magnetic moment parallel to each other and to the molecular axis. The electrons injected into the oligopeptide have therefore their spin oriented in the same direction, independent if they are transferred from the gold or from the ferrocene and independent on the specific enantiomer. Because of the CISS effect, in the case of the L-peptide the spin is oriented so that its transport is favored for the reduction direction, while for the D-peptide it is favored for the oxidation direction. Since we know from former studies that for the right-handed L peptide the preferred spin orientation is the spin that is aligned parallel to its velocity,²² we conclude that the magnetization of the gold and the ferrocene is pointing away from the surface, parallel to the molecular axis.

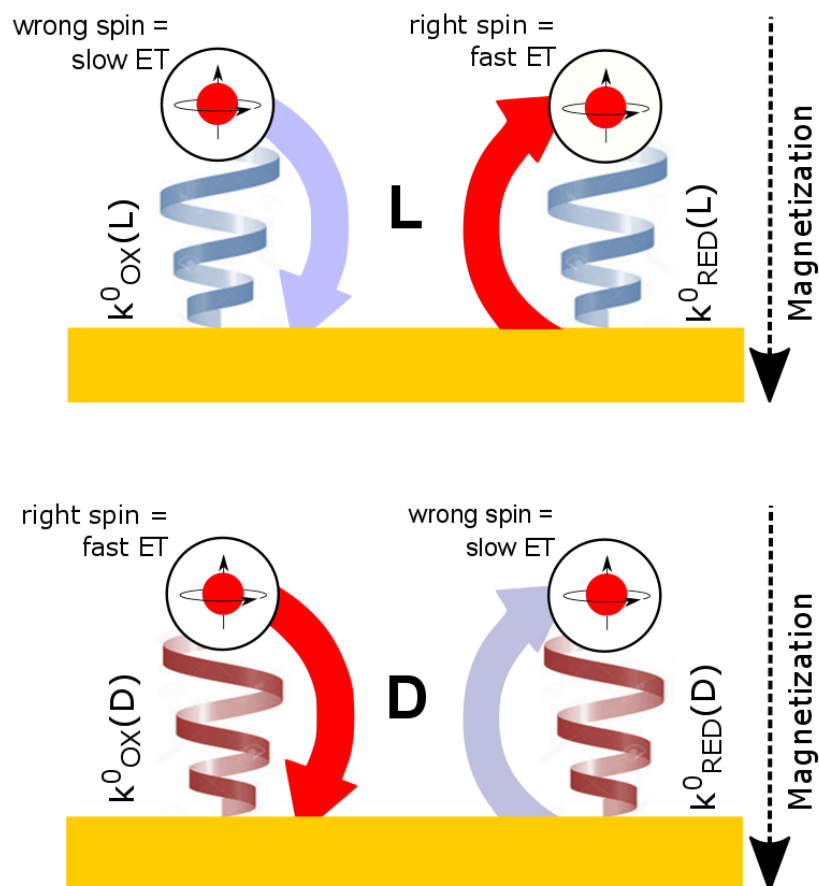


Figure V.9: A scheme of the proposed mechanism for the asymmetric electron transfer. The gold surface is magnetized and as a result, one spin is injected preferentially from it to the molecule or vice versa. In the case of L-12 mer-Fc peptide (right handed helix) the electron injected from the gold has a spin aligned parallel to the electron's velocity, which is the preferred spin for the electron transfer. As a result, the electron transfer in this direction (reduction process) is faster than backwards. In the case of D-12 mer-Fc peptide (left handed helix), the preferred spin orientation is when the spin is aligned antiparallel to the electron's velocity and therefore the preferred rate is for the oxidation process.

V.4 Conclusions

We show that “spontaneous magnetization” occurs when chiral oligopeptides are attached to ferrocene and self-assembled on a gold substrate. The magnetization measured shows high anisotropy and the “easy axis” is along the molecular axis. As a result, the electron transfer, measured by electrochemistry, shows asymmetry in the redox and oxidation rate constants and this asymmetry is reversed between the two

enantiomers. The results are explained by the chiral induced spin selectivity of the electron transfer.

V.5 Material and Methods

V.5.1 Peptide Synthesis

In addition to the peptide sequences given in Table V.1, we also synthesized Cya-D/L-(Ala-Leu)₇-H, Cya-D/L-(Leu-Ala-Ser)₃-H, Cya-D/L-(Aib-Ala-Leu)₄-H and Cya-D/L-(Aib-Ala-Leu)₅-Aib-H. The extreme hydrophobicity of the Cya-D/L-(Ala-Leu)₇-H peptides made it impossible for us to purify them by reverse phase HPLC on a C18-column. We anticipated that the incorporation of the hydrophilic amino acid, D/L-Serine into the sequence would increase the hydrophilicity of the peptides. Indeed Cya-D/L-(Leu-Ala-Ser)₃-H peptide was soluble enough to make possible the purification by reverse phase HPLC on a C18 column. However, the helicity analysis by CD spectroscopy revealed that the peptides adopt a random coil structure (Figure V.10). The incorporation of Aib residues at intermittent positions to Ala-Leu sequence to synthesize Cya-D/L-(Aib-Ala-Leu)₄-H or Cya-D/L-(Aib-Ala-Leu)₅-Aib-H did not make the peptides hydrophilic enough to purify them by reverse phase HPLC.

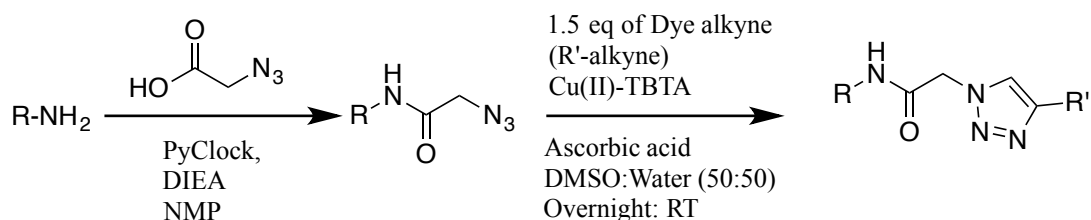
Cysteamine modified D/L- peptides were synthesized manually using the Fmoc-solid phase peptide synthesis strategy, starting from commercially available Cysteamine-4-methoxytrityl resin with a loading of ~0.83 meq/g (Anaspec). Fmoc-D/L-Ala/Leu-OH or Fmoc-D/L-Ser(tBu)-OH amino acids (Anaspec) were coupled using HATU (Chem-Impex) as the coupling reagent while PyClock (Peptides International) was used for the coupling of Fmoc-Aib-OH (Anaspec) and 2-Azidoacetic acid (Sigma Aldrich). HBTU (Chem-Impex) was used as the coupling reagent for Ferrocene Carboxylic acid (Sigma Aldrich). Anhydrous DIEA and anhydrous NMP (Sigma Aldrich) were used as the base and the solvent, respectively. The molar ratios

among growing peptide chain: amino acid: coupling reagent: base were 1:4:3.9:8. The respective molar ratios for 2-Azido acetic acid coupling was 1:4:3.9:12. First amino acid was coupled overnight while the others were coupled for one hour. 2-Azido acetic acid was coupled overnight. The coupling of the amino acids were repeated and the success of coupling was monitored by qualitative Kaiser test. The peptides were cleaved from the resin for 3 hours with a cleavage cocktail of 95% TFA (EMD): 2.5% TIS (Sigma Aldrich): 2.5% water and two drops of Immobilized TCEP disulfide reducing gel (Thermo Scientific). Azide modified peptide were cleaved from the resin using 92.5% TFA (EMD): 2.5% TIS (Sigma Aldrich): 2.5% water: 2.5% Dithiothreitol. Crude peptides were precipitated with cold diethyl ether (EMD) and dried under nitrogen. Peptides were purified by reversed-phase HPLC equipped with a C18 silica column on a Waters 600 controller and pump. Absorbance was monitored at 210 nm with a Waters 2996 photodiode array detector. Peptide masses were determined by ESI-MS or MALDI-ToF-MS on an Applied Biosystems Voyager biospectrometry workstation using α -cyano-4-hydroxycinnamic acid as the matrix (10 mg/ml in water/acetonitrile, 0.1% TFA). Samples of the lyophilized D/L-9,12 or 15 mer peptides were dissolved in nano pure water and those of D/L-12-mer-Fc were dissolved a 1:1 (v/v) mixtue of 2,2,2-trifluoroethanol (TFE) and nano pure water.

Table V.5: Peptide sequences and mass spectrometry results

Peptide (C to N)	MWcalc	MWexp D peptide	MWexp L peptide
Cya-D/L-(Ala-Leu) ₇ -H	1366.8	1366.5	1366.4
Cya-D/L-(Lue-Ala-Ser) ₃ -H	1162.41	1184.33	1184.76
Cya-D/L-(Aib-Ala-Leu) ₄ -H	1239.63	1263.00	1263.00
Cya-D/L-(Aib-Ala-Leu) ₅ -Aib-H	1508.98	1532.27	1532.17
D/L-9 mer-azide	827.95	850.2	850.4
D/L-9 mer-Cy3	1324.66	1320.63	1320.65
D-9mer-Mega stoke 673	1294.50	1315.32	-
D/L-12 mer-azide	1055.22	1077.5	1077.5
D/L-15 mer-azide	1282.477	1304.7	1304.7

We also synthesized dye-modified peptides by “click chemistry”. The azide modification to peptides was introduced on the solid phase. Then, the azide-modified peptides were cleaved from the resin and coupled to the dyes in solution. The general reaction is shown in Scheme V.1



Scheme V.1: Reaction for coupling of dye on to peptide

0.2-2 mM solutions of azide-modified peptide were prepared in water. 10 mM stock solutions of Cyanine3 alkyne (Lumiprobe) or Alkyne MegaStokes dye 673 (Sigma Aldrich) were prepared in DMSO. A 5 mM ascorbic acid solution was freshly prepared in water. 10 mM Cu(II)-TBTA complex in 55 vol.% in DMSO and water was obtained from Kerafast. Each reagent and solvent was degassed with Ar for a few minutes. Azide-modified peptide dissolved in water was mixed with 2 M pH 7.00 triethylammonium acetate buffer to final buffer concentration of 0.2 M. DMSO was added to this solution, so that the final composition of DMSO in the reaction mixture is 50% (v/v). To this solution, 1.5 molar excess of the dye alkyne of stock concentration 10 mM was added. Then, 5 mM Ascorbic acid, followed by 10 mM Cu(II)-TBTA complex were added to the reaction mixture, to 0.5 mM final concentration of each. Reaction mixture was vortexed and degassed with Ar for a few minutes after addition of each reagent. Reaction was left on a shaker at room temperature overnight. The product was precipitated with acetone and incubated at -20 °C for 20 minutes. Then, the reaction mixture was centrifuged at 10,000 rpm for 10 minutes and the pellet was washed with acetone. Solid was dried under nitrogen. Product mass was determined by

MALDI-ToF-MS on an Applied Biosystems Voyager biospectrometry workstation using α -cyano-4-hydroxycinnamic acid as the matrix (10 mg/ml in water/acetonitrile, 0.1% TFA).

V.5.2 CD Spectroscopy

The CD spectra for the peptides were measured in 1:1 (v/v) mixture of 10 mM, pH 7.00 sodium phosphate (NaPi) buffer and TFE, in 0.1 cm path length cuvettes, at 20 °C on a JASCO J-715 spectrometer equipped with a thermoelectrically controlled single-cell holder. The scan rate was 100 nm/min and 10 scans were accumulated for each spectrum. The concentration of the peptides was 0.1 mg/ml. The helix content of the peptides was determined from the CD data using the equations:⁵³

$$f_H = -([\theta]_{222} + 2340)/30300$$

where $[\theta]_{222}$ is the mean residue ellipticity at 222 nm, and f_H is the fraction of helix (both α and 3_{10}).

$$[\theta]_{222}(\text{deg cm}^2 \text{ dmol}^{-1}) = \theta_{222} * M/[10 * d * C * (N - 1)]$$

where θ_{222} is the observed ellipticity at 222 nm in degrees, M is the molecular weight of the peptide, d is the path length in cm, C is the concentration in g/ml and N is the number of peptide bonds in the peptide.⁵⁴

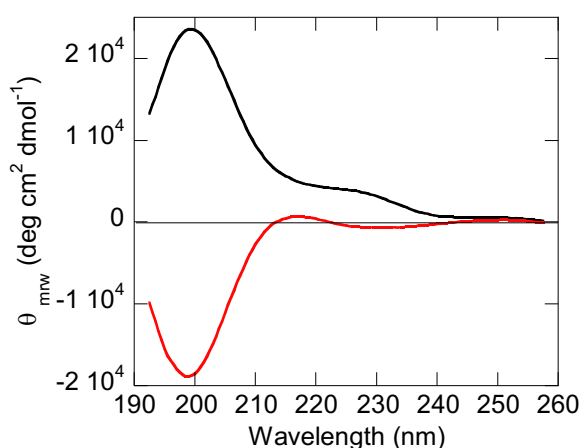


Figure V.10: CD spectra for 12 µg/ml solutions of Cya-D/L-(Leu-Ser-Ala)₃-H in 10 mM pH 7.00 NaPi buffer. Black line: D-peptide, Red line: L-peptide. The CD spectra were measured in a 1 cm path length cuvette.

V.5.3 Monolayer Formation

The 120 nm thick gold surfaces were prepared by electron beam evaporation on a p-doped silicon wafer, using 3 nm of chromium as the adhesion layer. The gold surfaces were cleaned by boiling them first in acetone and then in ethanol for 10 minutes, followed by a UV-ozone cleaning for 15 minutes and a final incubation in warm ethanol for 40 minutes. The surface, dried with a nitrogen gun, where immediately immersed into the peptide solution (0.625 mg/ml, using a 1:1(v/v) mixture of pH 7.00 10 mM NaPi and TFE as solvent) and incubated for 36 h. After the incubation, the surfaces were rinsed 3 times with deionized water, dried with a nitrogen gun and immediately used for the experiments.

V.5.4 Polarization Modulation Infrared Reflection Absorption Spectroscopy (PMIRRAS)

Infrared spectra were recorded in polarization modulation–infrared reflection–absorption mode, using a Nicolet 6700 FTIR instrument, equipped with a PEM-90 photoelastic modulator (Hinds Instruments, Hillsboro, OR), at an 80° angle of incidence. The orientation of the peptides on the gold surface was determined using the following equation:

$$\frac{I_1}{I_2} = 1.5 \times \left[\frac{(3\cos^2 \gamma - 1)(3\cos^2 \theta_1 - 1) + 2}{(3\cos^2 \gamma - 1)(3\cos^2 \theta_2 - 1) + 2} \right]$$

where I_1 and I_2 are the intensity of the amide I and amide II bands, θ_1 and θ_2 are the angles between the transition moment of the two bonds and the helical axis (which are found in the literature to be 39° and 75° respectively) and γ is the tilt angle of the helix in respect to the surface normal.⁵⁵⁻⁵⁶

V.5.5 Electrochemistry

The electrochemical experiments consisted in cyclic voltammetry experiments carried out at different scan rates (ν) ranging from 10 mV/s to 100 mV/s in a potential window from 0.0 to 0.7 V, using the oligopeptide modified gold surface as working electrode. The measurements were done using a standard three-electrode setup, in a supporting electrolyte solution of 0.1 M NaClO₄, using a Pt wire as the counter electrode and an Ag/AgCl (sat. KCl) electrode as reference. Following the same approach used by Waldeck and collaborators,⁵⁷ the charge transfer rate constant k^0 was obtained from the experimental data by plotting the anodic and cathodic peak separation ($E_p - E_0$) versus the normalized scan rate (ν/k^0) and fitting the data by a curve obtained by Marcus theory, using a recombination energy (λ) of 0.8 eV for the ferrocene. The surface coverage Γ is calculated integrating the charge under the faradaic current peaks at a scan rate of 50 mV/s.

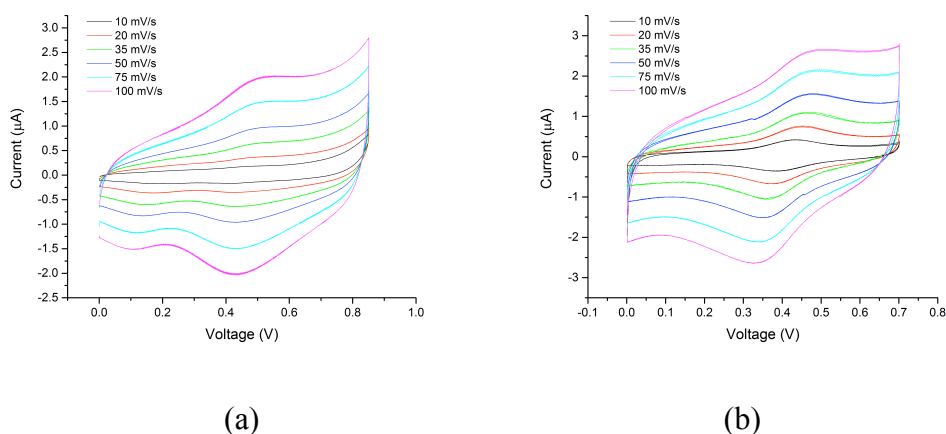


Figure V.11: Cyclic voltammograms for (a) D-12 mer Fc and (b) L-12 mer Fc

V.5.6 Contact Potential Difference (CPD)

The CPD of the surfaces was determined using a commercial Kelvin probe instrument (Delta Phi Besocke, Jülich, Germany) within a Faraday cage. The reference probe consisted of a gold grid. The measurements were held in the dark and in ambient atmosphere. The CPD signal of a blank gold substrate was taken as the zero value. The CPD of the monolayers is reported as the difference between the gold reference and the value recorded for the monolayers after letting the signal to stabilize.

V.5.7 Superconducting Quantum Interference Device (SQUID) Measurements

A SQUID magnetometer MPMS2 (magnetic property measurement system 2) with an absolute sensitivity of 10^{-7} emu was used to measure the magnetic properties of peptide monolayers, with the magnetic field applied either parallel or perpendicular to the sample plane. The measurements were conducted at 300 K, and consisted in a magnetizing run from 0 Oe to 6000 Oe, a first measurement going from 6000 Oe to -6000 Oe, a second going from -6000 Oe to 6000 Oe, and a demagnetizing run from 6000 Oe to 0 Oe. The diamagnetic contribution of the gold-silicon substrate was measured prior to the monolayer formation and subtracted from the final data. Figure V.12 and Figure V.13 report the measurements done on the bare gold surface and the unprocessed data for the monolayers.

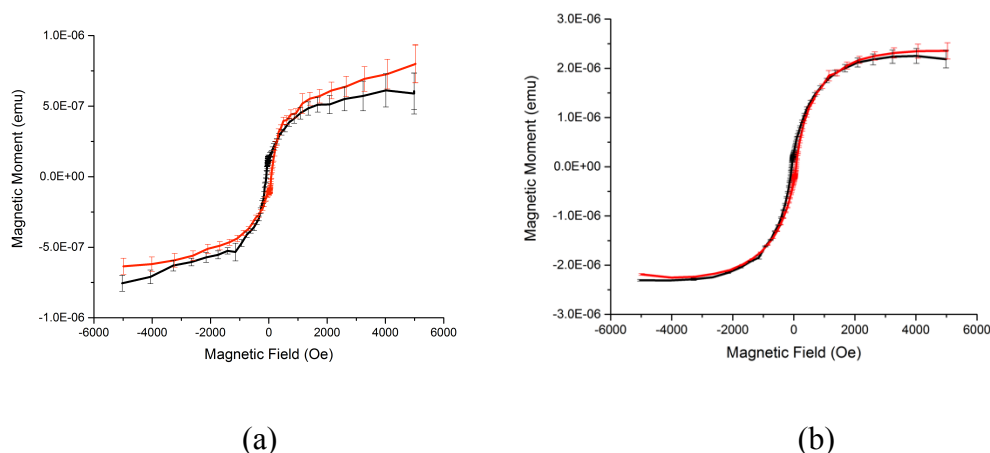


Figure V.12: SQUID measurements for the bare gold surface that has been used as a substrate for the L-12mer-Fc monolayer formation. Applied magnetic field (a) parallel to the field and (b) perpendicular to the field.

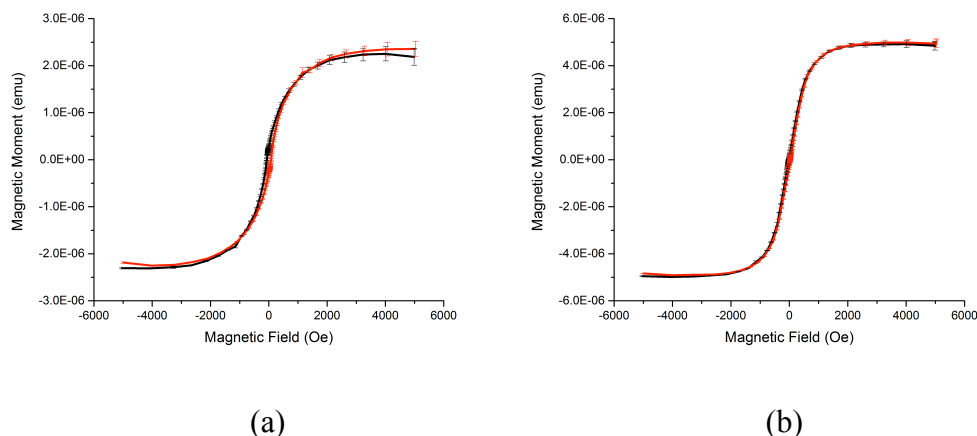


Figure V.13: SQUID measurements for the L-12mer-Fc monolayer prior to subtraction of the magnetic moment due to the bare gold substrate. Applied magnetic field (a) parallel to the field and (b) perpendicular to the field.

V.6 References

1. Bashir, Q.; Scanu, S.; Ubbink, M., Dynamics in electron transfer protein complexes. *FEBS J.*, **2011**, 278 (9), 1391-1400.
2. Horsley, J.; Yu, J.; Yeoh, Y. Q.; Abell, A., Peptides as Bio-inspired Molecular Electronic Materials. In *Peptides and Peptide-based Biomaterials and their Biomedical Applications*, Springer: 2017; pp 131-153.
3. Shah, A.; Adhikari, B.; Martic, S.; Munir, A.; Shahzad, S.; Ahmad, K.; Kraatz, H.-B., Electron transfer in peptides. *Chem. Soc. Rev.*, **2015**, 44 (4), 1015-1027.
4. Arikuma, Y.; Nakayama, H.; Morita, T.; Kimura, S., Ultra-Long-Range Electron Transfer through a Self-Assembled Monolayer on Gold Composed of 120-Å-Long α -Helices. *Langmuir*, **2010**, 27 (4), 1530-1535.

5. Kai, M.; Takeda, K.; Morita, T.; Kimura, S., Distance dependence of long-range electron transfer through helical peptides. *J. Pept. Sci.*, **2008**, *14* (2), 192-202.
6. Arikuma, Y.; Nakayama, H.; Morita, T.; Kimura, S., Electron Hopping over 100 Å along an α Helix. *Angew. Chem. Int. Ed.*, **2010**, *49* (10), 1800-1804.
7. Morita, T.; Kimura, S., Long-range electron transfer over 4 nm governed by an inelastic hopping mechanism in self-assembled monolayers of helical peptides. *J. Am. Chem. Soc.*, **2003**, *125* (29), 8732-8733.
8. Watanabe, J.; Morita, T.; Kimura, S., Effects of dipole moment, linkers, and chromophores at side chains on long-range electron transfer through helical peptides. *J. Phys. Chem. B*, **2005**, *109* (30), 14416-14425.
9. Venanzi, M.; Gatto, E.; Caruso, M.; Porchetta, A.; Formaggio, F.; Toniolo, C., Photoinduced Electron Transfer through Peptide-Based Self-Assembled Monolayers Chemisorbed on Gold Electrodes: Directing the Flow-in and Flow-out of Electrons through Peptide Helices. *J. Phys. Chem. A*, **2014**, *118* (33), 6674-6684.
10. Sek, S.; Tolak, A.; Misicka, A.; Palys, B.; Bilewicz, R., Asymmetry of electron transmission through monolayers of helical polyalanine adsorbed on gold surfaces. *J. Phys. Chem. B*, **2005**, *109* (39), 18433-18438.
11. Galoppini, E.; Fox, M. A., Effect of the electric field generated by the helix dipole on photoinduced intramolecular electron transfer in dichromophoric α -helical peptides. *J. Am. Chem. Soc.*, **1996**, *118* (9), 2299-2300.
12. Shin, Y.-g. K.; Newton, M. D.; Isied, S. S., Distance dependence of electron transfer across peptides with different secondary structures: the role of peptide energetics and electronic coupling. *J. Am. Chem. Soc.*, **2003**, *125* (13), 3722-3732.
13. Amit, M.; Cheng, G.; Hamley, I. W.; Ashkenasy, N., Conductance of amyloid β based peptide filaments: structure–function relations. *Soft Matter*, **2012**, *8* (33), 8690-8696.
14. Zheng, Y.; Case, M. A.; Wishart, J. F.; McLendon, G. L., Do main chain hydrogen bonds create dominant electron transfer pathways? An investigation in designed proteins. *J. Phys. Chem. B*, **2003**, *107* (30), 7288-7292.
15. Antonello, S.; Formaggio, F.; Moretto, A.; Toniolo, C.; Maran, F., Anomalous distance dependence of electron transfer across peptide bridges. *J. Am. Chem. Soc.*, **2003**, *125* (10), 2874-2875.
16. Polo, F.; Antonello, S.; Formaggio, F.; Toniolo, C.; Maran, F., Evidence against the hopping mechanism as an important electron transfer pathway for conformationally constrained oligopeptides. *J. Am. Chem. Soc.*, **2005**, *127* (2), 492-493.
17. Takeda, K.; Morita, T.; Kimura, S., Effects of monolayer structures on long-range electron transfer in helical peptide monolayer. *J. Phys. Chem. B*, **2008**, *112* (40), 12840-12850.
18. Skourtis, S. S., Probing protein electron transfer mechanisms from the molecular to the cellular length scales. *Peptide Science*, **2013**, *100* (1), 82-92.
19. Xiao, X.; Xu, B.; Tao, N., Conductance titration of single-peptide molecules. *J. Am. Chem. Soc.*, **2004**, *126* (17), 5370-5371.
20. Sisido, M.; Hoshino, S.; Kusano, H.; Kuragaki, M.; Makino, M.; Sasaki, H.; Smith, T. A.; Ghiggino, K. P., Distance dependence of photoinduced electron transfer along α -helical polypeptides. *J. Phys. Chem. B*, **2001**, *105* (42), 10407-10415.
21. Malak, R. A.; Gao, Z.; Wishart, J. F.; Isied, S. S., Long-range electron transfer across peptide bridges: The transition from electron superexchange to hopping. *J. Am. Chem. Soc.*, **2004**, *126* (43), 13888-13889.

22. Kettner, M.; Gohler, B.; Zacharias, H.; Mishra, D.; Kiran, V.; Naaman, R.; Fontanesi, C.; Waldeck, D. H.; S k, S.; Paw owski, J., Spin filtering in electron transport through chiral oligopeptides. *J. Phys. Chem. C*, **2015**, *119* (26), 14542-14547.
23. Kiran, V.; Cohen, S. R.; Naaman, R., Structure dependent spin selectivity in electron transport through oligopeptides. *J. Chem. Phys.*, **2017**, *146* (9), 092302.
24. Michaeli, K.; Kantor-Uriel, N.; Naaman, R.; Waldeck, D. H., The electron's spin and molecular chirality—how are they related and how do they affect life processes?, *Chem. Soc. Rev.*, **2016**, *45* (23), 6478-6487.
25. Gutierrez, R.; D  az, E.; Naaman, R.; Cuniberti, G., Spin-selective transport through helical molecular systems. *Phys. Rev. B*, **2012**, *85* (8), 081404.
26. Naaman, R.; Waldeck, D. H., Chiral-induced spin selectivity effect. *J. Phys. Chem. Lett.*, **2012**, *3* (16), 2178-2187.
27. Marqusee, S.; Robbins, V. H.; Baldwin, R. L., Unusually stable helix formation in short alanine-based peptides. *Proc. Natl. Acad. Sci. U.S.A.*, **1989**, *86* (14), 5286-5290.
28. Carmeli, I.; Skakalova, V.; Naaman, R.; Vager, Z., Magnetization of chiral monolayers of polypeptide: a possible source of magnetism in some biological membranes. *Angew. Chem. Int. Ed.*, **2002**, *41* (5), 761-764.
29. Marshall, G. R.; Hodgkin, E. E.; Langs, D. A.; Smith, G. D.; Zabrocki, J.; Leplawy, M. T., Factors governing helical preference of peptides containing multiple alpha, alpha-dialkyl amino acids. *Proc. Natl. Acad. Sci. U.S.A.*, **1990**, *87* (1), 487-491.
30. Karle, I. L.; Balaram, P., Structural characteristics of alpha-helical peptide molecules containing Aib residues. *Biochemistry*, **1990**, *29* (29), 6747-6756.
31. Tonlolo, C.; Benedetti, E., The polypeptide 310-helix. *Trends Biochem. Sci.*, **1991**, *16*, 350-353.
32. Karle, I. L.; Sukumar, M.; Balaram, P., Parallel packing of alpha-helices in crystals of the zervamicin IIA analog Boc-Trp-Ile-Ala-Aib-Ile-Val-Aib-Leu-Aib-Pro-OMe. 2H₂O. *Proc. Natl. Acad. Sci. U.S.A.*, **1986**, *83* (24), 9284-9288.
33. Bavoso, A.; Benedetti, E.; Di Blasio, B.; Pavone, V.; Pedone, C.; Toniolo, C.; Bonora, G. M.; Formaggio, F.; Crisma, M., Long, chiral polypeptide 310-helices at atomic resolution. *J. Biomol. Struct. Dyn.*, **1988**, *5* (4), 803-817.
34. Bezer, S.; Matsumoto, M.; Lodewyk, M. W.; Lee, S. J.; Tantillo, D. J.; Gagn  , M. R.; Waters, M. L., Identification and optimization of short helical peptides with novel reactive functionality as catalysts for acyl transfer by reactive tagging. *Org. Biomol. Chem.*, **2014**, *12* (9), 1488-1494.
35. Holzwarth, G.; Doty, P., The ultraviolet circular dichroism of polypeptides1. *J. Am. Chem. Soc.*, **1965**, *87* (2), 218-228.
36. Mortishire-Smith, R. J.; Drake, A. F.; Nutkins, J. C.; Williams, D. H., Left handed α -helix formation by a bacterial peptide. *FEBS Lett.*, **1991**, *278* (2), 244-246.
37. Woody, R. W.; Tinoco Jr, I., Optical rotation of oriented helices. III. Calculation of the rotatory dispersion and circular dichroism of the alpha-and 310-helix. *J. Chem. Phys.*, **1967**, *46* (12), 4927-4945.
38. Schellman, J. A.; Oriel, P., Origin of the Cotton effect of helical polypeptides. *J. Chem. Phys.*, **1962**, *37* (9), 2114-2124.
39. Toniolo, C.; Polese, A.; Formaggio, F.; Crisma, M.; Kamphuis, J., Circular dichroism spectrum of a peptide 310-helix. *J. Am. Chem. Soc.*, **1996**, *118* (11), 2744-2745.
40. Krimm, S.; Bandekar, J., Vibrational spectroscopy and conformation of peptides, polypeptides, and proteins. *Adv. Protein Chem.*, **1986**, *38*, 181-364.
41. Crespo, P.; Litr  n, R.; Rojas, T.; Multigner, M.; De la Fuente, J.; S  nchez-L  pez, J.; Garc  a, M.; Hernando, A.; Penad  s, S.; Fern  ndez, A., Permanent magnetism,

- magnetic anisotropy, and hysteresis of thiol-capped gold nanoparticles. *Phys. Rev. Lett.*, **2004**, *93* (8), 087204.
42. Trudel, S., Unexpected magnetism in gold nanostructures: making gold even more attractive. *Gold Bull*, **2011**, *44* (1), 3-13.
43. Singh, R., Unexpected magnetism in nanomaterials. *J. Magn. Magn. Mater.*, **2013**, *346*, 58-73.
44. Nealon, G. L.; Donnio, B.; Greget, R.; Kappler, J.-P.; Terazzi, E.; Gallani, J.-L., Magnetism in gold nanoparticles. *Nanoscale*, **2012**, *4* (17), 5244-5258.
45. Agrachev, M.; Antonello, S.; Dainese, T.; Ruzzi, M.; Zoleo, A.; Aprà, E.; Govind, N.; Fortunelli, A.; Sementa, L.; Maran, F., Magnetic Ordering in Gold Nanoclusters. *ACS Omega*, **2017**, *2* (6), 2607-2617.
46. Suzuki, M.; Kawamura, N.; Miyagawa, H.; Garitaonandia, J. S.; Yamamoto, Y.; Hori, H., Measurement of a Pauli and orbital paramagnetic state in bulk gold using x-ray magnetic circular dichroism spectroscopy. *Phys. Rev. Lett.*, **2012**, *108* (4), 047201.
47. Aragonès, A. C.; Aravena, D.; Cerdá, J. I.; Acís-Castillo, Z.; Li, H.; Real, J. A.; Sanz, F.; Hihath, J.; Ruiz, E.; Díez-Pérez, I., Large conductance switching in a single-molecule device through room temperature spin-dependent transport. *Nano Lett.*, **2015**, *16* (1), 218-226.
48. Naaman, R.; Waldeck, D. H., Spintronics and chirality: spin selectivity in electron transport through chiral molecules. *Annu. Rev. Phys. Chem.*, **2015**, *66*, 263-281.
49. Zakrassov, A.; Bitler, A.; Etgar, L.; Leitun, G.; Lifshitz, E.; Naaman, R., Controlling the anisotropic magnetic dipolar interactions of PbSe self-assembled nanoparticles on GaAs. *Phys. Chem. Chem. Phys.*, **2009**, *11* (35), 7549-7552.
50. Hernando, A.; Crespo, P.; Garcia, M., Origin of orbital ferromagnetism and giant magnetic anisotropy at the nanoscale. *Phys. Rev. Lett.*, **2006**, *96* (5), 057206.
51. Coey, J.; Venkatesan, M.; Fitzgerald, C.; Douvalis, A.; Sanders, I., Ferromagnetism of a graphite nodule from the Canyon Diablo meteorite. *Nature*, **2002**, *420* (6912), 156-159.
52. Makarova, T., Magnetic properties of carbon structures. *Semiconductors*, **2004**, *38* (6), 615-638.
53. Chen, Y.-H.; Yang, J. T., A new approach to the calculation of secondary structures of globular proteins by optical rotatory dispersion and circular dichroism. *Biochem. Biophys. Res. Commun.*, **1971**, *44* (6), 1285-1291.
54. Kelly, S. M.; Jess, T. J.; Price, N. C., How to study proteins by circular dichroism. *Biochim. Biophys. Acta*, **2005**, *1751* (2), 119-139.
55. López-Pérez, D. E.; Revilla-López, G.; Jacquemin, D.; Zanuy, D.; Palys, B.; Sek, S.; Alemán, C., Intermolecular interactions in electron transfer through stretched helical peptides. *Phys. Chem. Chem. Phys.*, **2012**, *14* (29), 10332-10344.
56. Miura, Y.; Kimura, S.; Imanishi, Y.; Umemura, J., Formation of oriented helical peptide layers on a gold surface due to the self-assembling properties of peptides. *Langmuir*, **1998**, *14* (24), 6935-6940.
57. Wierzbinski, E.; de Leon, A.; Davis, K. L.; Bezer, S.; Wolak, M. A.; Kofke, M. J.; Schlaf, R.; Achim, C.; Waldeck, D. H., Charge Transfer through Modified Peptide Nucleic Acids. *Langmuir*, **2012**, *28* (4), 1971-1981.